


REVIEW

[View Article Online](#)
[View Journal](#) | [View Issue](#)Cite this: *J. Mater. Chem. A*, 2024, **12**, 27855

Mechanical behavior of high-entropy intermetallic compounds and high-entropy ceramics

Bin Li,^a Jialin Sun,^b  ^{*,abc} Xiao Li^d and Jun Zhao^e

High-entropy intermetallic compounds (HEICs) and high-entropy ceramics (HECs) are both novel materials obtained by introducing chemical disorder through the mixing of multiple primary components. In comparison to traditional materials, they exhibit superior mechanical properties. However, the widespread application of HEICs and HECs is greatly hindered by their inferior ductility/toughness. In addition, the conventional trial-and-error method for designing HEICs and HECs is time-consuming and labor-intensive, and the mechanical properties of the final samples are highly uncertain. The primary aim of this review is to summarize the latest research progress on HEICs and HECs, with a focus on relevant phase structure prediction criteria and strengthening/toughening strategies, in order to accelerate their engineering applications. In this article, we have compiled the applications of machine learning and descriptor criteria in the prediction of phase structures. Furthermore, various strengthening/toughening strategies applied in HEICs and HECs were discussed, including solid solution strengthening, second-phase strengthening, nano-composite strengthening, etc. Finally, the challenges and future research directions of HEICs and HECs were also addressed.

Received 17th June 2024
Accepted 16th September 2024

DOI: 10.1039/d4ta04183f

rsc.li/materials-a

1. Introduction

Entropy is a thermodynamic parameter that quantifies the degree of disorder in a material. It was not until 2004 when Yeh *et al.*^{1,2} introduced the concept of high-entropy alloys (HEAs) that an increasing number of scholars came to recognize the significant impact of entropy in driving the development of materials. HEAs are characterized as multi-principal element alloys with high configurational entropy, composed of at least four principal metallic elements in approximately equimolar or near-equimolar fractions. HEAs benefit from four major effects: the thermodynamic high-entropy effect, kinetic sluggish diffusion effect, structural lattice distortion effect, and “cocktail” effect on performance.^{3–5} The high entropy effect is the foundation for the other three effects. It has been suggested that the high entropy effect can enhance the compatibility between multiple principal components and improve the mechanical properties of materials through the solid solution strengthening mechanism. High-entropy materials are composed of multiple elements that are randomly distributed at lattice positions in a multi-atomic size, which inevitably leads to

significant lattice distortion. The sluggish diffusion effect is currently facing scrutiny. Relevant studies suggest that hysteresis diffusion may not be applicable to CoCrFeNi and CoCrFeMnNi high-entropy alloys (HEAs).^{6–8} Therefore, more in-depth research on the sluggish diffusion effect is needed in the future. The cocktail effect refers to the ability to achieve unexpected properties in high-entropy materials by carefully selecting key elements. Adding high melting point elements such as tungsten and vanadium can enhance the high-temperature resistance of the alloy, while choosing aluminum and silicon can improve the oxidation resistance of the resulting high-entropy alloy.³

These effects demonstrate outstanding comprehensive mechanical properties, making high-entropy materials a well-deserved research hotspot over the past 20 years. In recent years, the field of high-entropy materials has introduced revolutionary structural materials such as high-entropy intermetallic compounds (HEICs), high-entropy ceramics (HECs), high-entropy cemented carbides (HECCs) (Fig. 1), *etc.*

Similar to HEAs, HECs are defined as the solid solution of corresponding five or more binary ceramic compounds with large configurational entropy. In 2015, the first bulk single-phase (MgCoNiCuZn)O HEC was synthesized by Rost *et al.*⁹ proposing entropy-stabilized ceramics. Since then, HECs have expanded from oxides to carbides, borides, nitrides, and silicides as well as multi-anion HECs such as carbonitrides, oxynitrides, borocarbides, borocarbonitrides and so on. As depicted in Fig. 2(a), the high frequency research objects of HECs mainly include mechanical properties, microstructure evolution, sintering behavior *etc.* Similarly, HECs exhibit

^aSchool of Mechanical, Electrical & Information Engineering, Shandong University, Weihai 264209, PR China. E-mail: sunjialin@sdu.edu.cn^bShenzhen Research Institute of Shandong University, Shenzhen 518057, PR China^cState Key Laboratory of Solid Lubrication, Lanzhou Institute of Chemical Physics, Chinese Academy of Sciences, Lanzhou 730000, PR China^dWeihai Weiyang Tool Co., Ltd, Weihai, 264210, PR China^eKey Laboratory of High Efficiency and Clean Mechanical Manufacture of MOE, School of Mechanical Engineering, Shandong University, Jinan 250061, PR China

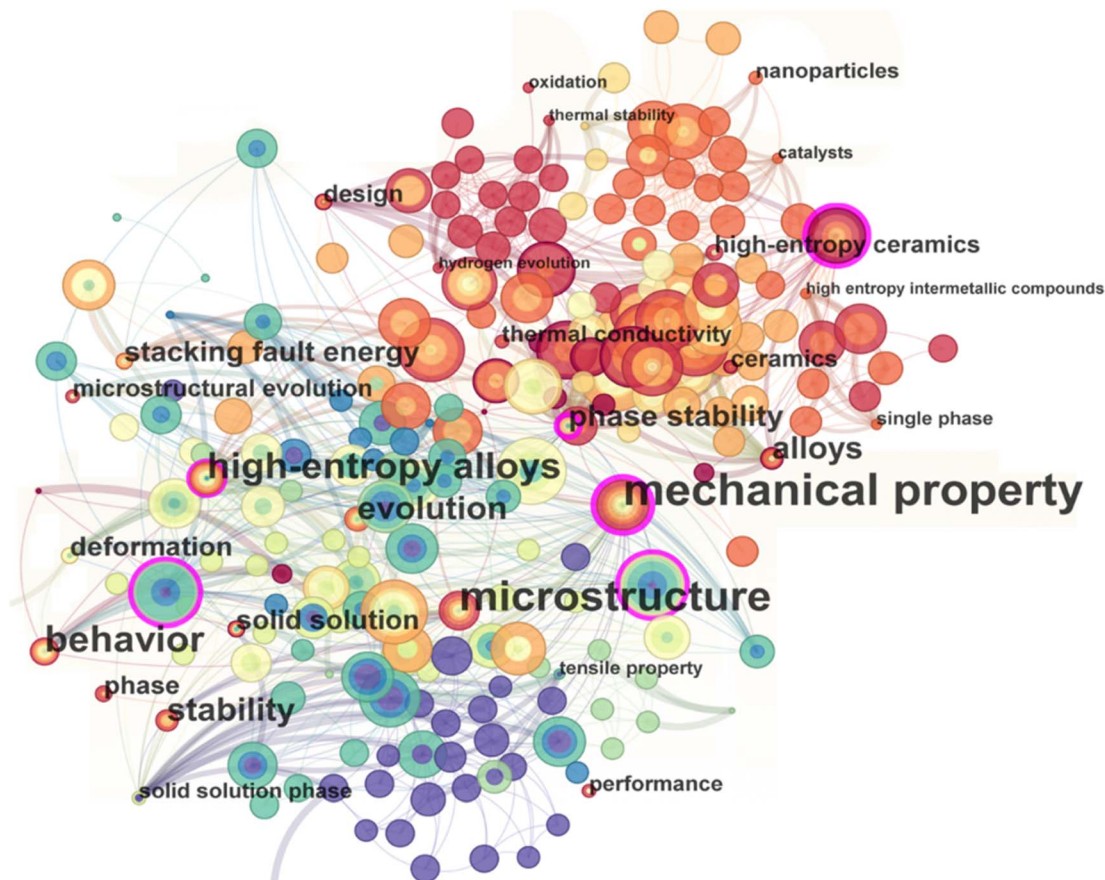


Fig. 1 High-entropy material keyword co-occurrence graph.

superior stability and properties as a function of the combined high-entropy effect, sluggish diffusion effect, lattice distortion effect and cocktail effect. For example, as illustrated in Fig. 2(b), HECs enjoy much higher hardness in comparison with traditional ceramic matrices. Besides, HECs generally have more oxidation/corrosion/creep resistance and augmented thermal stability compared with conventional ceramics.^{19,20} Yet, it is worth mentioning that the toughness of HECs yielded no obvious enhancement compared to traditional ceramics,

dramatically limiting the practical application of HECs. Toughening is also the urgent issue for HEC matrices with advanced applications.

The term HEIC could date back to Tsai describing the multi-principal element intermetallic in 2016.²¹ In the simplest case, the structure of HEICs could be expressed as $(A_1, A_2, \dots, A_m) \times (B_1, B_2, \dots, B_n)y$, in which A or/and B sublattices is/are in the form of high entropy substitution solid solution, significantly influencing the configurational entropy of the system as

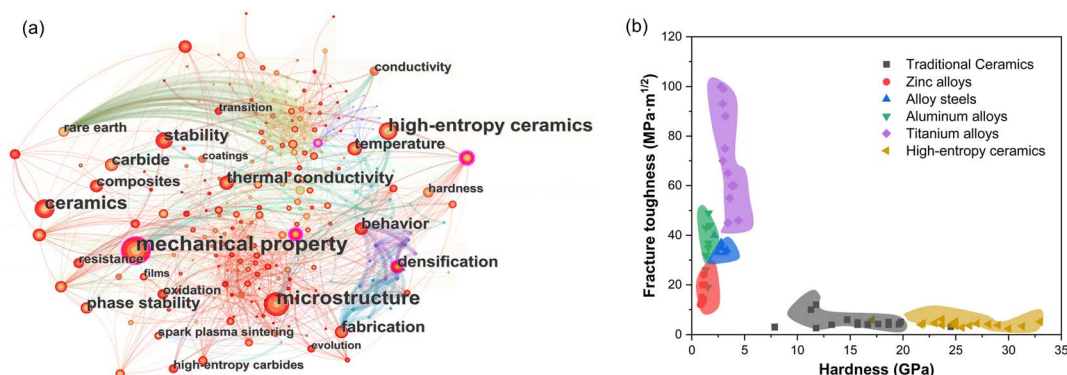


Fig. 2 (a) High-entropy ceramics keyword co-occurrence graph; (b) comparison of hardness–fracture toughness of high-entropy ceramics with other conventional metals (the mechanical properties of traditional ceramics and alloys are derived from <https://www.makeitfrom.com/>).^{10–18}

a whole.²² It is noteworthy as shown in Fig. 3(a) that ductility, toughness, deformation and mechanical properties are the predominant high frequency research objects for HEICs. As shown in Fig. 3(b), HEICs exhibited simultaneously enhanced ductility and fracture toughness in comparison with traditional intermetallic compounds. However, the trade-off relationship is still present between strength and toughness in the HEIC matrix.

Very recently, in 2023, on the 100th anniversary of the invention of cemented carbides, Sun *et al.*³² proposed the concept of HECCs in an authorized patent, which are composed of a high entropy carbide hard phase and high entropy alloy (or/ and high entropy intermetallic compound) binder phase. Currently, very few literature studies are available on HECCs. However, HEA bonded cemented carbides have been investigated by some scholars. It is declared that WC-HEA hardmetals possess enhanced mechanical properties and oxidation/corrosion resistance compared to traditional WC-Co cemented carbides,³³ as a function of the excellent microstructure stability, splendid high-temperature softening resistance and exceptional thermal-mechanical-chemical properties of HEAs. Based on these reports, HECCs are expected to yield further improved structure stability and properties in comparison with HEA bonded WC cemented carbides. For instance, as illustrated in Fig. 4, HECCs demonstrated slightly lower toughness but much higher hardness than HEAs, whereas it exhibited much higher hardness and toughness in comparison with HECs and HEICs. Furthermore, HECCs enjoyed the much-enhanced hardness and fracture toughness relationship compared to traditional cemented carbides. Therefore, HECCs play a broad role in advanced manufacturing industries, which cannot be matched or replaced by any metal, ceramic materials or traditional cemented carbides.

By comparing the mechanical properties of HECs, HEICs, and HECCs with those of conventional materials, it is evident that high-entropy materials indeed demonstrate superior performance. However, HECs and HEICs are also constrained by the trade-off between strength and plasticity. Furthermore, the phase and microstructure have a significant impact on the

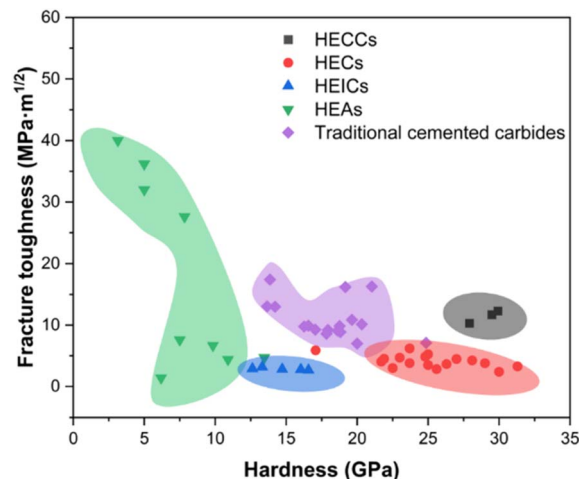


Fig. 4 Comparison chart of hardness and fracture toughness of high-entropy cemented carbide with high-entropy ceramics, high-entropy alloys, high-entropy intermetallic compounds and traditional cemented carbide.^{11–15,17,34–36}

mechanical properties of materials. However, the conventional trial-and-error method for preparing high-entropy materials is not only time-consuming and resource-intensive, but also results in significant uncertainty in the mechanical properties of the final design, thus severely limiting the widespread application of high-entropy materials. Therefore, the purpose of this paper is to summarize the principles of phase structure prediction and strengthening/toughening strategies for HEICs and HECs. Additionally, the study also identified and proposed potential challenges and future research directions for HEICs and HECs.

2. High-entropy intermetallic compounds

2.1 Development history

HEICs are a new class of intermetallic materials. The introduction of the high entropy concept greatly improves the

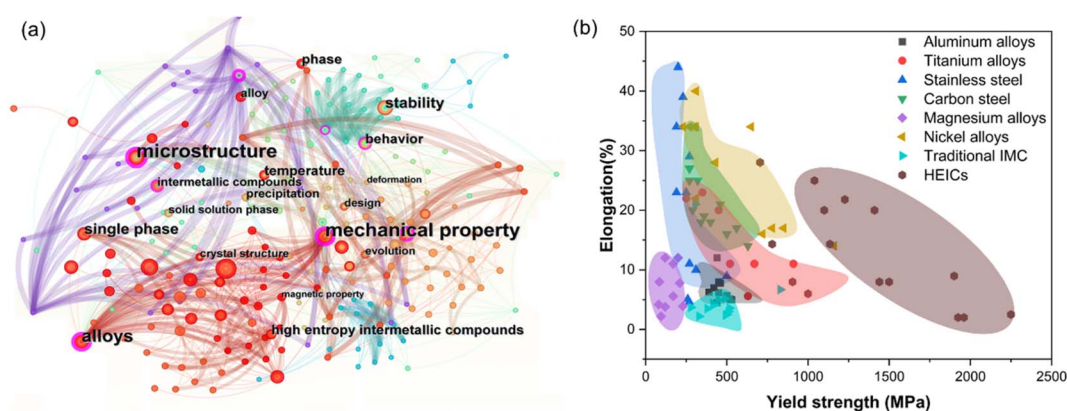


Fig. 3 (a) High-entropy intermetallic compounds keyword co-occurrence graph; (b) comparison of yield strength–elongation of high-entropy intermetallic compounds with that of other conventional metals (the mechanical properties of traditional alloys are derived from <https://www.makeitfrom.com/>).^{23–31}

brittleness of intermetallic compounds in the process of elemental doping. At the same time, HEICs also have four major effects on HEAs, which can be randomly arranged while ensuring the structural stability of the compounds. Even at high temperatures, they can maintain good stability, breaking through the limitations of material use.

The term HEIC could date back to Tsai describing the multi-principal element intermetallic in 2016.²¹ HEICs are obtained through multi-principal element design of individual sublattices of traditional intermetallic compounds. In these novel materials, the volume fraction of the intermetallic phase reaches over 75%.³⁷ It has been suggested that ordered second-phase and multicomponent intermetallic compounds have been observed in many HEAs before obtaining single-phase HEICs.³⁸ Until 2017, T. P. Yadav *et al.*³⁹ successfully synthesized a high-entropy Ti–Zr–V–Cr–Ni alloy composed of five elements. The cast alloy is composed entirely of a micron-sized C14-type hexagonal structure Laves phase, while the rapidly solidified ribbon shows the presence of a nanostructure Laves phase. It was suggested that the Ti–Zr–V–Cr–Ni alloy has no signs of the presence of amorphous or other metastable phases. This is the first reported single-phase HEIC. In 2019, Zhou *et al.*⁴⁰ successfully prepared a B2-type (Fe_{1/5}Co_{1/5}Ni_{1/5}Mn_{1/5}Cu_{1/5})Al HEIC by mechanical alloying and spark plasma sintering. In 2020, the application of the “interfacial disordered nanolayer induced ductilization” method in the preparation of HEICs demonstrated exceptional strength and tensile ductility, offering a novel approach for the fabrication of HEICs with superior comprehensive mechanical properties.²⁷ In 2023, Zhao *et al.*⁴¹ creatively utilized the ductility effect of interfacial disordered nanolayers to develop Co-rich HEICs, effectively overcoming the trade-off between strength and ductility. Furthermore, research indicates that the micro-segregation of elements in high-entropy sublattices is related to the properties of the constituent elements, their interactions, and the characteristics of melt crystallization.²²

2.2 Methods for predicting the phase structure and mechanical properties of high-entropy intermetallic compounds

HEICs are the latest typical representatives of high-entropy materials, which provide a new paradigm for the development of new high-entropy materials with unusual properties.⁴² Laves phases are the most extensive category of inter-metallic compounds and have significant potential for practical and structural applications. Specifically, previous reports on Cr–Nb–Ti–V–Zr and Al–Cr–Nb–Ti–V alloys have indicated that the formation of Laves phases allows the alloys to maintain high strength at temperatures as high as 1000 °C.^{43,44} Therefore, the prediction of the phase structure and mechanical properties of HEICs can expedite the discovery of novel HEICs with splendid mechanical properties.

2.2.1 δ^* Criterion. The structured B2 HEICs exhibit similarities to HECs in that one element, aluminum in this instance, which predominantly occupies one sublattice, while the

remaining four or five elements form a solid solution on the other sublattice. In addition, previous research has indicated that the atomic size difference of cationic atoms and the cation–anion bond length are considered important parameters for predicting the formation of single-phase HECs.^{45,46} Inspired by this, Zhou *et al.*⁴⁰ proposed the use of atomic size dispersion δ^* of non-Al elements as a key parameter for predicting the single-phase high-entropy B2 structure, which can be expressed as

$$\delta^* = 100 \sqrt{\sum_{i \neq \text{Al}} c_i (1 - r_i / \bar{r}_{\text{non-Al}})^2} \quad (1)$$

It was suggested that $\delta^* < 1$ can be a favorable indicator for facilitating the formation of a single B2 phase consisting of four to five components with nearly equal molar compositions.

2.2.2 $\Delta\chi_{\text{A}-\text{B}_j} - \delta_{\text{A}-\text{B}_j}$ criterion. It has been suggested that atomic radius and electronegativity are two important parameters for the formation of intermetallic phases.^{40,47} Ostovari *et al.*⁴² proposed two modified parameters, the sublattice electronegativity difference ($\Delta\chi_{\text{A}-\text{B}_j}$) and atomic size differences ($\delta_{\text{A}-\text{B}_j}$) as new indicators for the formation of a single high-entropy phase in ordered AB ICs. In order to describe the effect of electronegativity of atoms filling distinct sub-lattices in the semi-ordered crystal structure of (A₁, A₂, A₃...A_n)_x(B₁, B₂, ...B_m)_y HEICs, the sublattice electronegativity difference is defined as

$$\Delta\chi_{\text{A}-\text{B}_j} = 100 \sqrt{\sum_{j \neq \text{A}} c_j \sum_{i \neq \text{B}} c_i (1 - e_i / e_j^{\text{B}})^2} \quad (2)$$

where c_i , e_i , c_j and e_j are the atomic fractions and Pauling's electronegativity of the atoms occupying A and B sublattices in the crystal structure respectively. In addition, the atomic size difference of the sublattice is denoted as

$$\delta_{\text{A}-\text{B}_j} = 100 \sqrt{\sum_{j \neq \text{A}} c_j \sum_{i \neq \text{B}} c_i (1 - r_i / r_j^{\text{B}})^2} \quad (3)$$

where r_i and r_j are the atomic sizes of the atoms occupying A and B sublattices. The findings indicate that higher $\Delta\chi_{\text{A}-\text{B}_j}$ can promote the formation of single-phase HEICs. For the B2 phase with equimolar AB compositions, a single high entropy phase forms when $5 < \delta_{\text{A}-\text{B}_j} < 6$, and $\Delta\chi_{\text{A}-\text{B}_j} > 7$. A single high entropy phase is obtained over a relatively larger range of $\Delta\chi_{\text{A}-\text{B}_j}$ and $\delta_{\text{A}-\text{B}_j}$ parameters ($\Delta\chi_{\text{A}-\text{B}_j} \geq 7.13$ and $6.05 \leq \delta_{\text{A}-\text{B}_j} \leq 9.57$) for the Laves phase.

2.2.3 $\delta_r - \Delta\chi_{\text{Allen}}$ criterion. It was proposed that the formation of the Laves phase can be predicted through atomic size mismatch (δ_r) and the difference in Allen electronegativity parameters ($\Delta\chi_{\text{Allen}}$).⁴⁷ The δ_r can be calculated using the following formula:

$$\delta_r = 100\% \sqrt{\sum c_i (1 - r / \bar{r})^2} \quad (4)$$

$$\bar{r} = \sum c_i r_i \quad (5)$$

where c_i and r_i are the atomic fraction and atomic radius of element i , respectively. Furthermore, the Allen electronegativity difference ($\Delta\chi_{\text{Allen}}$) can be expressed as

$$\Delta\chi_{\text{Allen}} = \sqrt{\sum_{i=1}^n c_i (1 - \chi_i^{\text{Allen}}/\chi_a)^2} \quad (6)$$

$$\chi_a = \sum c_i \chi_i^{\text{Allen}} \quad (7)$$

where χ_i^{Allen} is the Allen electronegativity of element i and χ_a is the average Allen electronegativity. The formation of intermetallic Laves phases occurs when $\delta_r > 5.0\%$ and $\Delta\chi_{\text{Allen}} > 5.0\%$, as determined through analysis (Fig. 5(a)).

2.2.4 $\eta - \delta$ criterion. According to the research conducted by Guo *et al.*,⁴⁸ the significant impact of the difference in electronegativity on the formation of intermetallic compounds has been observed. Furthermore, it was suggested that a larger electronegativity difference promotes the formation of intermetallic bonds, such as Fe–Al and Ni–Al.²⁴ Yao *et al.*²⁴ proposed the use of differences in electronegativity (η) and atomic size (δ) to understand the fundamental phase formation patterns of HEICs. Previous calculations of the electronegativity difference neglected the direct electronegativity differences between neighboring atoms. Yao *et al.* proposed a new parameter η to better describe how the electronegativity of central atoms is influenced by neighboring atoms, which can be expressed as

$$\eta = \sqrt{\sum_{i=1}^n c_i \left[\sum_{j=1}^{\mu} (e_i - e_j)^2 \right]} \quad (8)$$

where $e_i - e_j$ is the direct Pauling's electronegativity difference between a central and neighbor atom, the probability coefficient. μ is denoted as

$$\mu = \frac{c_j V_m j^{2/3}}{\sum V_m j^{2/3}} \quad (9)$$

where V_m is the molar volume. The δ can be calculated using formula (4). After conducting statistical analysis, it was found

that full intermetallic compounds tend to form when $0.2 < \eta < 0.4$ and $\delta \geq 5.5$ (Fig. 5(b)).

2.2.5 $\Delta\chi_{A_i-B_j} - \delta^*$ criterion. In order to address the prediction of the single-phase structure of newly developed HEICs, a criterion based on the electronegativity difference of sub-lattices has been proposed.⁴⁹ This criterion aims to better describe the impact of the electronegativity of atoms occupying different sub-lattices within the semi-ordered crystal structure of $(A_1, A_2, A_3 \dots A_n)_x (B_1, B_2, \dots B_m)_y$ MEICs (medium high entropy intermetallic compounds)/HEICs. The variable $\Delta\chi_{A_i-B_j}$ can be represented by formula (2). The dispersion of atomic sizes of elements occupying high-entropy sites, denoted as δ^* , is represented by the following equation:

$$\delta^* = 100 \sqrt{\sum_{i \neq B}^n c_i \left(1 - \frac{r_i}{\bar{r}_{\text{site A}}} \right)^2} \quad (10)$$

Fig. 6 illustrates the $\Delta\chi_{A_i-B_j} - \delta^*$ diagram. As depicted in Fig. 6, a single phase is formed when $\Delta\chi_{A_i-B_j} \geq 5$ and $1.2 \leq \delta^* \leq 3.3$. It was suggested that a high sublattice electronegativity difference ($\Delta\chi_{A_i-B_j} \geq 5$) promotes the formation of single phase HEICs.

2.2.6 Machine learning. Due to its superior capabilities in data processing, machine learning (ML) has emerged as a significant tool in the field of materials science. Recently, a novel approach for exploring HEIC phase structures was proposed by Huang *et al.*,⁵⁰ which involves initially utilizing empirical guidelines and ML for preliminary predictions. The proficient artificial neural network (ANN) model was derived from the research conducted by previous research.⁵¹ As illustrated in Fig. 7, the input layer of the ML model comprises 13 neurons, while the output layer consists of a single neuron dedicated to outputting the recognition results of HEIC phase structures.

The empirical criteria and results of the ML model suggest that the HEIC AlTiCuCo is expected to manifest in the form of AM or IM phases, and based on the calculated E_m , it is more likely to adopt the L1₂ structure rather than the B2 structure.

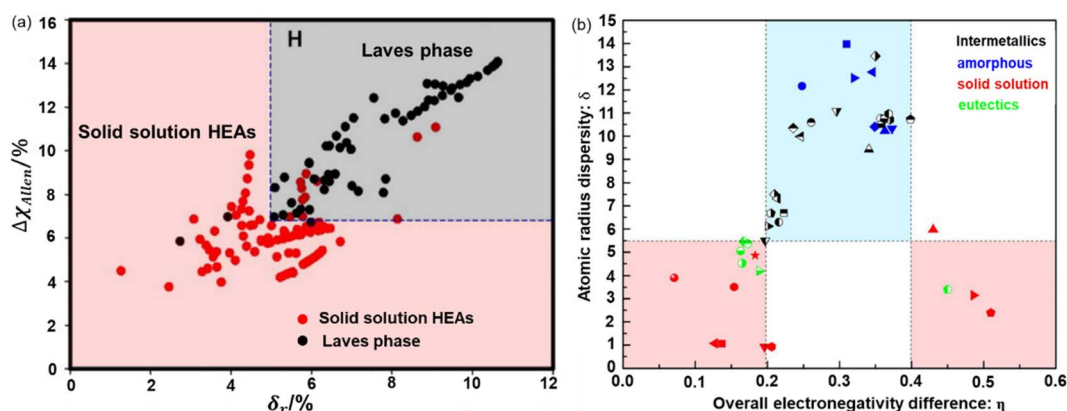


Fig. 5 (a) Relationship between parameters δ_r and $\Delta\chi_{\text{Allen}}$. Reproduced from ref. 47 with permission from Sage Publications, copyright 2017; (b) the $\delta - \eta$ plot delineating the phase selection of multicomponent alloys. Reproduced from ref. 24 with permission from Elsevier, copyright 2020.

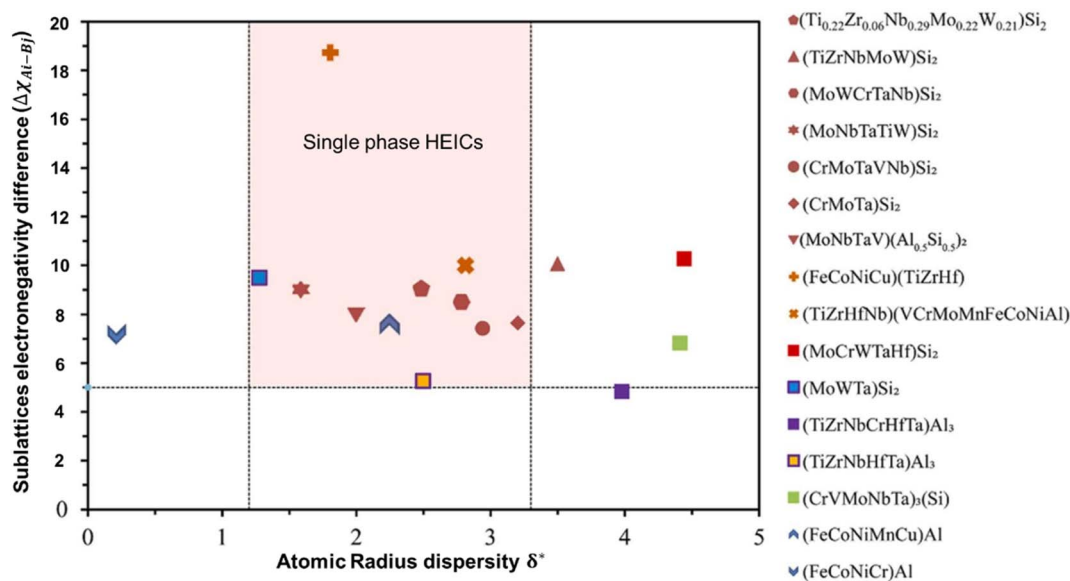


Fig. 6 The $\Delta\chi_{A-B} - \delta^*$ map outlining the single-phase formation in MEICs/HEICs. Reproduced from ref. 49 with permission from Elsevier, copyright 2022.

The term “mixing energy E_m ” is commonly employed to characterize phase stability and formability and can be calculated using the following formula:⁵⁰

$$E_m = \frac{E_{\text{total}} - E_{\text{atoms}}}{n} \quad (11)$$

where E_{total} and E_{atoms} represent the total energy of the cell.

2.3 Mechanical properties of high-entropy intermetallic compounds

2.3.1 Hardness. It has been suggested that alloying has a significant impact on the hardness of HEICs. Scientists examined the influence of Cr content on the microstructures and hot hardness of the $\text{AlCoCr}_x\text{FeMo}_{0.5}\text{Ni}$ HEIC ($x = 0-2.0$).⁵² As the numerical value of x increases from 0 to 2, there is a corresponding increase in the hardness of the alloy from Hv 601 to Hv 867. This phenomenon can be ascribed to the emergence of the hard σ phase, which is a result of the heightened Cr content. Similarly, the hardness of the B2-ordered $\text{Ti}_2\text{ZrHf}_{0.5}\text{VNi}_{0.5}\text{Al}_x$ HEIC shows a linear increment as a function of x .²³

Additionally, the structure also plays a considerable role in the hardness of HEICs and should not be overlooked. Ostovari *et al.*⁴² synthesized $(\text{Ni}_{0.2}\text{Co}_{0.2}\text{Fe}_{0.2}\text{Cu}_{0.2}\text{Mn}_{0.2})_3(\text{Al}_{0.5}\text{Ti}_{0.5})$ to

study the microstructure and hardness. The experimental findings indicate that the microhardness value of the dendritic B2 phase in $(\text{Ni}_{0.2}\text{Co}_{0.2}\text{Fe}_{0.2}\text{Cu}_{0.2}\text{Mn}_{0.2})_3(\text{Al}_{0.5}\text{Ti}_{0.5})$ is 1.5 times greater than that of the interbranch region.

2.3.2 Elevated temperature properties. Intermetallic alloys possessing long-range ordered structures are considered highly promising materials for use under high-temperature conditions, owing to their exceptional yield strength when exposed to elevated temperatures.⁵³

During the oxidation process, the complex oxide structure formed by HEICs may potentially enhance its high-temperature oxidation performance. Hou *et al.*⁵⁴ systematically studied the high-temperature oxidation resistance and mechanism of a novel $\text{Ni}_{3.3}\text{Co}_{3.9}\text{Cr}_5\text{Al}_{12}\text{Mo}_2\text{Ti}_3\text{Ta}_2\text{Nb}_3\text{B}_1$ HEIC. The present HEIC demonstrates notably low rates of oxidation, measuring $8.7 \times 10^{-5} \text{ mg}^2 \text{ cm}^{-4}$ and $5.6 \times 10^{-4} \text{ mg}^2 \text{ cm}^{-4}$ per hour at temperatures of 900 °C and 1000 °C, respectively. The oxidation process of the HEIC results in the formation of a complex oxide structure, characterized by a multi-layered composition. The outer layer primarily consists of a multicomponent spinel oxide, while the middle layer contains a combination of (Ti, Nb, Ta)₂O₄-type oxides and boron oxides. Additionally, the inner layer is observed to be a continuous layer of Al₂O₃ at both 900 °C

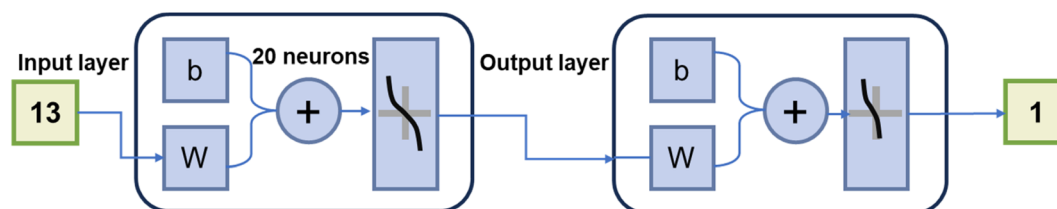


Fig. 7 The schematic illustration of a well-trained $13 \times 20 \times 1$ network for predicting the phase structure of AlTiCuCo. Reproduced from ref. 50 with permission from Elsevier, copyright 2022.

and 1000 °C. The Al_2O_3 layer contributes to the excellent oxidation resistance. A novel $\text{Fe}_{0.75}\text{Co}_{0.75}\text{Ni}_{0.75}\text{Cu}_{0.75}\text{TiZrHf}$ HEIC exhibits remarkable stability in a high temperature environment, maintaining yield strengths of 905 MPa at 800 °C and 705 MPa at 900 °C.²⁴ Researchers produced a non-equiatomic HEIC with the chemical composition of $\text{Ti}_{16.5}\text{Zr}_{17}\text{Hf}_{16.5}\text{Co}_{16.5}\text{Ni}_{16.5}\text{Cu}_{17}$, which predominantly crystallized in a B2 structure and contained a minor quantity of $\text{Cu}_{10}\text{Zr}_7$ precipitates.²⁵ The HEIC demonstrated remarkable thermal stability, maintaining a strength of around 1220 MPa and a fracture strain of approximately 20% at a temperature of 873 K, which can be ascribed to the stability of the B2 phase.

2.3.3 Strength and ductility. Yao *et al.*²⁴ successfully prepared a $\text{Fe}_{0.75}\text{Co}_{0.75}\text{Ni}_{0.75}\text{Cu}_{0.75}\text{TiZrHf}$ HEIC, which demonstrated exceptional compressive strength (2.25 GPa) and fracture strength (2.52 GPa). The $\text{Fe}_{0.75}\text{Co}_{0.75}\text{Ni}_{0.75}\text{Cu}_{0.75}\text{TiZrHf}$ HEIC demonstrates remarkable strength, attributed in part to its distinctive fully intermetallic-matrix-based HEA composition. This composition is characterized by a significant presence of covalent and metallic bonds, as opposed to a singular metallic bond. The $\text{Co}_{25}\text{Ni}_{25}(\text{HfTiZr})_{50}$ HEIC possesses a significantly distorted lattice structure and intricate atomic-level chemical order.⁵⁵ As a result of its composite structures, this alloy demonstrates a notably elevated energy barrier, effectively impeding dislocation movement and consequently displaying exceptional yield strength (1.96 GPa). The $\text{Ti}_{16.5}\text{Zr}_{17}\text{Hf}_{16.5}\text{Co}_{16.5}\text{Ni}_{16.5}\text{Cu}_{17}$ HEIC with metastable amorphous (am) and B2 phases demonstrated an excellent compressive fracture strength of approximately 2.25 GPa and fracture strain of about 8%.²⁵ The as-spun ribbons, consisting of both amorphous and [am + B2] phases, demonstrate favorable bending plasticity.

A novel AlNbTiVZr_x ($x = 0, 0.1, 0.25, 0.5, 1, 1.5$) alloy was prepared to investigate the structure and mechanical properties.³¹ The compressive yield strength demonstrated an increase with the increase in Zr content, reaching 1000 MPa for the AlNbTiV alloy and 1535 MPa for the $\text{AlNbTiVZr}_{1.5}$ alloy. Concurrently, the plasticity increased from 6% for the AlNbTiV alloy to over 50% for the $\text{AlNbTiVZr}_{0.5}$ alloy, subsequently declining to 0.4% for the $\text{AlNbTiVZr}_{1.5}$ alloy. Qiao *et al.*²³ synthesized a series of novel B2-ordered $\text{Ti}_2\text{ZrHf}_{0.5}\text{VNb}_{0.5}\text{Al}_x$ HEICs. As the variable x progresses from 0 to 1, there is a notable increase in the value of yield strength, increasing from 915 MPa to 1410 MPa, representing an approximate 54% increase. In addition, the compressive fracture strain maintains a level exceeding 50% for x values up to 0.5. We have collected and organized some mechanical properties of high-entropy intermetallic compounds in Table 1, hoping to accelerate the design of high-performance high-entropy intermetallic compounds.

2.3.4 Elasticity. Intermetallic compounds have been widely utilized in the automotive and aerospace industries due to their exceptional shape memory effect. Nevertheless, conventional shape memory alloys (SMAs) exhibit a limited spectrum of phase transition temperatures, and the formation of dislocations and precipitates at elevated temperatures results in inadequate thermal cycling stability, rendering them unsuitable for use under highly demanding service conditions.^{59,60}

The introduction of the concept of high entropy has significantly propelled the advancement of SMAs. Presently, a range of novel high-entropy shape-memory alloys (HEMSAs) have been designed utilizing TiNi, Fe-based, Ti-based, and NiMn-based alloy compositions.⁶¹ Peltier *et al.*⁶² established a relationship between the forward martensitic transformation starting temperature (T_{Ms}) in a HESMA and its chemical composition. It was suggested that the elements Hf, Zr, Fe, and Al are associated with an increase in T_{Ms} , while Co, Cu, and Ti are linked to a decrease in T_{Ms} . The correlation between the chemical composition and forward martensitic transformation starting temperature offers valuable insights for the development of HESMAs. At a temperature of 443 K, HESMA $\text{Ti}_{25}\text{Zr}_{10}\text{Hf}_{15}\text{Ni}_{25}\text{Cu}_{25}$ demonstrates excellent yield strength (>1680 MPa) and is capable of fully recovering strain upon stress unloading.⁶³ Canadinc *et al.*⁶⁴ conducted a study on a series of HESMAs, proposing that the high configurational entropy of the alloy may contribute to the enhancement of transformation temperature, transformation stress, and strain recovery at high temperatures. Specifically, the transformation temperature of HESMA $(\text{TiZrHf})_{50}(\text{NiPd})_{50}$ exceeds 973 K, and in addition, alloys $\text{Ni}_{25}\text{Pd}_{25}\text{Ti}_{25}\text{Hf}_{25}$ and $\text{Ni}_{35}\text{Pd}_{15}\text{Ti}_{30}\text{Hf}_{20}$ also exhibit a certain degree of high-temperature super-plasticity.

2.4 Strengthening/toughening of HEICs

Intermetallic compounds (ICs) have metallic, ionic and covalent hybrid bonds. Therefore, ICs are more resistant to diffusion-driven phenomena such as dislocation climb, grain boundary slipping and grain growth. This results in ICs exhibiting ultra-high temperature strength and stability.²²

With the rapid development of industries such as aerospace, high-speed transportation, and advanced weaponry, there is an increasing demand for high-temperature structural materials. The excellent strength and high-temperature stability exhibited by ICs align with this requirement. Furthermore, the introduction of the high-entropy concept has provided a broader space for intermetallic compounds to demonstrate even more outstanding mechanical properties. However, the inferior ductility/toughness significantly hinder the widespread application of ICs and HEICs in the field of high-temperature structures.

Extensive research has been conducted on the toughening of ICs. In the 1990s, inspired by the multi-layered structure of shells, Vecchio *et al.*⁶⁵ developed novel $\text{Ti-Al}_3\text{Ti}$ laminate composites, consisting of alternating layers of high-strength, low-toughness Al_3Ti and high-toughness Ti, in the form of a metallic/intermetallic compound laminate composite material. It has been suggested that the $\text{Ti-Al}_3\text{Ti}$ laminate composite demonstrate outstanding performance; thus using layered composites is considered to be one of the important strategies for toughening ICs. In addition, the effective measure of enhancing the toughness of ICs is also achieved through the utilization of *in situ* reactions to generate dispersed reinforcing phases.^{66–68} Simultaneously, the reinforcement of ICs through the use of whisker/fiber and fine grain strengthening/toughening is also considered a viable approach.^{69–71}

Table 1 Mechanical properties of high-entropy intermetallic compounds^a

HEICs	Condition	Phase	Hardness	Ultimate tensile strength (MPa)	Yield strength (MPa)	Elongation ϵ (%)	Ref.
AlCoCr _x FeMo _{0.5} Ni ($x = 0$, RT)	AC	B2 + σ	Hv 601	—	—	—	52
AlCoCr _x FeMo _{0.5} Ni ($x = 2$, RT)	AC	B2 + σ	Hv 867	—	—	—	52
AlCoCr _x FeMo _{0.5} Ni ($x = 1.5$, 1000 °C)	AC	B2 + σ	Hv 374	—	—	—	52
AlCoCr _x FeMo _{0.5} Ni ($x = 2$, 1000 °C)	AC	B2 + σ	Hv 450	—	—	—	52
AlNbTiVZr _x ($x = 0$, RT)	AM-AN 1200°C/24 h	B2	—	—	1000 (Compressive)	6	31
AlNbTiVZr _x ($x = 0$, 600 °C)	AM-AN 1200°C/24 h	B2	—	—	780 (Compressive)	14.3	
AlNbTiVZr _x ($x = 0$, 800 °C)	AM-AN 1200°C/24 h	B2	—	—	560 (Compressive)	>50	
AlNbTiVZr _x ($x = 0.5$, RT)	AM-AN 1200°C/24 h	B2	—	—	1485 (Compressive)	>50	31
AlNbTiVZr _x ($x = 0.5$, 600 °C)	AM-AN 1200°C/24 h	B2 + Zr ₅ Al ₃ + C14	—	—	1135 (Compressive)	7.5	
AlNbTiVZr _x ($x = 0.5$, 800 °C)	AM-AN 1200°C/24 h	B2 + Zr ₅ Al ₃ + C14	—	—	675 (Compressive)	>50	
AlNbTiVZr _x ($x = 1.5$, RT)	AM-AN 1200°C/24 h	B2 + Zr ₅ Al ₃ + C14	—	—	1535 (Compressive)	0.4	31
AlNbTiVZr _x ($x = 1.5$, 600 °C)	AM-AN 1200°C/24 h	B2 + Zr ₅ Al ₃ + C14	—	—	1195 (Compressive)	>50	
AlNbTiVZr _x ($x = 1.5$, 800 °C)	AM-AN 1200°C/24 h	B2 + Zr ₅ Al ₃ + C14	—	—	180 (Compressive)	0	
AlNbZrTi _x ($x = 1$)	IM-AN1200°C/5 h	B2 + Zr ₅ Al ₃	—	—	1579 (Compressive)	17.8	30
AlNbZrTi _x ($x = 2$)	IM-AN1200°C/5 h	B2	—	—	1227 (Compressive)	21.8	30
AlNbZrTi _x ($x = 3$)	IM-AN1200°C/5 h	B2	—	—	1111 (Compressive)	>50	30
Al _{0.25} FeCoNiV	AM	B2 + L1 ₂	—	1530	1100 (Tensile)	20	29
Ti ₂ ZrHf _{0.5} VNb _{0.5} Al _x ($x = 0$)	AM	BCC	Hv 309.8	—	915 (Compressive)	>50	23
Ti ₂ ZrHf _{0.5} VNb _{0.5} Al _x ($x = 0.5$)	AM	B2	Hv 375.7	—	1159 (Compressive)	>50	23
Ti ₂ ZrHf _{0.5} VNb _{0.5} Al _x ($x = 1.0$)	AM	B2	Hv 460.0	—	1410 (Compressive)	15.1	23
Fe _{0.75} Co _{0.75} Ni _{0.75} Cu _{0.75} TiZrHf (RT)	AM	B2	Hv 600	2520	2250 (Compressive)	2.5	24
Fe _{0.75} Co _{0.75} Ni _{0.75} Cu _{0.75} TiZrHf (400 °C)	AM	B2	—	2230	1770(Compressive)	3	24
Fe _{0.75} Co _{0.75} Ni _{0.75} Cu _{0.75} TiZrHf (600 °C)	AM	B2	—	—	1500 (Compressive)	8	24
Fe _{0.75} Co _{0.75} Ni _{0.75} Cu _{0.75} TiZrHf (800 °C)	AM	B2	—	—	905 (Compressive)	33	24
Fe _{0.75} Co _{0.75} Ni _{0.75} Cu _{0.75} TiZrHf (900 °C)	AM	B2	—	—	705 (Compressive)	28	24
Ti _{16.5} Zr ₁₇ Hf _{16.5} Co _{16.5} Ni _{16.5} Cu ₁₇	AM	B2 + Cu ₁₀ Zr ₇	—	—	1440 (Compressive)	8	25
TiZrVCrNiFe _x	AM	C14	Hv 1444	—	—	—	56
TiZrVCrNiFe _x ($x = 1$)	AM	C14	Hv 1417	—	—	—	56
TiZrVCrNiFe _x ($x = 2$)	AM	C14	Hv 1411	—	—	—	56
TiZrHfNiCu	AM	C14	—	—	1924 (Compressive)	2	28
ZrTiHfCuNiFe	Copper mold casting	B2	—	—	~1900 (Compressive)	6.1	57
Co _{2.5} Ni _{2.5} (HfTiZr) ₅₀	AM	—	—	—	1960 (Compressive)	—	55
FeCoNiV	Induction melting	L1 ₂	—	1100	398 (Compressive)	20	26
Co-30Ni-11Al-5.5W-4Ti-2.5Ta-0.10B	AM	L1 ₂	—	—	281 (Compressive)	0.42	58
Co-30Ni-11Al-5.5W-4Ti-2.5Ta-0.10B	AM	L1 ₂	—	—	709 (Compressive)	0.32	58
Ni _{4.3} Co _{22.4} Fe _{8.8} Al _{10.7} Ti _{11.7} B _{2.5}	AM	L1 ₂ + FCC	—	1611	1040 (Tensile)	25	27

^a AC-as-cast; AN-annealing; AG-aging; AM-arc melting; RT-room temperature; IM-introducing melt.

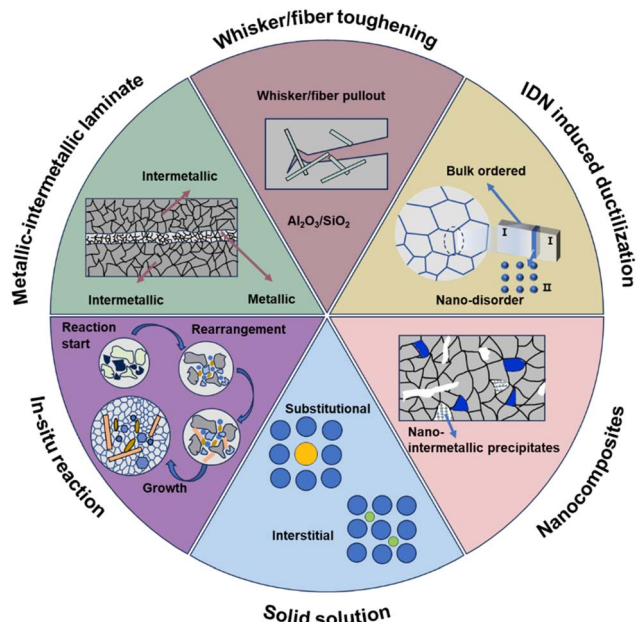


Fig. 8 Diagram illustrating part of the strengthening/toughening strategies for ICs and HEICs.

Currently, there is a limited amount of research on the toughening of HEICs. It is believed that toughening strategies for HEICs can draw inspiration from traditional toughening methods for ICs, such as whisker/fiber and fine grain strengthening/toughening. Fig. 8 illustrates some of the strengthening/toughening strategies which have been employed in ICs and HEICs. We aim for Fig. 8 to assist readers in gaining a better understanding of the strengthening/toughening strategies discussed in Section 2.4. We have compiled the current strengthening/toughening strategies of HEICs, with the aim of inspiring scholars to accelerate the research and design of high-performance HEICs.

2.4.1 Strengthening/toughening of nanocomposites. A dual-phase high-entropy nanocomposite (DHENC) material, consisting of high-entropy nano-intermetallic precipitates (HENIPs) and high-entropy nanoscale solid solution domains (HENSsDs), demonstrates elevated tensile yield strength (1.23 GPa) and exceptional ductility ($\sim 19\%$).⁷² The iso-concentration surfaces of Ni, Al, and Ti revealed the existence of HENIPs, with the high-density HENIPs being evenly dispersed across the volume of the three-dimensional reconstruction at the tip of the sample (Fig. 9(a)). Due to the slight lattice mismatch between the nanoscale precipitate particles and the FCC matrix phase, the order strengthening will result in a significant enhancement of the yield strength. According to calculations, the strength of the DHENC has increased by approximately 0.81 GPa due to the presence of nano-intermetallic precipitates. Furthermore, the evolution of multiple dislocation types during the deformation process is considered to be the primary reason for its high ductility. This deformation stage includes predominant features such as dislocation plane slip (Fig. 9(b)), coplanar dislocation arrays (Fig. 9(c)), dislocation walls (Fig. 9(d)),

microbands (Fig. 9(e)), and stacking faults in solid solution domains (Fig. 9(f)).

2.4.2 Solid solution strengthening. A novel $\text{Fe}_{0.75}\text{Co}_{0.75}\text{Ni}_{0.75}\text{Cu}_{0.75}\text{TiZrHf}$ HEIC ($T_{0.75}$) demonstrated an exceptional compressive yield strength of 2.25 GPa and fracture strength of 2.52 GPa.²⁴ Furthermore, $T_{0.75}$ also demonstrates excellent high-temperature phase stability, maintaining yield strengths of up to 905 MPa and 705 MPa at 800 °C and 900 °C, respectively. As depicted in Fig. 9(g), $T_{0.75}$ demonstrates excellent room-temperature compressive strength compared with other materials. The exceptional strength exhibited by $T_{0.75}$ can be attributed to the presence of seven primary elements in close to equimolar ratios, leading to more pronounced lattice distortion and solid solution strengthening compared to most HEAs. Very recently, the multi-principal $\text{Co}_{1.7}\text{Cu}_{1.7}\text{TiZrHf}$ HEIC ($A_{1.7}$) with a single B2 phase exhibits exceptional compressive yield strength (1.77 GPa) and fracture strength (2.15 GPa) at room temperature.⁷³ Furthermore, $A_{1.7}$ maintains an elastic strain limit of approximately 1.5% at such high strength. Fig. 9(h) and (i) illustrate the microstructural characteristics of $A_{1.7}$. It was suggested that the primary reasons for the elevated strength exhibited by $A_{1.7}$ are solid solution strengthening and grain boundary strengthening. To quantify the solid solution strengthening effect, the density-related parameter specific yield strength of $A_{1.7}$ was calculated. The specific yield strength can be computed using the following equation:

$$\text{SYS} = \sigma_y / \rho_{\text{mix}} \quad (12)$$

$$\rho_{\text{mix}} = \frac{\sum c_i A_i}{\sum c_i A_i / \rho_i} \quad (13)$$

where σ_y , A_i , and ρ_i are yield strength, atomic weight and the density of the i th element, respectively. Based on the calculated results, the specific yield strength of A is 209.4 kPa m³ kg⁻¹. Simultaneously, the high-entropy effect exhibited by $A_{1.7}$ and the single-phase B2 structure also contribute to a certain degree of enhancement in strength.

2.4.3 Interfacial disordered nanolayer induced ductilization. The $\text{Ni}_{43.9}\text{Co}_{22.4}\text{Fe}_{8.8}\text{Al}_{10.7}\text{Ti}_{11.7}\text{B}_{2.5}$ HEIC prepared using the “interfacial disordered nanolayer induced ductilization” method exhibits exceptionally high strength (~ 1.6 GPa) and tensile ductility ($\sim 25\%$).²⁷ From Fig. 10(a), we can clearly see interfacial disordering, which creates an ultrathin disordered layer along the grain boundary with an FCC solid-solution structure. It is suggested that the improvement in yield strength is attributed to the high antiphase boundary energy of highly ordered superlattice grains, which plays a significant role in hindering the nucleation and motion of dislocations. Fig. 10(b) illustrates a schematic diagram of the nanoscale interfacially disordered structure. Moreover, due to the introduction of a plastic buffer nanolayer, the plastic deformation compatibility between adjacent ordered grains is greatly enhanced and the generation of micro-cracks along the boundary is effectively inhibited.²⁷

Zhao *et al.*⁴¹ creatively exploited the ductility effect of interfacial disordered nanolayers to develop a Co-rich HEIC ($\text{Co}_{47}\text{Ni}_{30}\text{Al}_{10}\text{V}_5\text{Ta}_4\text{Ti}_4$)_{99\text{B}_1} (at%, denoted as Co-rich HEIC hereafter).

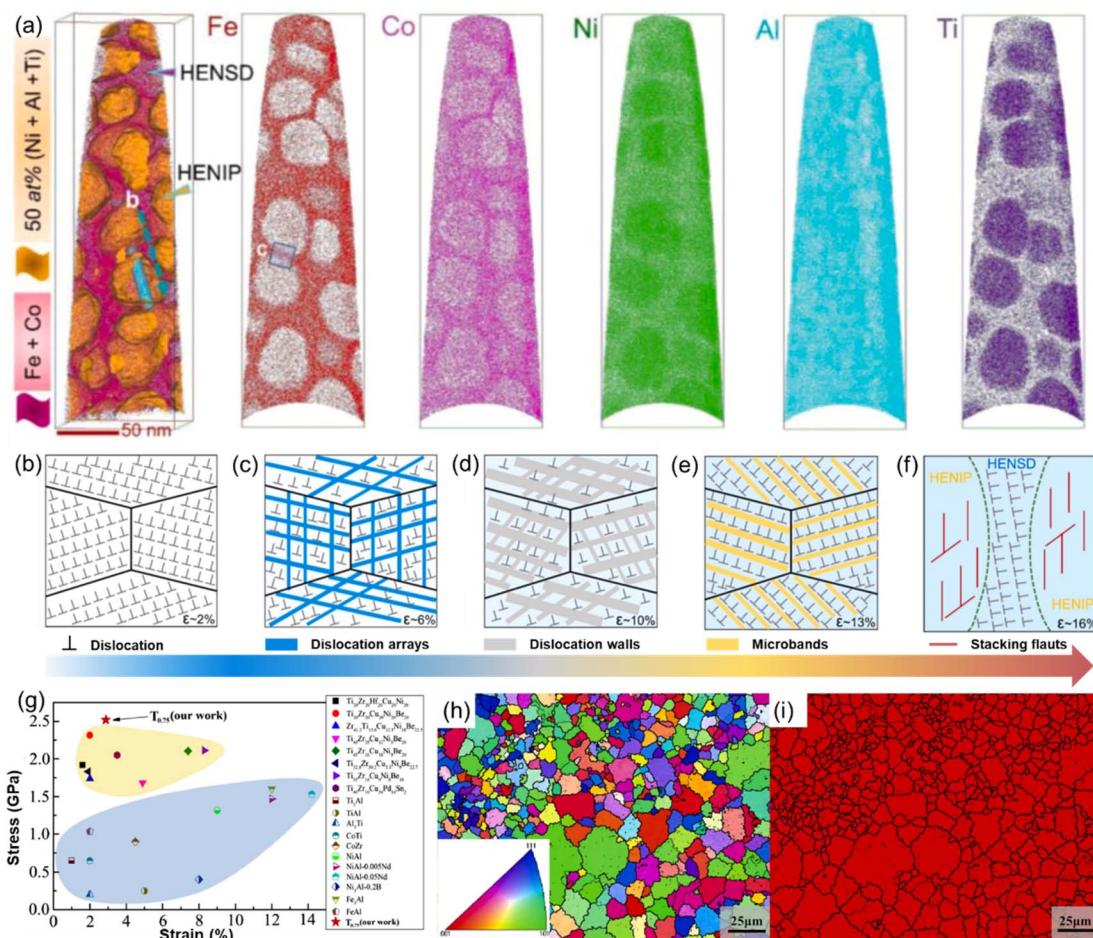


Fig. 9 (a) Three-dimensional (3D) reconstruction map of an atom probe tomography (APT) needle tip (the iso-concentration surface was constructed with an Ni + Al + Ti atomic ratio of 50%) of the DHENC, and 3D APT maps showing the distribution of each element (Fe, Co, Ni, Al, and Ti). Reproduced from ref. 72 with permission from Elsevier, copyright 2022; (b–f) schematic illustrations of the deformation mechanisms with multi-type dislocation substructure evolution. Reproduced from ref. 72 with permission from Elsevier, copyright 2022; (g) comparison of the room-temperature compressive properties of the $T_{0.75}$ HEIC, BMGs and conventional ICs. Reproduced from ref. 24 with permission from Elsevier, copyright 2020; (h and i) electron backscatter diffraction IPF image and phase distribution image of an $A_{1.7}$ alloy. Reproduced from ref. 73 with permission from Elsevier, copyright 2023.

As depicted in Fig. 10(c), clear disordered FCC nanolayers can be observed near the grain boundaries. The prepared Co-rich HEIC exhibits excellent yield strength (~ 748 MPa) and ultimate tensile strength (~ 1611 MPa), as well as exceptional ductility ($\sim 37\%$). Considering that the critical shear stress of the dislocation nucleus in the ordered $L1_2$ alloy is positively correlated with its antiphase boundary energy,⁷⁶ the antiphase boundary energy is significantly increased due to the addition of Ta, Ti and V elements, which causes an elevated impediment for dislocation motion and an increased strength consequently. Fig. 10(d) depicts three-dimensional reconstructions of a representative APT tip obtained from the Co-rich HEIC, revealing a prominently visible near-edge-on grain boundary. The excellent ductility exhibited by the $(\text{Co}_{47}\text{Ni}_{30}\text{Al}_{10}\text{V}_5\text{Ta}_4\text{Ti}_4)_{99}\text{B}_1$ HEIC may be ascribed to the synergistic impact of the material's high work-hardening capacity and enhanced fracture resistance resulting from the presence of interfacial disordered nanolayers at grain boundaries.

2.4.4 Lamellar-structure. A novel lamellar-structured (LS) $L1_2$ -type Co–Ni–Al–Ti–Ta–Nb–B-based HEIC was designed, which overcomes the trade-off of strength and plasticity.⁷⁴ The LS-HEIC exhibits an outstanding yield strength (~ 1007 MPa at temperature, ~ 1.2 GPa at 600–800 °C) and tensile elongation ($\sim 17\%$ at room temperature, $\sim 10\%$ at 600–800 °C). Previous studies have shown that the addition of elements such as Ti, Ta, and Nb causes an increase in the anti-phase boundary energy.^{77,78} In addition, it has been proven that the stacking of geometrically necessary dislocations will produce hetero-deformation induced stress, which also has a certain effect on the improvement of strength.⁷⁹ Furthermore, the reasonable tensile elongation exhibited by the LS-HEIC at temperatures ranging from 600 to 800 °C can be attributed to two underlying reasons. One of which is that, as illustrated in Fig. 10(e) and (f), the deformed LS-HEIC produces substantial paired dislocations and a high density of SISFs (superlattice intrinsic stacking faults) and SISF networks at 600 °C and 800 °C, respectively. According to previous research, SISFs will play a role in

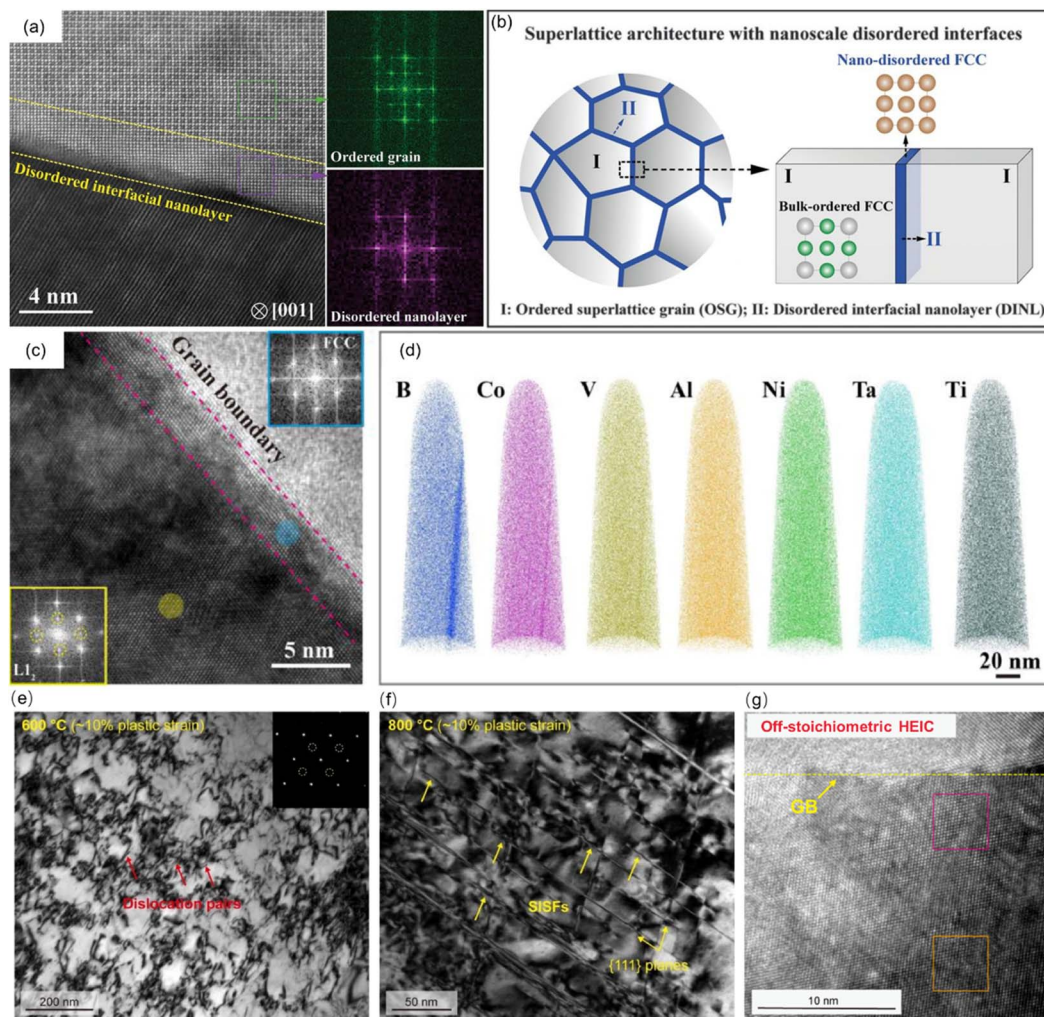


Fig. 10 Unusual nanoscale interfacially disordered structure of superlattice materials. (a) High-resolution HAADF-STEM image revealing the ultra-thin disordered layer at the grain boundaries with a nanoscale thickness. The images on the right show the corresponding fast Fourier transform (FFT) patterns. (b) Schematic illustration highlighting the nanoscale interfacially disordered structure. Reproduced from ref. 27 with permission from The American Association for the Advancement of Science, copyright 2020. (c) High-resolution TEM image and the insetted fast Fourier transform (FFT) revealing the interfacial disordered nanolayer formed at the grain boundary. (d) 3D reconstructions of individual element maps for an APT tip containing a grain boundary; deformation substructures of the LS-HEIC at intermediate temperatures (600 and 800 °C). Reproduced from ref. 41 with permission from Elsevier, copyright 2023; (e) dislocation configurations of the LS-HEIC deformed by ~10% plastic strain at 600 °C, indicating the generation of numerous dislocation pairs; (f) microstructures of the LS-HEIC deformed by ~10% plastic strain at 800 °C, showing deformation-induced high-density SISFs and SISF networks. Reproduced from ref. 74 with permission from Elsevier, copyright 2023; (g) typical high-resolution TEM imaging of the off-stoichiometric HEICs showing grain boundary structures between ordered L_{12} -type grains. Reproduced from ref. 75 with permission from Elsevier, copyright 2023.

hindering dislocations.⁸⁰ Accordingly, this ultimately leads to the LS-HEIC achieving enhanced work hardening and improved plastic deformation stability. Another reason is that after the tensile test, plastic deformation occurs parallel to the cylindrical interface, and stacked dislocations are preferentially formed at the boundary. This contributes to the formation of a large number of dislocation slip paths, which in turn improves tensile plasticity.⁷⁴

2.4.5 Off-stoichiometry-guided design. Prior research has reported that altering the stoichiometry of an alloy has a notable positive impact on the ductility of intermetallic alloys.^{81,82}

Xiao *et al.*⁷⁵ sought to investigate the potential for enhancing the ductility of high-strength HEICs through the modification

of the alloying stoichiometry. Off-stoichiometric HEICs exhibit an exceptionally high yield strength of 839 ± 2 MPa and excellent ultimate tensile strength of 1433 ± 17 MPa. Furthermore, these off-stoichiometric HEICs also display a substantial tensile elongation of $29 \pm 1\%$, in contrast to their stoichiometric HEIC counterparts which exhibit noticeable brittleness. As depicted in Fig. 10(g), the nanoscale disordered FCC phase in off-stoichiometry HEICs is also generated in the proximity of the grain boundary. It has been proposed that the presence of disordered FCC phases is significant in enhancing tensile plasticity through the elimination of intergranular embrittlement.²⁷ Furthermore, the disordered FCC phase aids in reducing the significant antiphase boundary barrier that

impedes the nucleation and movement of dislocations.⁸³ Consequently, the disordered FCC phases at the grain boundaries, induced by off-stoichiometry, effectively prevent premature intergranular fracture and lead to exceptional ductility at elevated strength levels.

3. High-entropy ceramics

3.1 Development history

Since 2015, Rost *et al.*⁹ first designed and prepared a high-entropy oxide (HEO) ceramic ($\text{Mg}_{0.2}\text{Zn}_{0.2}\text{Cu}_{0.2}\text{Co}_{0.2}\text{Ni}_{0.2}\text{O}$) with a rock-salt structure and confirmed the important role of high mixed entropy in phase stability. To date, extensive scholarly attention has been devoted to the study of high-entropy ceramics both domestically and internationally. A considerable array of high-entropy ceramic materials has been synthesized, and novel design principles have been introduced within this timeframe. In 2016, seven boride HECs with a density of about 92% were synthesized for the first time, all of which have better hardness and oxidation resistance than single-component diborides.⁴⁷ Biesuz *et al.*⁸⁴ prepared (MgNiCoCuZn)O powder with high sintering activity by chemical coprecipitation combined with the hydrothermal method using metal nitrate and sulfate as raw materials and sintered it without pressure at 1050 °C, which can make the prepared ceramic density reach up to 97%. Researchers have been striving to develop ceramic materials that are extremely hard and tough. Finally, scientists have prepared ($\text{Hf}_{0.2}\text{Nb}_{0.2}\text{Ta}_{0.2}\text{Ti}_{0.2}\text{Zr}_{0.2}\text{N}$) high-entropy nitride ceramics with extremely high hardness (up to 33 GPa) and fracture toughness ($5.2 \text{ MPa m}^{1/2}$)

by exothermic combustion of mechanically activated nano-structured metallic precursors in nitrogen, consolidated by spark plasma sintering.¹⁸ In addition, the sintering of HECs is challenging due to their robust covalent bonds and low diffusion coefficient, thereby imposing significant constraints on the widespread adoption of HECs on a large scale. A novel rapid liquid-phase assisted ultra-high temperature sintering strategy was proposed to overcome this challenge.⁸⁵

At present, high-entropy ceramic materials can be divided into high-entropy oxide ceramics, high-entropy carbide ceramics, high-entropy nitride ceramics, high-entropy boride ceramics and high-entropy silicide ceramics. High-entropy oxide ceramics not only have the excellent thermal and mechanical properties of traditional oxide ceramics, but also their various crystalline structures such as the rock salt structure, fluorite structure, spinel structure, perovskite structure and magnetite structure make high-entropy oxide ceramics show rich functional properties. Excellent performance makes high-entropy oxide ceramics show good application potential in high-temperature protective layers, magnetic materials and catalytic materials. Fig. 11 shows the comparison of the number of research papers on high-entropy oxide ceramics of different crystal forms, and it can be seen that among many high-entropy oxide ceramics, rock salt metal oxides and spinel-type metal oxide ceramics are the most widely studied.

3.2 Methods for predicting the phase structure and mechanical properties of high-entropy ceramics

High-entropy ceramics have been widely studied due to their superior mechanical properties and unique structure. However,

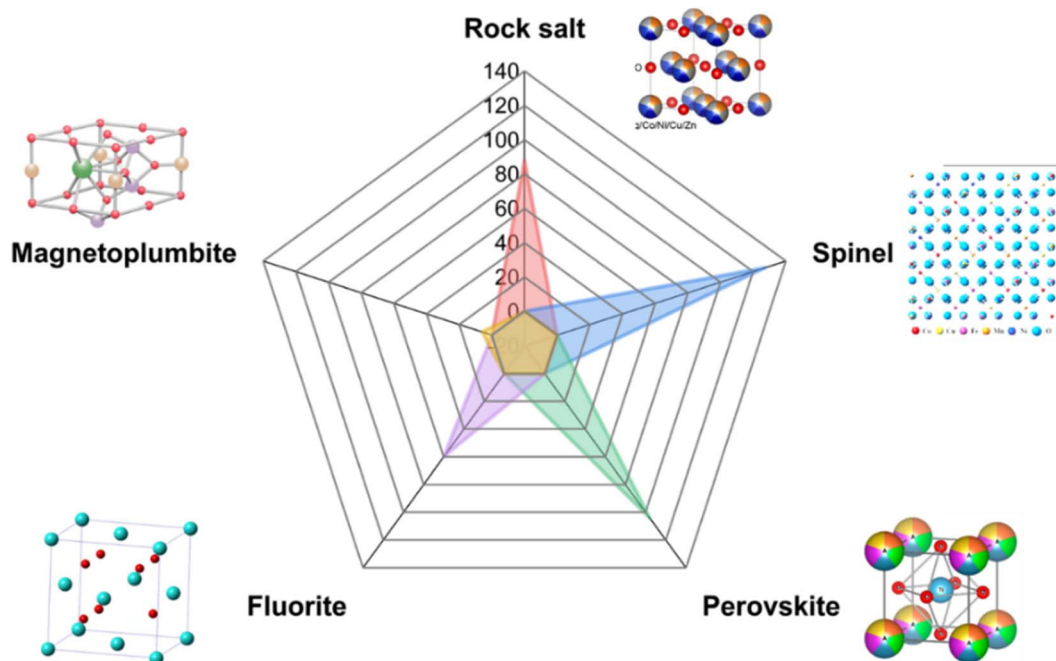


Fig. 11 The comparison of the number of research papers on high-entropy oxide ceramics with different crystal forms. Reproduced under the terms of the CC-BY 4.0 license. Copyright 2019, the authors, published by American Chemical Society.⁸⁶ Reproduced from ref. 87 with permission from Springer, copyright 2023; reproduced from ref. 88 with permission from Elsevier, copyright 2020; Reproduced from ref. 89 with permission from MDPI AG, copyright 2023.

the traditional trial-and-error method greatly limits the development of high-entropy ceramics. In this section, we have sorted out the relevant part of the research on the structure and mechanical property prediction of high-entropy ceramics, hoping to give researchers a general understanding of the prediction of high-entropy ceramic phase structures and mechanical properties.

3.2.1 ΔH_{form} criterion. Lu *et al.*⁹⁰ investigated the single-phase formation and mechanical properties of (TiZrNbTaMo)C with one equimolar and twenty non-equimolar systems using first-principles calculations. The scientists calculated the formation energies of all the samples. The formation energy ΔH_{form} can be expressed as

$$\Delta H_{\text{form}} = E_{\text{HEC}} - \sum_{i=1}^n c_i E_i \quad (14)$$

where E is the Density Functional Theory (DFT) ground-state energy and c_i is the molar fraction of the i th component. It was found that the ΔH_{form} values for all samples were negative, indicating that single-phase solid solutions can be prepared as long as there is enough energy to overcome the energy barrier. Furthermore, an analysis was conducted to examine the correlation between compositions, lattice constants, formation energy, VEC, and mechanical properties. This involved the calculation of the Pearson correlation coefficient and the creation of a heatmap illustrating the correlation between composition, structure, and elastic properties (Fig. 12(a)). The introduction of zirconium in a (TiZrNbTaMo)C system is not conducive to the formation of a single-phase solid solution phase, which probably can be attributed to the large lattice distortions and high formation energy of ZrC.⁹⁰ Based on the correlation heat map for “composition–structure–elastic properties”, researchers have also noted that Ti contributes to the stability of the crystal structure and the enhancement of hardness and Young's modulus, whereas Mo demonstrates a contrary effect. The occurrence of elemental segregation demonstrates that, alongside miscibility, entropy serves as the primary driving factor in the creation of solid solutions.⁹⁰ In good accord with the prediction results, the hardness and Young's modulus show a notable increase with increasing Ti content and a decreasing Mo concentration.

3.2.2 $\Omega - \delta_a$ criterion. The $\Omega - \delta$ criterion has demonstrated effectiveness in the prediction of HEAs. By utilizing first-principles calculations and thermodynamic principles related to configurational mixing entropy, researchers have developed a three-dimensional phase diagram that incorporates thermodynamic and structural variables, such as configurational mixing entropy and enthalpy. Liu *et al.*⁹⁵ recently extended the $\Omega - \delta_a$ criterion to high entropy carbide ceramic systems. Ω represents the formation of solid solution in HECs, as shown below:

$$\Omega = \frac{T_m \Delta S_{\text{mix}}}{|\Delta H_{\text{mix}}|} \quad (15)$$

where T_m is the melting point with the standard error. It has been proposed that when the value of Ω exceeds 1, a multi-component high entropy carbide has the potential to create

a single-phase solid solution based on thermodynamic principles. Furthermore, lattice constant differences, denoted as δ , are frequently employed to forecast the development of solid solutions within single-phase high entropy ceramics. The variation in lattice constants among the constituent carbides within high entropy carbides is delineated as follows:⁹⁶

$$\delta_a = \sqrt{\sum_{n=1}^N x_i \left[1 - a_i / \sum_{n=1}^N x_i a_i \right]^2} \quad (16)$$

where the lattice constant of the i th carbide component is denoted as a_i , with its molar fraction represented by x_i . It has been suggested that when both $\Omega > 1$ and $\delta_a < 6.6\%$ are satisfied, single solid solution high entropy carbides can be formed.

3.2.3 Machine learning methods. Due to its superiority, machine learning has achieved great success in many fields, especially in predictive materials, making it one of the tools in the field of materials science.⁹⁷ In Zhang *et al.*'s study, they developed a machine learning model to overcome the challenge of large phase spaces for the rational design of new high-performance HECs.⁹¹ Utilizing a proficiently trained model, the researchers examined approximately 90 un-synthesized high entropy ceramic carbides comprising 5 cations from groups IV, V, and VI of the periodic table. As a result, they successfully predicted 38 single-phase HECCs, and these prognostications closely align with the outcomes of the ongoing experimental investigations. In order to reduce overfitting caused by strongly correlated features and enhance prediction accuracy, the scientists removed features with Pearson coefficients higher than 0.9. Fig. 12(b) shows the feature selection for ML models. Previous studies have demonstrated that the metal elements in group IV and group V can form stable rock-salt structures with carbon as binary transition metal carbides (TMCs).^{98–100} According to the results, the scientists found that the elements in group IV/V have higher tendency in single phase HECCs. The Group VI elements (Cr, Mo, and W) are commonly found in multi-phase HECCs. In addition, due to Group VI elements having a higher valence filling, it is anticipated that the inclusion of these elements can lead to improved mechanical properties of HECCs.^{101,102} The study has come to some interesting conclusions. The VEC has been widely used to distinguish different phases of HEAs¹⁰³ and has been shown to play an important role in intermetallic phase formation.¹⁰⁴ However, it is noteworthy that the VEC is less effective in determining the formation of phases in HECCs.⁹¹ The scientists have identified σ_{VEC} (VEC deviation of constituent TMCs) and σ_χ (deviation of electronegativity of constituent TMCs) as key factors that influence the bonding properties and local atomic environment of metal elements in HECCs. These factors have been found to exert a substantial influence on the phase formation or separation of HECCs.⁹¹ This ML model proposed by Zhang is able to predict the possibilities of phase formation of equimolar and non-equimolar HECCs, which can accelerate the design of HECCs. While ML models show a lot of advantages, they also have some non-negligible shortcomings, that is, machine learning models require a large amount of high-quality data to achieve accurate prediction. Some researchers

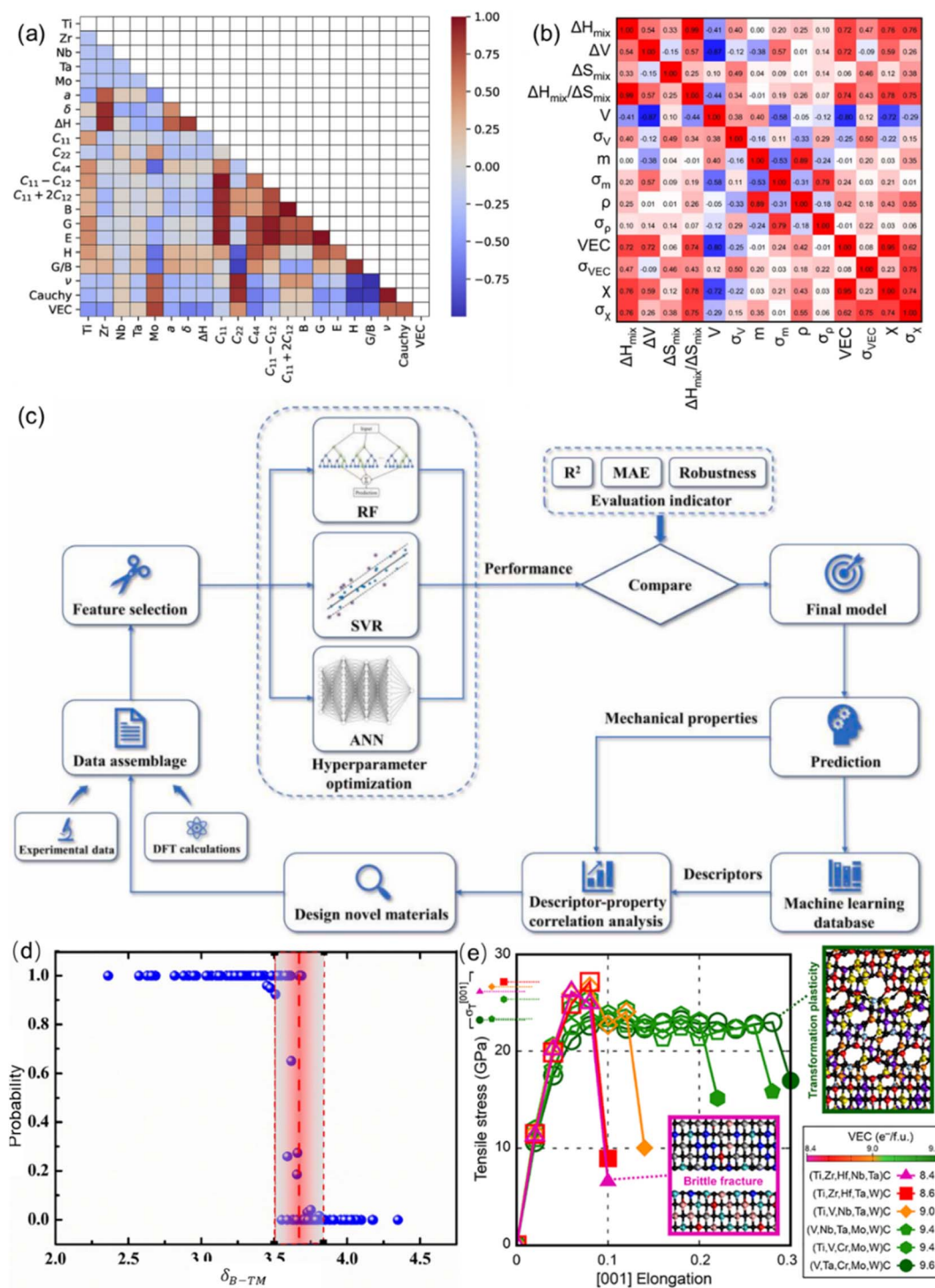


Fig. 12 (a) The “composition–structure–elastic properties” correlation heatmap of (TiZrNbTaMo)C. Reproduced from ref. 90 with permission from Elsevier, copyright 2021; (b) feature selection for ML models. Reproduced under the terms of the CC-BY 4.0 license. Copyright 2022, the authors, published by Springer Nature;⁹¹ (c) machine learning flowchart for the prediction of mechanical properties and descriptor-property correlation analysis of multicomponent ceramics. Reproduced from ref. 92 with permission from Elsevier, copyright 2022; (d) single phase formation probability of all compositions (training and test) predicted by the KNN model trained by δ_{B-TM} . When δ_{B-TM} approaches 3.66, marked as the red zone, HEBs can exist as a single or multiphase. Reproduced from ref. 93 with permission from Elsevier, copyright 2023; (e) *ab initio* molecular dynamics tensile properties and deformation mechanisms. Reproduced under the terms of the CC-BY 4.0 license. Copyright 2022, the authors, published by the American Association for the Advancement of Science.⁹⁴

have noticed this problem and are committed to circumventing it.

3.2.4 $\bar{\chi}$ criterion. In this case, more and more studies start with ML models to predict the phase formation ability, hardness, Young's modulus and other related performance parameters of HECs. There are scholars who established a high-precision machine learning model to predict the Young's modulus, hardness and wear resistance of high-entropy carbides.⁹² The diagram in Fig. 12(c) depicts the machine learning framework used to forecast the mechanical properties and examine the correlations between descriptors-properties of HECs. In order to determine the predominant features during the prediction process, scientists used the permutation importance calculation method. To minimize accidental errors and enhance the precision of the calculation importance, each feature was randomly rearranged with 10 different orders ($K = 10$). The three most influential factors in predicting Young's modulus were determined to be δ_{T_m} (deviation of melting temperatures), \bar{E}_{total} (fraction-weighted mean total energy of the constituent metal carbides), and δ_{χ} (deviation of the Pauling electronegativity). In addition, δ_{VEC} (deviation of valence electron concentrations), VEC (valence electron concentration), and δ_{T_m} were identified as the primary predictors for hardness.⁹² The finding indicates that the hardness increases when $\bar{\chi} < 4.1$ and decreases at higher $\bar{\chi}$ values while the modulus demonstrated an increase across three distinct intervals: $\bar{\chi} < 4.1$, $4.1 \leq \bar{\chi} \leq 4.3$ and $\bar{\chi} > 4.3$ ($\bar{\chi}$, average Pauling electronegativity). In addition, the hardness increases first with δ_{EA} (deviation of electron affinities) and then is apt to decrease. It was proposed that δ_{χ} and $\delta_{r_{\text{atom}}}$ are relatively essential in predicting the Young's modulus of HEAs,¹⁰⁵ but not so effective in predicting the Young's modulus and hardness values of HECs. In addition, as the total energy of the HEC system decreases, there is an observed increase in both the modulus and hardness. This suggests that high-entropy systems characterized by greater stability are more inclined to exhibit improved mechanical properties.

3.2.5 $\delta_{\text{B-TM}}$ criterion. Yan *et al.* identified a systematic approach for the design of single-phase high entropy diborides (HEBs) through the utilization of a data-driven methodology.⁹³ The utilization of machine learning in materials science has been significantly impeded by data-related challenges, including insufficient data and substandard data quality. However, researchers have effectively addressed this issue through the implementation of a high-throughput experimental (HTE) methodology.⁹³ In contrast to prior studies, Yan's research does not rely solely on the existing literature for data collection. Instead, all data utilized in the study are obtained from samples that have been prepared under consistent conditions. This methodological approach notably enhances the quality of the training data essential for the development of dependable machine learning models. Through the utilization of interpretable machine learning techniques, they illustrated that the predominant factor influencing the formation of HEBs is $\delta_{\text{B-TM}}$. According to previous study, the $\delta_{\text{B-TM}}$ means B-TM bond length deviation of the precursor diborides.¹⁰⁶

$$\delta_{\text{B-TM}} = 100 \times \sqrt{\sum_{i=1}^n c_i \left(1 - \frac{l_i}{\bar{l}}\right)^2} \quad (17)$$

where l_i is the length of the B-TM bond in diborides, $\bar{l} = \sum_{i=1}^n c_i l_i$ denotes the mean distance of the B-TM bond, c_i denotes the concentration of the i th diboride precursor, and n is the total number of precursor species in a HEB. Consequently, the researchers proposed an empirical rule that while $\delta_{\text{B-TM}} < 3.66$ tends to form single-phase high-entropy diborides, $\delta_{\text{B-TM}} > 3.66$ is more likely to form multiphase high-entropy diborides (Fig. 12(d)).⁹³

3.2.6 VEC criterion. The high hardness and thermal stability exhibited by high-entropy carbide ceramics have enabled their potential applications in significant fields, yet they have been consistently limited by their inferior fracture toughness. Sangiovanni *et al.*⁹⁴ proposed that the valence electron concentration (VEC) is a crucial parameter in regulating the fracture resistance of high-entropy carbides. The research

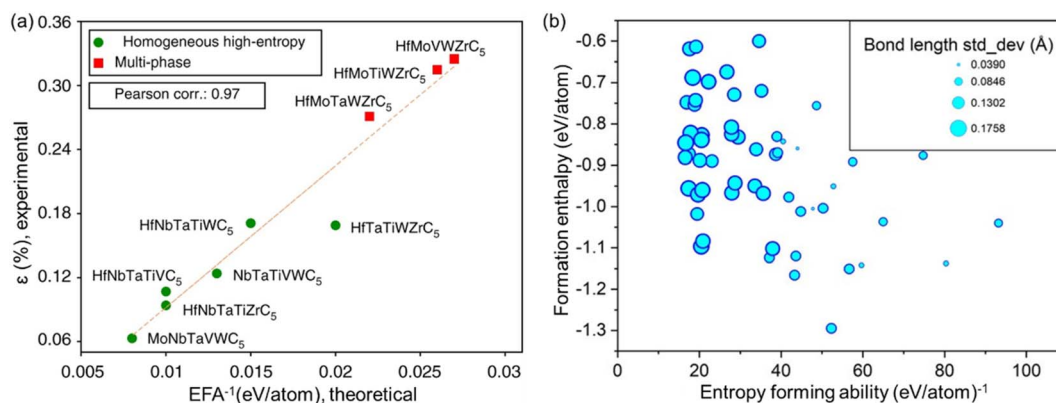


Fig. 13 (a) Linear relationship between EFA-1 and the distortion of experimental lattice parameters ϵ . Green circles and red squares indicate homogeneous high-entropy single- and multi-phase compounds, respectively. Reproduced under the terms of the CC-BY 4.0 license. Copyright 2022, the authors, published by Springer Nature.¹⁰⁹ (b) Formation enthalpy, EFA, and BLSD of all 56 HEN compositions. The radius of the circle shows the BLSD, as shown in the inset. Reproduced from ref. 108 with permission from John Wiley and Sons, copyright 2021.

examined six different compositions of high-entropy ceramics to explore the relationship between the VEC and the material's resistance to brittle fracture. Fig. 12(e) illustrates the tensile properties of six types of high-entropy carbides. It was suggested that high entropy carbides with a VEC equal to or greater than 9.4 demonstrate favorable fracture resistance, while samples with a VEC below 9 appear to be brittle.

3.2.7 EFA criterion. Entropy formation ability (EFA) is often utilized as a descriptor for identifying potential single-phase high-entropy ceramics.^{107–109} EFA is characterized as the inverse of the standard deviation of the energy distribution spectrum encompassing all configurations.¹⁰⁹ The standard deviation σ can be used to quantitatively describe the energy distribution spectrum (H_i). The equation for EFA can be represented by the following formula:

$$\text{EFA}(N) \equiv \{\sigma[\text{spectrum}(\text{Hi}(N))]\}_{T=0}^{-1} \quad (18)$$

$$\sigma\{H_i(N)\} = \sqrt{\frac{\sum_{i=1}^n g_i (H_i - H_{\text{mix}})^2}{\left(\sum_{i=1}^n g_i\right) - 1}} \quad (19)$$

where n is the total number of sampled geometrical configurations and g_i are their degeneracies. Saker *et al.*¹⁰⁹ produced 56 five-metal compositions from eight refractory metals (Hf, Nb, Mo, Ta, Ti, V, W, and Zr). Subsequently, they utilized the automated FLOW partial occupation method to generate 49 distinct 10-atom unit cell configurations for each composition. Based on calculations and experimental findings, it is suggested that the formation of single phase by high-entropy carbides is more likely when the EFA exceeds 50 (Fig. 13(a)). A few years later, Huang *et al.*¹⁰⁸ carried out an in-depth investigation on the focus of high-entropy nitride ceramics building upon prior studies. The standard deviation of bond length (BLSD) is also implemented to describe the relationship between EFA and lattice distortion. EFA, BLSD, and formation enthalpy for the entire set of 56 compositions are depicted in Fig. 13(b). It was suggested that large EFA values and small enthalpy of formation tend to form single-phase high-entropy nitride ceramics.

3.2.8 VEC and mechanical properties. The VEC has been demonstrated to function as a reliable indicator for the mechanical characteristics of nitrides, carbides, and carbonitrides. An increase in the VEC is associated with an increase in metallic bond properties and a greater number of structural

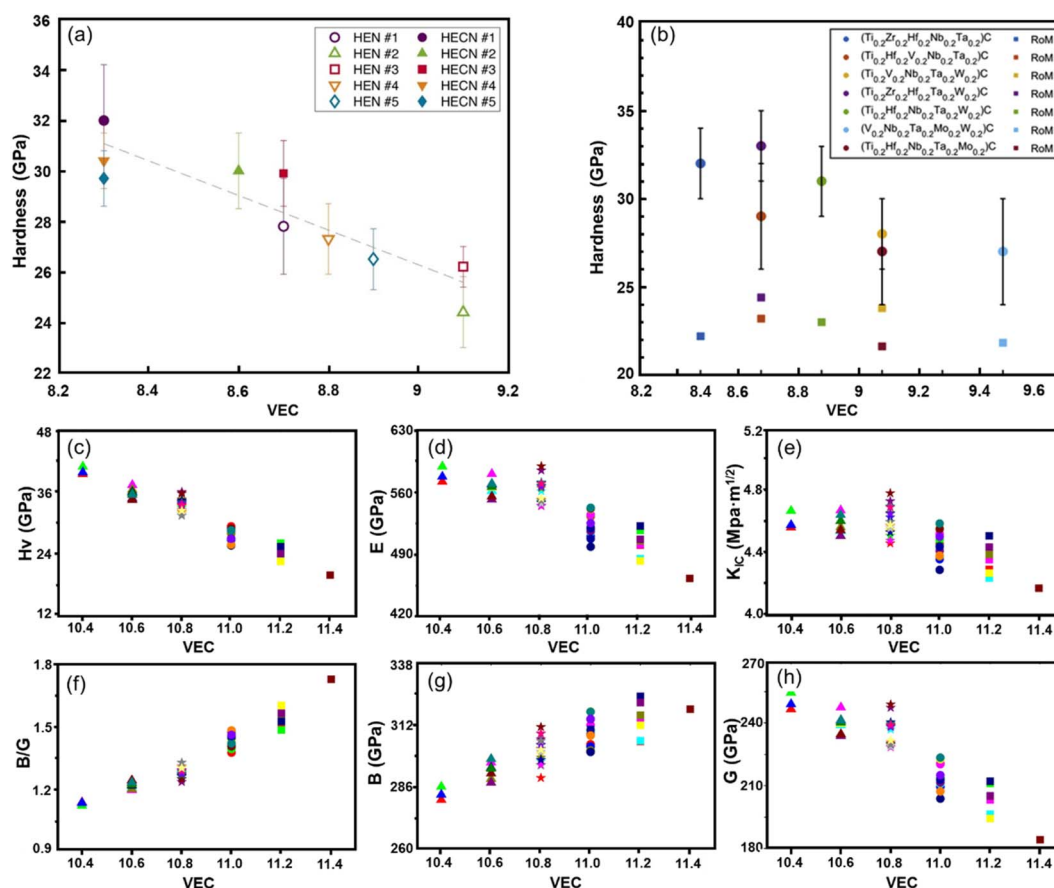


Fig. 14 (a) Nanoindentation hardness as a function of the valence electron concentration (VEC). Error bars are 1 standard deviation from the mean value. Reproduced under the terms of the CC-BY 4.0 license. Copyright 2020, the authors, published by Springer Nature.¹¹⁰ (b) Hardness of seven high entropy carbide compositions along with rule mixture values against the VEC. Reproduced from ref. 107 with permission from Elsevier, copyright 2020. (c–h) The mechanical properties of the quinary high-entropy metal diborides as functions of the VEC. (c) Vickers hardness; (d) Young's modulus; (e) fracture toughness; (f) B/G; (g) bulk modulus; (h) shear modulus. Reproduced from ref. 111 with permission from Elsevier, copyright 2024.

transformations that the lattice can undergo during deformation.^{101,107,110}

Dippo *et al.*¹¹⁰ conducted a series of computations on ten synthesized high-entropy carbides and high-entropy carbonitrides. As illustrated in Fig. 14, the VEC–hardness diagram is depicted. From Fig. 14(a), it can be observed that high entropy ceramics with high VEC values exhibit low hardness. It was suggested that the increment in the VEC enhances the characteristics of metallic bonds and anharmonic lattice vibrations.¹¹² In terms of mechanical properties, it is characterized by a decrease in hardness. Harrington *et al.*¹⁰⁷ calculated the VEC for seven types of high-entropy carbide ceramics and compared their respective hardness values. The hardness exhibits a decreasing trend with an increase in the VEC value (Fig. 14(b)).

Very recently, Liu *et al.*¹¹¹ conducted an extensive study on the mechanical properties of 56 types of quinary high-entropy

diborides through first-principles density functional theory and thermodynamic calculations. Similarly, the Vickers hardness of quinary HEBs also demonstrates a decreasing trend with an increase in VEC values (Fig. 14(c)). Furthermore, Fig. 14(d)–(h) illustrates the correlation between various mechanical properties and VEC. Within the realm of materials science, the bulk modulus (K), shear modulus (G), and Young's modulus (Y) are fundamental mechanical properties that are commonly employed in the design and development of materials characterized by high hardness and resistance to compression.^{113–115} Furthermore, it can be observed from Fig. 14(e) that the fracture toughness of HEBs exhibits a decreasing trend with an increase in the VEC. This indicates that the VEC can serve as a reliable indicator of the mechanical properties of high-entropy ceramics, thereby aiding in the acceleration of the development of high-performance high-entropy ceramics.

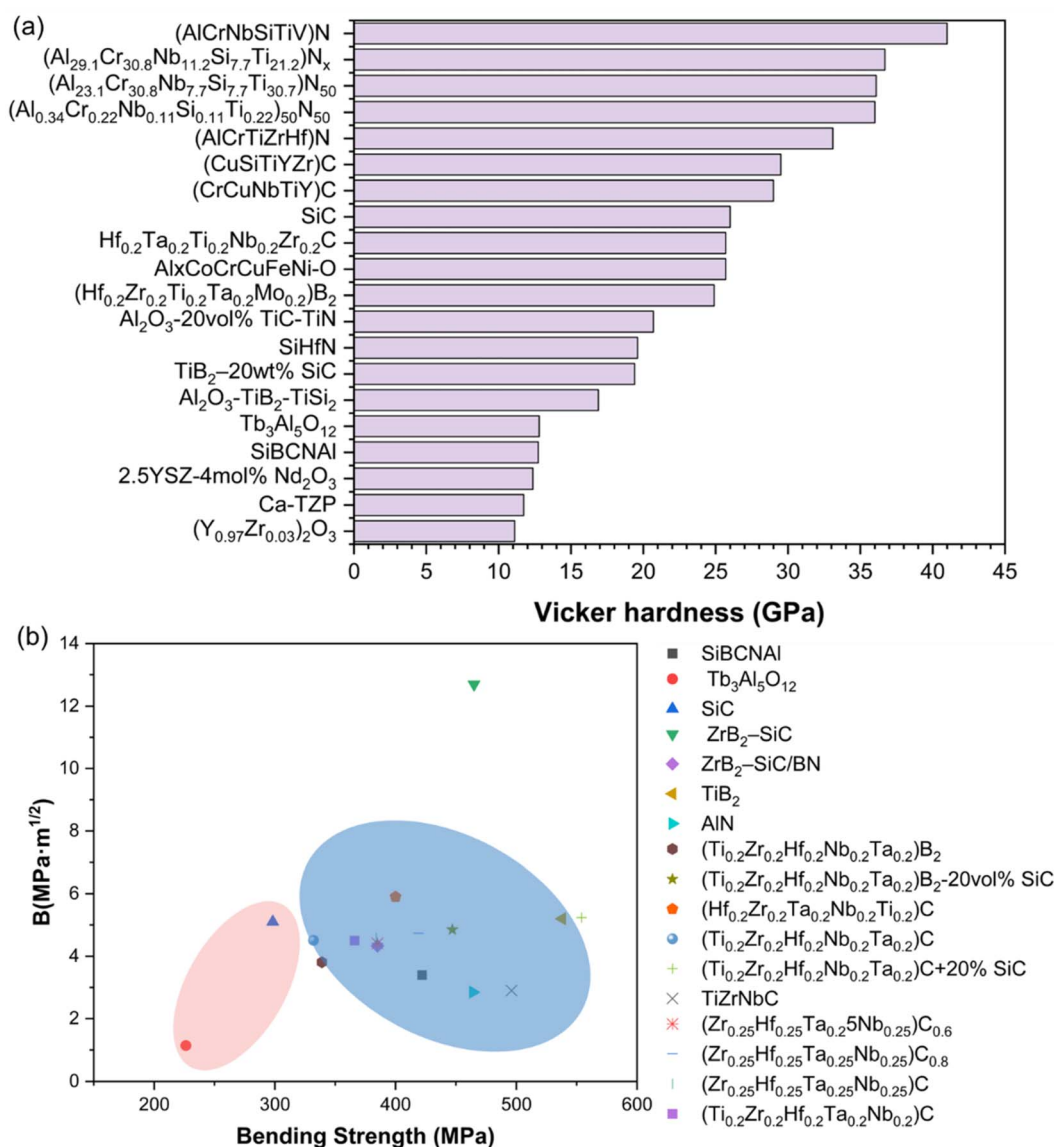


Fig. 15 (a) Comparison chart of Vickers hardness of high-entropy ceramics and traditional ceramics.^{116–133} (b) Mechanical properties of flexural strength–fracture toughness of high-entropy ceramics and traditional ceramics.^{12,17,35,134–136}

3.3 Mechanical properties of high-entropy ceramics

3.3.1 Hardness. Many HECs demonstrate superior hardness compared to conventional ceramics. Fig. 15(a) illustrates the Vickers hardness values of select HECs in comparison to traditional ceramic materials. The exceptional hardness of HECs is intricately linked to their fundamental properties. When multiple alloying elements are mixed in near equimolar ratios to form a single-phase solid solution, the inevitable distortion of the lattice structure in high-entropy materials is attributed to the differences in atomic radii and mismatch in physical properties such as elastic moduli among the various elements. HECs are innovative materials containing a minimum of four distinct cations or anions. Due to variations in the atomic radii of constituent elements, HECs exhibit pronounced lattice distortion effects. Excessive lattice distortion will destabilize the structure of the single-phase solid solution, resulting in the precipitation of the second phase or even amorphization.¹³⁷ Furthermore, the distortion of the lattice structure will lead to an increase in the internal energy of the material, an increase in microscopic stress, and a hindrance to the movement of dislocations. Consequently, this will contribute to the heightened hardness of HECs.

3.3.2 Elevated temperature properties. The advancement and evolution of human civilization have necessitated more rigorous demands for mechanical properties. Certain high-temperature operational conditions urgently require a novel material possessing thermal stability, high temperature resistance, and resistance to oxidation and ablation. The thermal resistance and low thermal conductivity of HECs exactly align with this requirement. For example, the thermal resistance of equiatomic (HfZrTaNbTi)C ceramics was investigated through the process of annealing the specimens at temperatures of 500, 800, and 1140 °C in an argon environment for a duration of 1 hour.¹³⁸ The experimental findings demonstrate the absence of phase decomposition and phase transition, providing evidence for the favorable thermal stability of (HfZrTaNbTi)C at a temperature of 1140 °C. It was suggested that the excellent thermal stability of HECs can be attributed to sluggish diffusivity.^{139–141} A research investigation was conducted to analyze the high temperature oxidation characteristics of a dual phase diboride and a high entropy diboride composed of $(\text{Ti}_{0.25}\text{V}_{0.25}\text{Zr}_{0.25}\text{Hf}_{0.25})\text{B}_2$, both containing identical metallic elements in the sublattice.¹³⁹ At 1500 °C, the oxidation rate of dual phase diboride was found to be 2.8 times higher than that of high entropy diboride. The exceptional effectiveness of high entropy diboride was ascribed to the high entropy and sluggish diffusion of oxygen resulting from lattice distortion, thereby augmenting its resistance to oxidation.¹³⁹ Due to the kinetic hysteresis diffusion effect introduced by HECs, the velocity of heat transfer in HECs becomes slow, which can explain the low thermal conductivity of most HECs. Furthermore, the high-entropy effect of HECs contributes to enhancing their resistance to oxidation. As a result, HECs are anticipated to demonstrate greater potential in high-temperature thermal insulation and anti-oxidation applications compared to traditional ceramic materials.

3.3.3 Strength and toughness. Ceramic materials have historically been constrained by their relatively low fracture toughness. However, the vast compositional range and distinctive microstructure of HECs offer the potential to attain a balance between strength and fracture toughness in these materials. We observed an enhancement in the strength–toughness characteristics of high-entropy ceramics in comparison to conventional ceramic materials (Fig. 15(b)). As a result of the incorporation of additional components into HECs, these materials exhibit noticeable lattice distortion. This lattice distortion contributes to heightened resistance to dislocation motion, consequently resulting in greater strength of HECs when compared to conventional ceramic materials. The solution strengthening effect resulting from the mutual solution between different metal components in HECs has been observed to contribute to their high levels of hardness and fracture toughness.¹⁴² In addition, the addition of various elements in HECs may produce a cocktail effect and improve the strength–fracture toughness of ceramics. It has been proposed that the addition of Mo can promote grain refinement and produce fine grain strengthening. On the other hand, the addition of Mo helps in the ceramic sintering process to densify. These two effects synergistically improve the fracture toughness of (TiZrNbTaMo)C.³⁶

As emerging ceramic materials, HECs undoubtedly break the design shackles of traditional ceramic materials and greatly expand the diversity of ceramic materials. Due to the distinctive composition of HEC materials and their resemblance to high-entropy alloys in terms of the “four major effects”, HEC materials exhibit exceptional corrosion resistance/chemical stability/hardness/wear resistance and thermal stability. Consequently, these materials are anticipated to find extensive applications in national defense, aerospace, nuclear energy, and other sectors. Unlike metallic materials, which typically function as conductors, ceramics possess diverse electrical properties and can serve as conductors, semiconductors, or insulators, thereby expanding the potential use of HECs in electronic appliances. Tables 2–5 show the mechanical characteristics of high-entropy oxide ceramics, high-entropy nitride ceramics, high-entropy carbide ceramics and high-entropy boride ceramics, respectively.

3.4 Strengthening/toughening of HECs

3.4.1 Fine grain strengthening/toughening. In polycrystalline materials, the size of the grains significantly impacts the mechanical properties. This is attributed to the abundance of grain boundaries in materials with small grain sizes, which impede the motion of dislocations. Additionally, the diverse orientations of the grains also contribute to this influence.²⁰⁹ Therefore, grain refinement may have a certain degree of improvement effect on fracture toughness. Fig. 16 illustrates the fracture toughness of high entropy ceramics with different grain sizes, showing an increasing trend in fracture toughness as the grain size decreases.

Ma *et al.*²¹³ successfully prepared ultra-fine-grained $(\text{Hf}_{0.2}\text{Zr}_{0.2}\text{Ta}_{0.2}\text{Nb}_{0.2}\text{Ti}_{0.2})\text{B}_2$ high-entropy diboride ceramics.

Table 2 Reported mechanical properties of high-entropy oxides

High entropy oxides	Condition	Crystal structure	Hardness (GPa)	Thermal conductivity (Wm ⁻¹ K ⁻¹)	Fracture toughness (MPa m ^{1/2})	Ref.
(Al _{0.19} Cr _{0.13} Nb _{0.19} Ta _{0.30} Ti _{0.19})O ₂	RMS: <i>f</i> _{O₂} (30%)	Rutile	22	—	—	143
	RMS: <i>f</i> _{O₂} (80%)	Rutile	24	—	—	
(AlCrTaTiZr)O _x	RMS: <i>f</i> _{O₂} (2.5%)	Amorphous	13	—	—	144
Al _x CoCrCuFeNi-O	RMS-AN (500°C/5 h)	Spinel	25.7 ± 2.3	—	—	117
(Al _{0.31} Cr _{0.20} Fe _{0.14} Ni _{0.35})O	RMS	—	18.5	—	—	145
BaCo _{0.2} Fe _{0.2} Zr _{0.2} Sn _{0.2} Pr _{0.2} O _{3-δ}	—	Perovskite	—	—	—	146
(Ce _{0.2} Y _{0.2} Gd _{0.2} Sm _{0.2} Nd _{0.2}) ₂ Zr ₂ O ₇	PLS	—	—	0.056	—	147
(Dy _{0.2} Y _{0.2} Ho _{0.2} Er _{0.2} Yb _{0.2}) ₂ Zr ₂ O ₇	—	—	~12	—	—	148
(Gd _{0.2} Y _{0.2} Er _{0.2} Tm _{0.2} Yb _{0.2}) ₂ Zr ₂ O ₇	—	—	11.98	—	1.535	149
(La _{0.2} Nd _{0.2} Y _{0.2} Er _{0.2} Yb _{0.2}) ₂ Zr ₂ O ₇	—	—	11.47	—	—	148
(La _{0.2} Nd _{0.2} Sm _{0.2} Eu _{0.2} Gd _{0.2}) ₂ Zr ₂ O ₇	—	Pyrochlore	10.75	—	—	148
(La _{0.2} Nd _{0.2} Sm _{0.2} Eu _{0.2} Gd _{0.2}) ₂ Zr ₂ O ₇	RFS	Pyrochlore	~12	—	—	150
(La _{0.2} Nd _{0.2} Sm _{0.2} Eu _{0.2} Gd _{0.2}) ₂ Zr ₂ O ₇	RFS	Pyrochlore	8.2	—	—	150
(La _{0.2} Y _{0.2} Gd _{0.2} Sm _{0.2} Nd _{0.2}) ₂ Zr ₂ O ₇	PLS	—	—	0.044	—	147
(La _{0.2} Y _{0.2} Gd _{0.2} Ce _{0.2} Sm _{0.2}) ₂ Zr ₂ O ₇	PLS	—	—	0.047	—	147
(La _{0.2} Ce _{0.2} Gd _{0.2} Sm _{0.2} Nd _{0.2}) ₂ Zr ₂ O ₇	PLS	—	—	0.052	—	147
(La _{0.2} Y _{0.2} Gd _{0.2} Ce _{0.2} Nd _{0.2}) ₂ Zr ₂ O ₇	PLS	—	—	0.051	—	147
(La _{0.2} Y _{0.2} Ce _{0.2} Sm _{0.2} Nd _{0.2}) ₂ Zr ₂ O ₇	PLS	—	—	0.057	—	147
(La _{1/7} Nd _{1/7} Sm _{1/7} Eu _{1/7} Gd _{1/7} Dy _{1/7} Ho _{1/7}) ₂ Zr ₂ O ₇	SPS	Pyrochlore	13.86	—	1.1	151
(La _{0.2} Y _{0.2} Sm _{0.2} Eu _{0.2} Gd _{0.2}) ₂ Zr ₂ O ₇	CIP-PLS	Pyrochlore	7.9	—	—	152
((La _{1/3} Eu _{1/3} Gd _{1/3}) _{1-x} Yb _x) ₂ Zr ₂ O ₇	—	—	~11	—	—	153
(La _{0.25} Eu _{0.25} Gd _{0.25} Yb _{0.25}) ₂ (Zr _{0.75} Hf _{0.25}) ₂ O ₇	—	—	~10	—	—	154
(La _{0.2} Nd _{0.2} Sm _{0.2} Gd _{0.2} Yb _{0.2}) ₂ (Zr _{0.75} Ce _{0.25}) ₂ O ₇	—	Pyrochlore	—	—	2.0 ± 0.3	155
(Sm _{1/5} Yb _{1/5} Gd _{1/5} Er _{1/5} Dy _{1/5}) ₂ Ti ₂ O ₇	—	Pyrochlore	10.14	—	—	156
Sr(Y _{0.2} Sm _{0.2} Gd _{0.2} Dy _{0.2} Yb _{0.2}) ₂ O ₄	SSR	—	6.86	—	1.92 ± 0.04	157
(Zr _{0.2} Hf _{0.2} Ti _{0.2} Gd _{0.2} Y _{0.2})O _{2-δ}	—	—	—	0.0257	—	158
(Ce _{0.2} Zr _{0.2} Hf _{0.2} Sn _{0.2} Ti _{0.2})O ₂	SSR	Fluorite	—	1.28	—	159
(Dy _{0.2} Ho _{0.2} Er _{0.2} Y _{0.2} Yb _{0.2}) ₃ NbO ₇	—	Fluorite	9.51	0.724	—	160
(Hf _{0.25} Zr _{0.25} Ce _{0.25} Y _{0.25})O _{2-δ}	SPS	Fluorite	13.6 ± 0.5	1.74 ± 0.15	—	161
(Hf _{0.25} Zr _{0.25} Ce _{0.25} Y _{0.25}) ₂ (Y _{0.125} Yb _{0.125})O _{2-δ}	SPS	Fluorite	12.7 ± 0.7	1.55 ± 0.20	—	161
(Hf _{0.2} Zr _{0.2} Ce _{0.2} Y _{0.2}) ₂ O _{2-δ}	SPS	Fluorite	13.3 ± 0.6	1.29 ± 0.11	—	161
(Hf _{0.25} Zr _{0.25} Ce _{0.25} Y _{0.25} Ca _{0.125})O _{2-δ}	SPS	Fluorite	13.3 ± 0.6	1.10 ± 0.20	—	161
(Hf _{0.25} Zr _{0.25} Ce _{0.25} Y _{0.25} Gd _{0.125})O _{2-δ}	SPS	Fluorite	13.2 ± 0.5	1.17 ± 0.13	—	161
(Hf _{0.2} Zr _{0.2} Ce _{0.2} Y _{0.2} Gd _{0.2})O _{2-δ}	SPS	Fluorite	13.1 ± 0.5	1.61 ± 0.13	—	161
(Hf _{0.2} Zr _{0.2} Ce _{0.2} Y _{0.2} Gd _{0.2})O _{2-δ}	SPS	Fluorite	12.6 ± 0.5	1.62 ± 0.13	—	161
(Hf _{0.25} Zr _{0.25} Ce _{0.25} Y _{0.25} Gd _{0.125})O _{2-δ}	SPS	Fluorite	12.3 ± 0.7	1.81 ± 0.14	—	161
(Y _{0.3} Gd _{0.3} Yb _{0.4}) ₄ Hf ₃ O ₁₂	UHS	Fluorite	11.94	—	1.26	162
(Ca _{0.5} Sr _{0.5})(RE) ₂ O ₄	SSR	Anti-spinel	—	1.48	—	163
(Dy _{0.2} Ho _{0.2} Er _{0.2} Tm _{0.2} Lu _{0.2}) ₂ Hf ₂ O ₇	—	Fluorite	15.55	—	1.69	164
La ₂ (Hf _{1/2} Zr _{1/2}) ₂ O ₇	—	Pyrochlore	—	2.29 ± 0.06	—	125
(La _{1/2} Pr _{1/2}) ₂ (Sn _{1/3} Hf _{1/3} Zr _{1/3}) ₂ O	—	Pyrochlore	—	2.24 ± 0.07	—	125
(La _{1/3} Pr _{1/3} Nd _{1/3}) ₂ (Hf _{1/2} Zr _{1/2}) ₂ O ₇	—	Pyrochlore	—	2.16 ± 0.06	—	125
(La _{1/5} Ce _{1/5} Nd _{1/5} Sm _{1/5} Eu _{1/5}) ₂ Zr ₂ O ₇	—	Pyrochlore	—	2.06 ± 0.06	—	125
(La _{1/7} Ce _{1/7} Pr _{1/7} Nd _{1/7} Sm _{1/7} Eu _{1/7} Gd _{1/7}) ₂	—	Pyrochlore	—	1.97 ± 0.06	—	125
(Hf _{1/2} Zr _{1/2}) ₂ O ₇	—	—	—	—	—	
(La _{1/7} Ce _{1/7} Pr _{1/7} Nd _{1/7} Sm _{1/7} Eu _{1/7} Gd _{1/7}) ₂	—	Pyrochlore	—	2.02 ± 0.06	—	125
(Sn _{1/3} Hf _{1/3} Zr _{1/3}) ₂ O	—	—	—	—	—	
(La _{0.2} Nd _{0.2} Sm _{0.2} Eu _{0.2} Gd _{0.2}) ₂ Zr ₂ O ₇	SSR	Pyrochlore	—	<1	—	165
(La _{0.2} Y _{0.2} Sm _{0.2} Eu _{0.2} Gd _{0.2}) ₂ Zr ₂ O ₇	SSR	Pyrochlore	—	<1	—	165
(La _{0.2} Nd _{0.2} Y _{0.2} Eu _{0.2} Gd _{0.2}) ₂ Zr ₂ O ₇	SSR	Pyrochlore	—	<1	—	165
(La _{0.2} Nd _{0.2} Sm _{0.2} Y _{0.2} Gd _{0.2}) ₂ Zr ₂ O ₇	SSR	Pyrochlore	—	<1	—	165
(La _{0.2} Nd _{0.2} Sm _{0.2} Eu _{0.2} Y _{0.2}) ₂ Zr ₂ O ₇	SSR	Pyrochlore	—	<1	—	165
(La _{0.2} Ce _{0.2} Nd _{0.2} Sm _{0.2} Eu _{0.2}) ₂ Zr ₂ O ₇	—	Pyrochlore	—	0.76	—	166
(Sm _{0.2} Eu _{0.2} Tb _{0.2} Dy _{0.2} Lu _{0.2}) ₂ Zr ₂ O ₇	SSR	Pyrochlore	12.42	0.86	~2.24	167
(Mg _x Co _x Ni _x Cu _x Zn _x)O	—	Rock-salt	—	—	—	168
Mg _x Ni _x Co _x Cu _x Zn _x Sc _x O (<i>x</i> ~ 0.167)	—	Rock-salt	—	—	—	169
Mg _x Ni _x Cu _x Co _x Zn _x Ge _x O, <i>x</i> = 0.167	—	Rock-salt	—	1.60 ± 0.14	—	170
Mg _x Ni _x Cu _x Co _x Zn _x Cr _x O, <i>x</i> = 0.167	—	Rock-salt	—	1.64 ± 0.24	—	170
Mg _x Ni _x Cu _x Co _x Zn _x Sn _x O, <i>x</i> = 0.167	—	Rock-salt	—	1.44 ± 0.10	—	170
Mg _x Ni _x Cu _x Co _x Zn _x Sb _x O, <i>x</i> = 0.167	—	Rock-salt	—	1.41 ± 0.17	—	170
Mg _x Ni _x Cu _x Co _x Zn _x Sc _x O, <i>x</i> = 0.167	—	Rock-salt	—	1.68 ± 0.13	—	170

Table 2 (Contd.)

High entropy oxides	Condition	Crystal structure	Hardness (GPa)	Thermal conductivity (Wm ⁻¹ K ⁻¹)	Fracture toughness (MPa m ^{1/2})	Ref.
Mg _x Ni _x Cu _x Co _x Zn _x O, x = 0.2	—	Rock-salt	—	2.95 ± 0.25	—	170
Sm ₂ (Sn _{1/4} Ti _{1/4} Hf _{1/4} Zr _{1/4}) ₂ O ₇	—	Pyrochlore	—	1.73 ± 0.05	—	125
(Sm _{1/2} Gd _{1/2}) ₂ (Ti _{1/3} Hf _{1/3} Zr _{1/3}) ₂ O ₇	—	Pyrochlore	—	1.47 ± 0.04	—	125
(Sm _{1/3} Eu _{1/3} Gd _{1/3}) ₂ (Hf _{1/2} Zr _{1/2}) ₂ O ₇	—	Pyrochlore	—	1.97 ± 0.06	—	125
(Sm _{1/3} Eu _{1/3} Gd _{1/3}) ₂ (Sn _{1/3} Hf _{1/3} Zr _{1/3}) ₂ O ₇	—	Pyrochlore	—	2.21 ± 0.07	—	125
(Sm _{1/3} Eu _{1/3} Gd _{1/3}) ₂ (Ti _{1/4} Sn _{1/4} Hf _{1/4} Zr _{1/4}) ₂ O ₇	—	Pyrochlore	—	1.67 ± 0.05	—	125
(Sm _{1/4} Eu _{1/4} Gd _{1/4} Yb _{1/4}) ₂ (Ti _{1/4} Sn _{1/4} Hf _{1/4} Zr _{1/4}) ₂ O ₇	—	Pyrochlore	—	1.45 ± 0.04	—	125
(Sm _{1/3} Eu _{1/3} Gd _{1/3}) ₂ (Ti _{1/2} Sn _{1/6} Hf _{1/6} Zr _{1/6}) ₂ O ₇	—	Pyrochlore	—	1.71 ± 0.05	—	125
(Sm _{1/3} Eu _{1/3} Gd _{1/3}) ₂ (Ti _{3/4} Sn _{1/12} Hf _{1/12} Zr _{1/12}) ₂ O ₇	—	Pyrochlore	—	1.90 ± 0.06	—	125
(Sm _{1/3} Eu _{1/3} Gd _{1/3}) ₂ Ti ₂ O ₇	—	Pyrochlore	—	2.88 ± 0.09	—	125
(Sm _{1/4} Eu _{1/4} Gd _{1/4} Yb _{1/4}) ₂ (Ti _{1/2} Hf _{1/4} Zr _{1/4}) ₂ O ₇	—	Pyrochlore	—	1.36 ± 0.04	—	125
(Sm _{3/4} Yb _{1/4}) ₂ (Ti _{1/2} Zr _{1/2}) ₂ O ₇	—	Pyrochlore	—	1.40 ± 0.04	—	125
(Y _{0.2} Nd _{0.2} Sm _{0.2} Eu _{0.2} Gd _{0.2}) ₂ Zr ₂ O ₇	SSR	Pyrochlore	—	<1	—	165

Specifically, at a temperature of 1973 K, the sintered sample with an average grain size of 684 nm exhibited high Vickers hardness (26.2 GPa) and excellent fracture toughness (5.3 MPa m^{1/2}). It was proposed that the comprehensive mechanical properties exhibited by (Hf_{0.2}Zr_{0.2}Ta_{0.2}Nb_{0.2}Ti_{0.2})B₂ are mainly

attributed to the fine-grain strengthening mechanism and the microcrack deflection toughening mechanism. As depicted in Fig. 17(a)–(d), the fracture model of the sintered sample is distinguished by typical intergranular fracture, with numerous regularly faceted and intact ultrafine grains that are visible on

Table 3 Reported mechanical properties of high-entropy nitrides

High-entropy nitrides	Condition	Structure	Hardness (GPa)	Elastic modulus (GPa)	Fracture toughness (MPa m ^{1/2})	Ref.
(Al _{29.1} Cr _{30.8} Nb _{11.2} Si _{7.7} Ti _{21.2})N _x	RMS	FCC (NaCl-type)	36.7	—	—	124
(Al _{23.1} Cr _{30.8} Nb _{7.7} Si _{7.7} Ti _{30.7})N ₅₀	RMS	FCC (NaCl-type)	36.1	—	—	124
(AlCrNbSiTiV)N	RMS	FCC (NaCl-type)	41	30	—	123
(AlCrTiZrHf)N	RMS	FCC	33.1	—	—	122
(Al _{0.34} Cr _{0.22} Nb _{0.11} Si _{0.11} Ti _{0.22}) ₅₀ N ₅₀	RMS	FCC (NaCl-type)	36 (5 mN)	—	—	121
(Al _{0.5} CrFeNiTi _{0.25})N _x	RMS	FCC	21.78	253.8	—	171
(AlMoNbSiTaTiVZr)N _x	—	FCC (NaCl-type)	37	—	—	172
(AlCrMoTiNi) _{1-x} N _x (x = 0.29)	—	Amorphous	15.69 ± 0.27	—	2.0	173
(AlCrMoTiNi) _{1-x} N _x (x = 0.37)	—	FCC	18.50 ± 0.22	—	—	173
(AlCrMoTiNi) _{1-x} N _x (x = 0.40)	—	FCC	28.91 ± 1.02	—	—	173
(AlCrMoTiNi) _{1-x} N _x (x = 0.45)	—	FCC	31.25 ± 1.01	—	3.25	173
(AlCrNbSiTiV)N	RMS	FCC	—	—	—	174
(Al,Ta,Ti,V,Zr)N	RMS	—	~20	433	2.4	14
(AlCrNbSiTiV)N	RMS	FCC (NaCl-type)	>40	—	—	175
(AlCrSiNbZr)N _x	RMS	—	12.3	—	—	176
(AlCrSiTiZr) _{100-x} N _x	RMS	Amorphous	16.9	231.5	—	177
(AlCrTiZrHf)N	RMS	FCC	33.1	—	—	178
Al–Cr–Nb–Y–Zr–N	RMS	—	29.6 ± 1.2	343	—	179
(Al,Cr,Nb,Y,Zr)N _x	RMS	FCC (NaCl-type)	27	230–370	—	180
AlCoCrCu _{0.5} FeNi–N	RMS–F _{N₂} /25%	—	9.8	—	—	181
(CrHfTaTiZr) ₁ N _x	—	FCC (NaCl-type)	26.5	465.5	—	110
(CrHfNbTiZr) ₁ N _x	—	FCC (NaCl-type)	27.3	488.4	—	110
(CrHfNbTaTi) ₁ N _x	—	FCC (NaCl-type)	26.2	488.9	—	110
(CrNbTaTiV) ₁ N _x	—	FCC (NaCl-type)	24.4	476.7	—	110
(FeCoNiCuAlCrV)N	—	FCC (NaCl-type)	38	—	—	182
(Hf,Ta,Ti,V,Zr)N	RMS	FCC	32.5 ± 0.8	—	—	183
Hf–Nb–Ti–V–Zr–N	RMS	FCC (NaCl-type)	18.8	418	—	184
(Hf _{0.2} Nb _{0.2} Ta _{0.2} Ti _{0.2} Zr _{0.2})N	SPS	FCC	Up to 33 (4.9 N)	—	Up to 5.2	18
(MoSiTiVZr)N _x	RMS	—	45.6	—	—	185
(HfNbTaTiZr) ₁ N _x	—	FCC (NaCl-type)	27.8	502.6	—	110
(TiZrNbHfTa)N/WN	VAC	FCC	34	325	—	186
(TiVCrZrNbMoHfTaWAlSi)N	RMS	FCC + HCP	34.8	—	—	187
(VAlTiCrMo)N _x	RMS	FCC	5.731	133.697	—	188
(Zr–Ti–Cr–Nb–Si)N	VAD	FCC	27	273	—	189

Table 4 Reported mechanical properties of high-entropy carbides

High-entropy carbide	Condition	Structure	Hardness (GPa)	Elastic modulus (GPa)	Fracture toughness (MPa ^{1/2})	Ref.
(CuSiTiY)C	—	Amorphous	29.5	—	—	120
(CrCuNbTiY)C	—	FCC	29	—	—	119
Hf _{0.2} Ta _{0.2} Ti _{0.2} Nb _{0.2} Zr _{0.2} C	—	FCC	25.7 ± 3.5	473 ± 37	—	118
Hf _{0.2} Ta _{0.2} Ti _{0.2} Nb _{0.2} Mo _{0.2} C	—	—	23.8 ± 2.7	—	—	118
Hf _{0.2} Ta _{0.2} Ti _{0.2} Nb _{0.2} Mo _{0.2} C	—	FCC	23.8 ± 2.7	544 ± 48	—	118
(Hf _{0.2} Zr _{0.2} Ta _{0.2} Nb _{0.2} Ti _{0.2})C	SPS	Rock-salt	17.07 ± 0.54 (9.8 N)	—	5.9 ± 0.7	16
(Hf _{0.2} Zr _{0.2} Ta _{0.2} Nb _{0.2} Ti _{0.2})C	PLS	—	17.7 ± 0.5 (9.8 N)	—	4.3 ± 0.2	190
(TiZrHfNbTaMo)C	PLS	—	23.2 (9.8 N)	—	3.7 ± 0.2	191
(Hf,Zr,Ti,Ta,Nb)C	CTR	Rock-salt	24.8 ± 0.8 (4.9 N)	452 ± 6	—	192
(Hf _{0.2} Ta _{0.2} Zr _{0.2} Nb _{0.2} Ti _{0.2})C	HP	—	24	—	2.306	193
(Hf-Ta-Zr-Nb)C	SPS	Rock-salt	36.1 ± 1.6	598 ± 15	—	194
(NbTaZrTiHfVW)C	—	—	38.71	—	4.67	195
(Ti _{0.2} Zr _{0.2} Hf _{0.2} Nb _{0.2} Ta _{0.2})C + 20%SiC	SPS	FCC	25 ± 0.8 (9.8 N)	—	5.24 ± 0.41	17
(Ti _{0.2} Zr _{0.2} Hf _{0.2} Nb _{0.2} Ta _{0.2})C	SPS	—	21.9 ± 0.4 (9.8 N)	—	4.51 ± 0.61	17
(TiZrNbTaMo)C	HP	—	25.3 (9.8 N)	—	3.28	36
(Ti _{0.2} Zr _{0.2} Hf _{0.2} Ta _{0.2} Nb _{0.2})C	SPS	—	20.39 (9.8 N)	—	4.5 ± 0.6	196
TiZrHfVNBaB ₁₂ -C	HP	—	12 (9.8 N)	—	4.3 ± 0.6	197
(TiZrHfVNBa)C	—	—	24.9 (9.8 N)	—	—	198
(TiAlCrNbY)C	D _R -0.19	—	15.3 ± 1.2 (0.05 N)	—	—	199
	D _R -0.17	—	20.7 ± 1.4 (0.05 N)	—	—	199
	D _R -0.16	—	22.6 ± 1.2 (0.05 N)	—	—	199
	D _R -0.15	—	12.8 ± 0.9 (0.05 N)	—	—	199
(VNBaMoW)C ₅	SPS	—	19.6	—	5.4	200
(VNBaMoW)C	SPS	Rock-salt	23.8	—	3.34	201
(Zr _{0.25} Nb _{0.25} Ti _{0.25} V _{0.25})C	—	Rock-salt	30.3 ± 0.7	460.4 ± 19.2	4.7 ± 0.5	142
(Zr _{0.25} Hf _{0.25} Ta _{0.25} Nb _{0.25})C	SPS	—	—	—	4.73	134

the fracture surface. The presence of ultra-fine grains not only elevates the hardness, but also leads to increased deformation during crack propagation, consequently improving fracture toughness.

(Hf_{0.2}Mo_{0.2}Ta_{0.2}Nb_{0.2}Ti_{0.2})B₂, with an average grain size of 1.86 μm, exhibits reasonable fracture toughness (4.47 MPa m^{1/2}).¹³ The findings indicate that the increased fracture toughness of (Hf_{0.2}Mo_{0.2}Ta_{0.2}Nb_{0.2}Ti_{0.2})B₂ is attributed to the refinement of the grain structure and improved sintering ability. (Ti_{0.6}W_{0.1}Nb_{0.1}-Ta_{0.1}Mo_{0.1})(C_{0.78}N_{0.22})-Co-Ni (HECN1-Co-Ni) ceramic exhibits excellent hardness (2053.4 HV) and fracture toughness (12.3 MPa m^{1/2}).²¹⁴ It has been suggested that fine-grained strengthening can greatly improve the strength and toughness of HECN1-Co-Ni. Specifically, the crack deflection path caused by fine-grained intergranular fracture is longer, which leads to the improvement of toughness (Fig. 17(e)-(g)). Zhou *et al.*²¹⁵ fabricated (Ti,Nb,Ta,Mo,W)(C,N) (CA2.5-1450) ceramics with fine grain structures, which exhibited high hardness (24.5 GPa) and fracture toughness (6.1 MPa m^{1/2}). Similarly, as the cracks propagate through intergranular fracture, a more pronounced deviation of cracks is observed in fine-grained samples. The increased crack deflection consumes more energy during the crack propagation process, thereby significantly enhancing the fracture toughness of the ceramic (Fig. 17(i)).

3.4.2 Second phase strengthening/toughening. Second phase strengthening is an effective means to strengthen the ceramic. It was proposed that the second phase can manifest in diverse manners, including fibers, precipitates, newly generated phases (occurring at elevated processing temperatures), and

even individual elements.²⁰⁹ Second-phase strengthening, as an effective method for improving traditional ceramic materials, currently holds great potential for enhancing the mechanical properties of HECs. As depicted in Fig. 18, the materials are commonly utilized as a secondary phase for strengthening and toughening.

The (Ti_{0.2}Zr_{0.2}Hf_{0.2}Nb_{0.2}Ta_{0.2})C-20 vol% SiC (HEC-20SiC) sample exhibited excellent four-point bending strength (554 ± 73 MPa) and excellent fracture toughness (5.24 ± 0.41 MPa m^{1/2}) compared to the (Ti_{0.2}Zr_{0.2}Hf_{0.2}Nb_{0.2}Ta_{0.2})C sample.¹⁷ As the sintering temperature increases from 1800 °C to 2000 °C, the mean grain size of the HEC increases from 5 μm to 35 μm, while the mean grain size of HEC-20SiC merely increases from 3 μm to 5 μm (Fig. 19(a)). It was suggested that the addition of SiC particles greatly refines the grain size of the HEC, which in turn improves the bending strength and fracture toughness. Fig. 19(b) and (c) depict the Vickers indentation of the HEC-1900 and HEC-20SiC-1900 samples, aimed at examining the crack propagation characteristics in both specimens. As shown in Fig. 19(b), the crack propagation of the HEC is relatively flat, while the HEC with the addition of SiC particles shows a very tortuous crack propagation path (Fig. 19(c)). Therefore, it can be reasonably deduced that the crack deflection of SiC particles should be the main reason for the improvement of fracture toughness.

Peng *et al.*²¹⁶ also used SiC particles to improve the comprehensive mechanical properties of HECs. They used spark plasma sintering to prepare a series of (NbTaZrW)C-xSiC (x = 0/5/15/30/50 vol%) HECs and explored the toughening

Table 5 Reported mechanical properties of high-entropy borides^a

High-entropy boride	Condition	Structure	Hardness (GPa)	Elastic modulus (GPa)	Fracture toughness (MPa ^{1/2})	Ref.
(Hf _{0.2} Zr _{0.2} Ta _{0.2} Nb _{0.2} Ti _{0.2})B ₂	SPS	Hexagonal	17.5 ± 1.2 (1.96 N)	—	—	46
(Hf _{0.2} Zr _{0.2} Ta _{0.2} Mo _{0.2} Ti _{0.2})B ₂	SPS	Hexagonal	19.1 ± 1.8 (1.96 N)	—	—	46
(Hf _{0.2} Zr _{0.2} Mo _{0.2} Nb _{0.2} Ti _{0.2})B ₂	SPS	Hexagonal	21.9 ± 1.7 (1.96 N)	—	—	46
(Hf _{0.2} Mo _{0.2} Ta _{0.2} Nb _{0.2} Ti _{0.2})B ₂	SPS	Hexagonal	22.5 ± 1.7 (1.96 N)	—	—	46
(Hf _{0.2} Zr _{0.2} Ta _{0.2} Cr _{0.2} Ti _{0.2})B ₂	SPS	Hexagonal	21.0 ± 2.8 (1.96 N)	—	—	46
(Hf _{0.2} Mo _{0.2} Ta _{0.2} Nb _{0.2} Ti _{0.2})B ₂	SPS	Hexagonal	22.5 ± 1.7 (1.96 N)	—	—	202
(Hf _{0.2} Zr _{0.2} Ti _{0.2} Ta _{0.2} Mo _{0.2})B ₂	BCR	Hexagonal	24.9 ± 1.0 (1.96 N)	—	—	116
(Hf _{0.2} Zr _{0.2} Ti _{0.2} Ta _{0.2} Nb _{0.2})B ₂	BCR	Hexagonal	20.5 ± 1.0 (1.96 N)	—	—	116
(Hf _{0.2} Zr _{0.2} Ti _{0.2} Ta _{0.2} Cr _{0.2})B ₂	BCR	Hexagonal	24.9 ± 1.0 (1.96 N)	—	—	116
(Hf _{0.2} Zr _{0.2} Ta _{0.2} Nb _{0.2} Ti _{0.2})B ₂	SPS	Hexagonal	21.7 ± 1.1 (1.96 N)	—	4.06 ± 0.35	13
(Hf _{0.2} Zr _{0.2} Mo _{0.2} Nb _{0.2} Ti _{0.2})B ₂	SPS	Hexagonal	26.3 ± 1.8 (1.96 N)	—	3.64 ± 0.36	13
(Hf _{0.2} Mo _{0.2} Ta _{0.2} Nb _{0.2} Ti _{0.2})B ₂	SPS	Hexagonal	27.0 ± 0.4 (1.96 N)	—	4.47 ± 0.40	13
(Hf _{0.2} Zr _{0.2} Ta _{0.2} Cr _{0.2} Ti _{0.2})B ₂	SPS	Hexagonal	28.3 ± 1.6 (1.96 N)	—	—	203
(Hf _{0.2} Mo _{0.2} Zr _{0.2} Nb _{0.2} Ti _{0.2})B ₂	SPS	Hexagonal	26.3 ± 0.7 (1.96 N)	—	—	203
(Hf _{0.2} Zr _{0.2} Ta _{0.2} Cr _{0.2} Ti _{0.2})B ₂	SPS	Hexagonal	29.3 (1.96 N)	—	3.56	204
(Hf _{0.2} Zr _{0.2} Ti _{0.2} Ta _{0.2} Cr _{0.2})B ₂	AC	—	22.6 (1.96 N)	—	—	205
(Mo _{0.2} Zr _{0.2} Ta _{0.2} Nb _{0.2} Ti _{0.2})B ₂	SPS	Hexagonal	23.7 ± 1.7 (1.96 N)	—	—	46
(Ti _{0.2} Hf _{0.2} Zr _{0.2} Nb _{0.2} Ta _{0.2})B ₂	BCR	Hexagonal	25.6 ± 0.8	500	2.83 ± 0.15	10
(Ti _{0.2} Zr _{0.2} Hf _{0.2} Mo _{0.2} W _{0.2})B ₂	BCR	Hexagonal	26.0 ± 1.5 (1.96 N)	—	—	206
(Ti _{0.2} Ta _{0.2} Cr _{0.2} Mo _{0.2} W _{0.2})B ₂	BCR	Hexagonal	23.7 ± 1.3 (1.96 N)	—	—	206
(Ti _{0.2} Zr _{0.2} Hf _{0.2} Nb _{0.2} Ta _{0.2})B ₂	BCR	Hexagonal	20.9 ± 1.3 (1.96 N)	505	3	206
(Ti _{0.2} Zr _{0.2} Hf _{0.2} Nb _{0.2} Ta _{0.2})B ₂	HP	—	23.7 ± 0.7 (1.96 N)	—	3.81 ± 0.40	12
(Ti _{0.2} Zr _{0.2} Hf _{0.2} Nb _{0.2} Ta _{0.2})B ₂ -20 vol% SiC	HP	—	24.8 ± 1.2 (1.96 N)	—	4.85 ± 0.33	12
(Y _{0.2} Nd _{0.2} Sm _{0.2} Gd _{0.2} Tb _{0.2})B ₄	SPS	Tetragonal	13–15 (9.8 N)	—	—	207
(Zr _{0.2} Hf _{0.2} Nb _{0.2} Ta _{0.2} W _{0.2})B ₂	BCR	Hexagonal	26.7 ± 1.1 (1.96 N)	—	—	206
(Zr _{0.23} Ti _{0.20} Hf _{0.19} V _{0.14} Ta _{0.24})B ₂	NRMS	Hexagonal	47.2 ± 1.8	540.1 ± 17.1	—	208

^a RMS-reactive magnetron sputtering; F_{N2}-nitrogen flow-rate ratio; VAC-vacuum arc evaporation; VAD-vacuum arc deposition; PLS-pressureless sintering; BCR-boro/carbothermal reduction; HP-hot pressing; NRMS-non-reactive magnetron sputtering; D_R-deposition rates; CTR-carbothermal reduction; SSR-solid state reaction; RFS-reactive flash sintering; UHS-ultrafast high-temperature sintering.

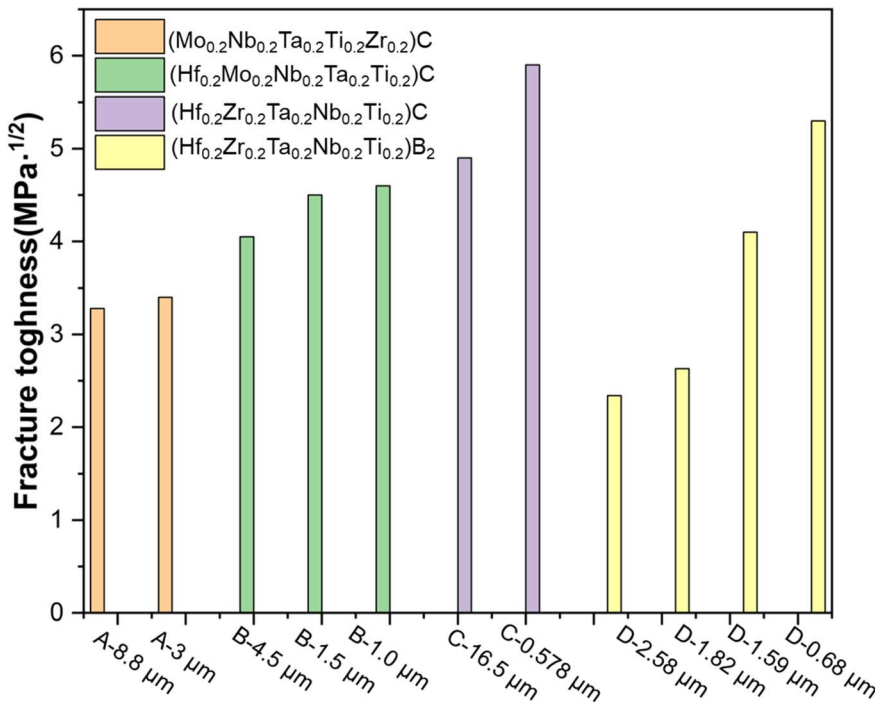


Fig. 16 Comparison of fracture toughness in high-entropy ceramics with different grain sizes.^{35,36,46,210–213}

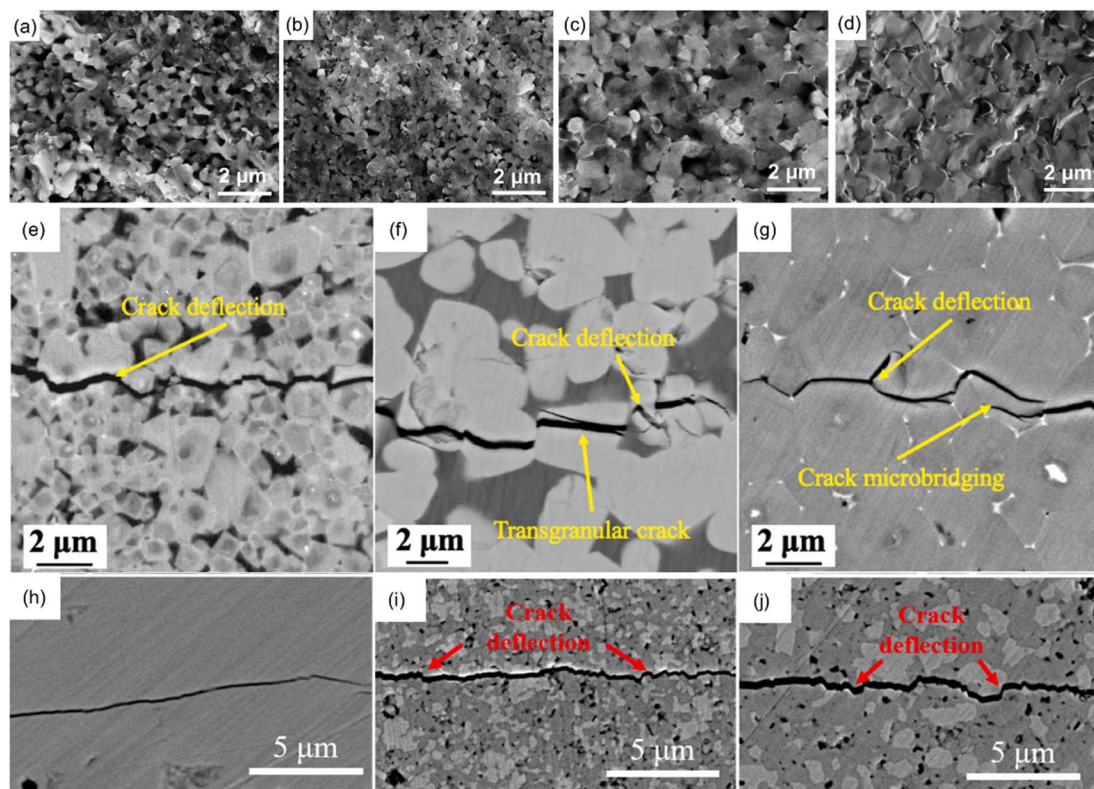


Fig. 17 (a–d) Fracture surface SEM images of the as-sintered samples at different temperatures. Reproduced from ref. 213 with permission from John Wiley and Sons, copyright 2020. (a) 1373 K, (b) 1573 K, (c) 1773 K, and (d) 1973 K; BSE micrographs of the fracture surface and crack propagation of samples of HECN1-Co-Ni, $(\text{Ti}_{0.2}\text{W}_{0.2}\text{Mo}_{0.2}\text{Nb}_{0.2}\text{Ta}_{0.2})(\text{C}_{0.78}\text{N}_{0.22})$ -Co-Ni and TiCN-Co-Ni. (e) Crack propagation of HECN1-Co-Ni, (f) crack propagation of $(\text{Ti}_{0.2}\text{W}_{0.2}\text{Mo}_{0.2}\text{Nb}_{0.2}\text{Ta}_{0.2})(\text{C}_{0.78}\text{N}_{0.22})$ -Co-Ni and (g) crack propagation of sample TiCN-Co-Ni. Reproduced from ref. 214 with permission from Elsevier, copyright 2023; SEM micrographs of crack propagation in (h) CA0-2000, (i) CA2.5-1450 and (j) CA5-1450. Reproduced from ref. 215 with permission from Elsevier, copyright 2023.

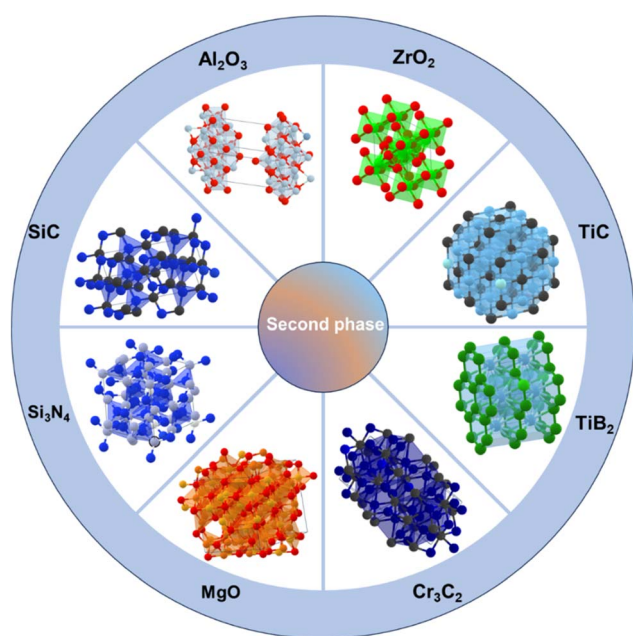


Fig. 18 Second-phase reinforced particle/fiber crystal patterns that are commonly used in ceramics (the above crystal structures are from website <https://next-gen.materialsproject.org/>).

mechanism of SiC. Additionally, the crystallographic properties of selected HEC- x SiC samples were analyzed using EBSD, and the findings are illustrated in Fig. 19(d)–(i). It was suggested that when the SiC content was below 15vol%, the crack mainly propagated through the particle while maintaining the previous path (Fig. 19(j) and (k)). However, as the SiC content increased to a relatively large value, a significant deflection of the crack path was observed. This was attributed to the predominant occurrence of SiC debonding and pullout, which accompanied the deflection of the crack (Fig. 19(l)). In addition, the SiC particles can bridge the extended cracks and provide a closing stress to hinder the formation of a new crack surface, consequently enhancing the fracture toughness. As the crack continues to propagate, the bridge will experience failure due to the separation of the weak interface with low fracture energy, specifically the HEC/SiC_p interface and SiC_p grain boundary.²¹⁶ Additionally, SiC_p will also be pulled out to enhance energy dissipation,²¹⁸ leading to further enhancement of fracture toughness.

Additionally, Al_2O_3 is often used to toughen ceramics due to its high strength and high melting point. $\text{Al}_2\text{O}_3/(\text{Y}_{0.2}\text{Er}_{0.2}\text{Yb}_{0.2}\text{Ho}_{0.2}\text{Lu}_{0.2})_3\text{Al}_5\text{O}_{12}$ high-entropy oxide ceramics exhibit comparable flexural strength (333 MPa) and fracture toughness ($6.8 \text{ MPa m}^{1/2}$).²¹⁷ As depicted in Fig. 19(m)–(p), the interface of

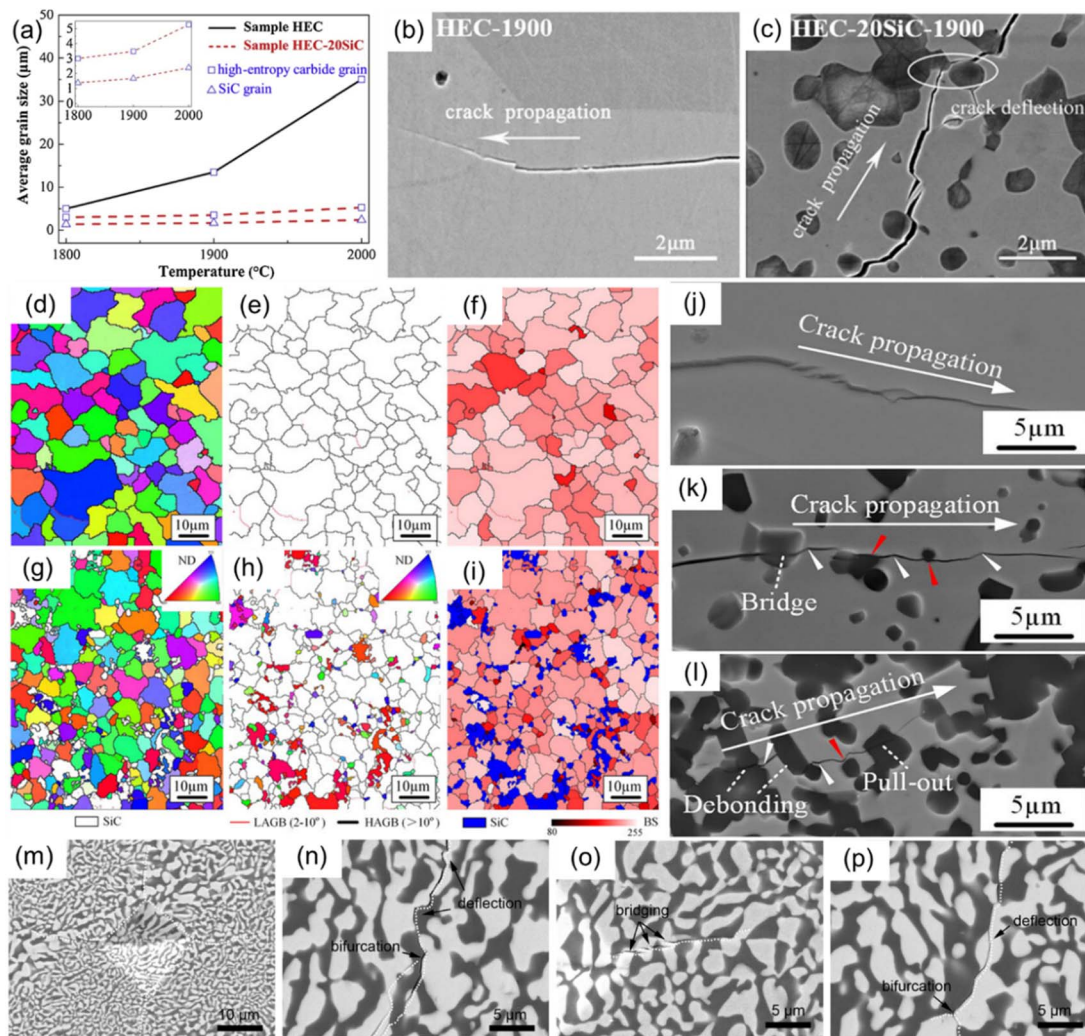


Fig. 19 (a) Average grain size of each phase in the HEC and HEC-20SiC samples as a function of sintering temperature; (b and c) SEM images of the related crack propagations; electron back scattered diffraction (EBSD) results of representative high-entropy carbide ceramic (HECC)-xSiC samples with different SiC_p contents. Reproduced from ref. 17 with permission from Elsevier, copyright 2019; (d–f) HECC-0 sample and (g–i) HECC-30 sample; scanning electron microscopy (SEM) images of crack paths obtained by the Vickers indentation test: (j) HECC-0; (k) HECC-15; and (l) HECC-50. Reproduced from ref. 216 with permission from John Wiley and Sons, copyright 2023. Note that the white triangle indicates crack deflection that occurred inside the high-entropy carbide ceramic (HECC) matrix and red triangle implies the crack deflection in the vicinity of the HECC/SiC_p interface; the SEM image of indentation crack deflection, bifurcation, and bridging in the microstructure of directional solidified Al₂O₃/(Y_{0.2}Er_{0.2}Yb_{0.2}Ho_{0.2}Lu_{0.2})₃Al₅O₁₂ eutectic HEOCs (m–p). Reproduced from ref. 217 with permission from Elsevier, copyright 2021.

Al₂O₃ and (Y_{0.2}Er_{0.2}Yb_{0.2}Ho_{0.2}Lu_{0.2})₃Al₅O₁₂ exhibits the phenomena of indentation crack deflection, bifurcation, and bridging. Thereby, the primary toughening mechanisms can be attributed to crack bridging, deflection, and bifurcation.

3.4.3 In situ self-toughening. *In situ* self-toughening is to form ceramic composite materials by adding an inducer to the ceramic matrix or a raw material that can generate a second phase, so that uniformly distributed whiskers, grains and other reinforcements are generated in the ceramic matrix.²¹⁹ The mechanism of *in situ* self-reinforcement is highly similar to that of second-phase strengthening, with the former achieved by regulating the generation conditions or reaction process to enable the autonomous generation of uniformly distributed second phases. Thereby, *in situ* self-toughening can make the toughened phase more compatible with the ceramic matrix.

A new strategy using the low chemical affinity between W and N to prepare an *in situ* W₂C particle reinforced (Ti,Ta,Nb,Zr,W)(C,N) high-entropy ceramic was proposed by Li *et al.*²²⁰ The (Ti,Ta,Nb,Zr,W)(C,N) HEC demonstrated a significant hardness of 23.46 GPa, as well as an outstanding fracture toughness of 4.59 MPa m^{1/2}. The diffusion of W and uniformly distributed W₂C particles in the high-entropy carbonitride matrix enhances the mechanical properties due to the high-entropy effect and dispersion strengthening mechanism. With increasing sintering temperature, the W₂C diffraction peak decreases, indicating the progressive diffusion of W into the lattice of the HEC. In addition, due to the diffusion of W into the high-entropy ceramic matrix, the reduction of the W₂C phase also brings about an increase in the Vickers hardness. The grain size and distribution of the W₂C phase are the main factors

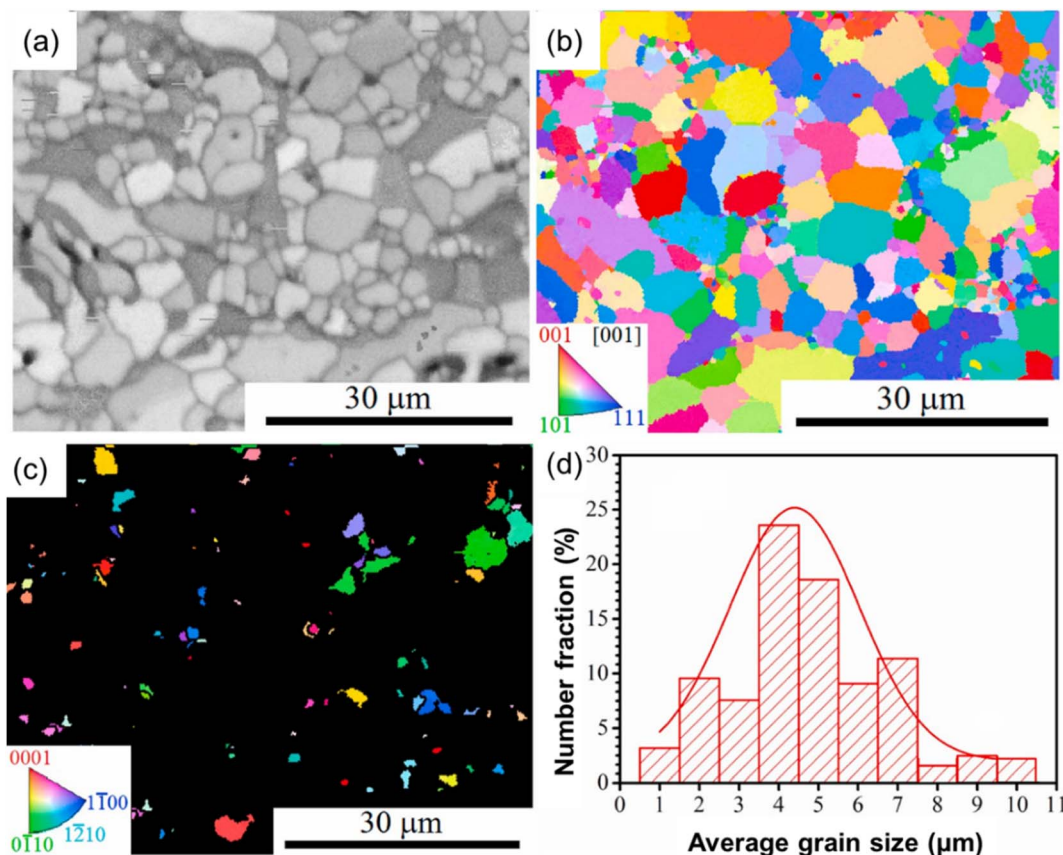


Fig. 20 Microstructure of $\text{Al}_2\text{O}_3/(\text{NbTaMoW})\text{C}$ composites: (a) SEM image and corresponding EBSD mapping (b and c) EBSD mapping of Al_2O_3 and (d) grain size distribution of $(\text{NbTaMoW})\text{C}$ and Al_2O_3 composites. Reproduced from ref. 222 with permission from Elsevier, copyright 2021.

affecting the fracture toughness. However, as the sintering temperature increases to a certain extent, the coarse particles of W_2C are significantly reduced and uniformly distributed in the matrix, thus improving the fracture toughness of the HEC.²²¹

The $\text{Al}_2\text{O}_3/(\text{NbTaMoW})\text{C}$ HEC demonstrate excellent fracture toughness ($4.5 \text{ MPa m}^{1/2}$) and comparable flexural strength (530 MPa).²²² Fig. 20(a) and (b) depict the microstructural characteristics of composites consisting of $\text{Al}_2\text{O}_3/(\text{NbTaMoW})\text{C}$. The incorporation of a specific quantity of Al_2O_3 into the HEC has been shown to significantly enhance the flexural strength and fracture toughness of $(\text{NbTaMoW})\text{C}$. As depicted in Fig. 20(c), the distribution of Al_2O_3 grains within the HEC matrix appears to be random. The haphazard arrangement of Al_2O_3 demonstrates the ability to effectively resist the applied force and impede the spread of fractures in the matrix. Furthermore, the bonding strength at the interface between Al and $(\text{NbTaMoW})\text{C}$ HEC significantly impacts the flexural strength and fracture toughness of the resultant specimens. Fig. 20(d) demonstrates the grain size distribution of $(\text{NbTaMoW})\text{C}$ and Al_2O_3 composites. It was suggested that the *in situ* fabricated Al_2O_3 and a lower sintering temperature can significantly reduce the grain size, leading to a considerable strengthening effect.¹⁷ Additionally, the disparate coefficients of thermal expansion between Al_2O_3 and the ceramic matrix often result in residual stresses.¹⁷ During the process of crack propagation, the residual stress will be released, thereby reducing the stress intensity at

the crack tip. Consequently, the prepared samples can withstand larger loads before fracturing, leading to an improvement in flexural strength.

3.4.4 Nanocomposite toughening. The fabrication of nanocomposite structures necessitates a sufficient chemical driving force to induce the segregation of elements.²²³ It has been proposed that the formation of a nano-composite structure represents an efficient method for enhancing the strength of materials while maintaining their toughness. The toughening mechanism of a nanocomposite structure involves the passivation effect of the metal phase at the crack tip and the inhibition effect of the phase interface on crack propagation.²²⁴

Li *et al.*²²⁴ successfully prepared a nanocomposite ($\text{CuNiTiNbCr})\text{N}_x$ thin film by introducing N atoms to react with Ti, Nb, and Cr to generate the $(\text{TiNbCr})\text{N}$ phase. Fig. 21(a) displays the microstructural features of the $(\text{CuNiTiNbCr})\text{N}_x$ high-entropy films deposited at a flow rate of 6 sccm, as examined through TEM and STEM. The nanocomposite $(\text{CuNiTiNbCr})\text{N}_x$ high entropy films demonstrate elevated levels of hardness (18.3 GPa) and comparable toughness ($1.17 \text{ MPa m}^{1/2}$). It was proposed that the enhancement of hardness can be attributed to the development of nanocrystalline nitride phases. In addition, the excellent mechanical properties can be attributed to the significant reduction in crack propagation length due to the presence of numerous interfaces within the structure of the

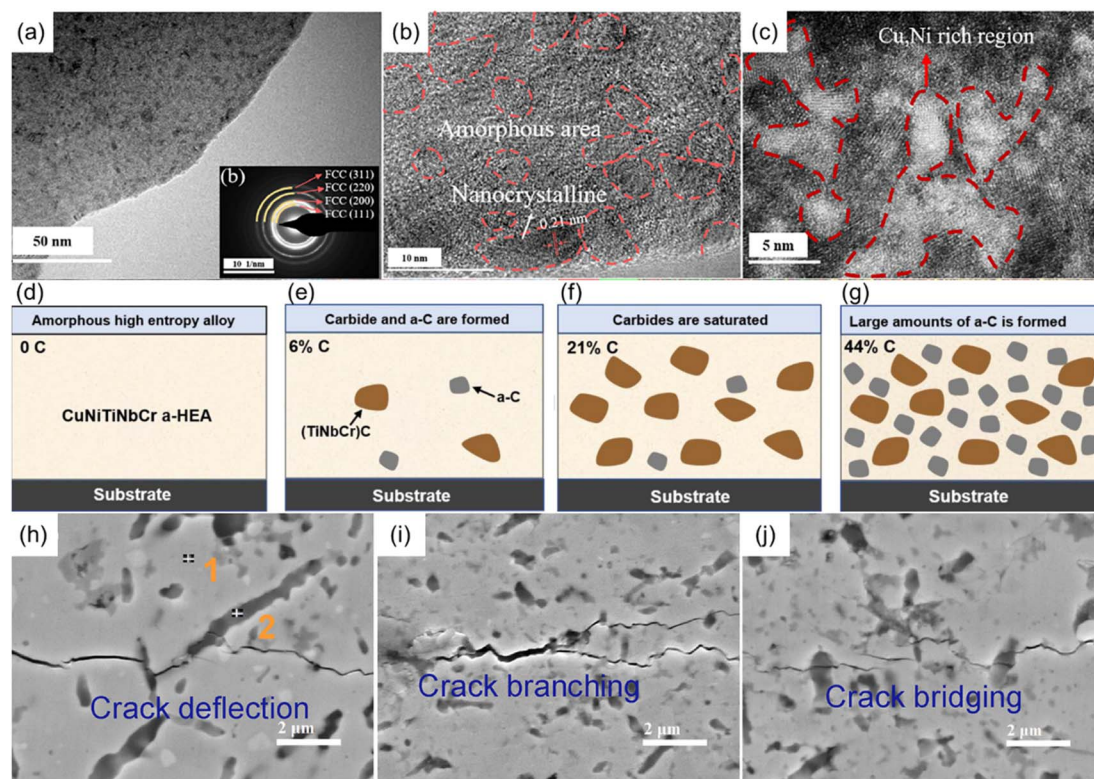


Fig. 21 TEM and STEM images of $(\text{CuNiTiNbCr})\text{N}_x$ films deposited at $F_N = 6$ sccm, (a) the low magnified TEM image; (b) the corresponding selected area electron diffraction pattern; (c) the high-resolution TEM image. Reproduced from ref. 224 with permission from Elsevier, copyright 2023; (d–g) schematic diagram of structural evolution of $(\text{CuNiTiNbCr})\text{C}_x$ HEFs with carbon content. Reproduced from ref. 223 with permission from Elsevier, copyright 2024; toughening mechanisms in HEC– SiC_{nw} . (h) Crack deflection, (i) crack branching, and (j) crack bridging. Reproduced from ref. 225 with permission from Elsevier, copyright 2021.

nanocomposite material, which impedes the expansion of cracks.

Additionally, they employed a similar approach to fabricate $(\text{CuNiTiNbCr})\text{C}_x$ high-entropy nanocomposite films with excellent hardness and fracture toughness.²²³ It was suggested that with the introduction of C atoms, there is a preference for the formation of a stable $(\text{TiNbCr})\text{C}$ phase through the reaction of C with Ti, Nb, and Cr. The schematic illustrations depicting the structural changes in high entropy ceramics as the carbon content increases are presented in Fig. 21(d)–(g). As the carbon content reaches 21%, the high-entropy film exhibits the highest hardness of 18 GPa (Fig. 21(f)), attributed to the predominant presence of the stable $(\text{TiNbCr})\text{C}$ phase in the matrix. When the carbide phase reaches saturation, excess C atoms precipitate in the form of C–C bonds (a-C phase). As depicted in Fig. 21(g), the dominance of the a-C phase in the matrix becomes evident as the C content increases to 44%. The fracture toughness of high-entropy films increases with the increase in carbon content, reaching its peak value of $1.28 \text{ MPa m}^{1/2}$ at a C content of 44%. It was proposed that the primary factor contributing to the enhancement of fracture toughness is the hindrance of crack propagation due to the presence of numerous phase interfaces within the nanocomposite structure.^{226,227}

We have successfully enhanced the densification and fracture toughness of HECs by employing nanomaterials such as

multilayer graphene and SiC nanowires (SiC_{nw}).²²⁵ HEC-multilayer graphene and HEC– SiC_{nw} ceramics demonstrated flexural strengths of 671.3 MPa and 626.5 MPa, along with fracture toughness values of $7.1 \text{ MPa m}^{1/2}$ and $6.2 \text{ MPa m}^{1/2}$, respectively. Due to the presence of SiC_{nw} , crack deflection, crack branching, and crack bridging have been observed in HEC– SiC_{nw} , resulting in its excellent fracture toughness being demonstrated as shown in Fig. 21(h)–(j). The high toughness of HEC-multilayer graphene is related to the inherent bending and sliding behavior of multilayer graphene. Furthermore, the friction between the multilayer graphene and HEC matrix serves as a bridging force, resulting in enhanced resistance to crack propagation and significantly improved fracture toughness.

3.4.5 Multianionic structure strengthening. Previous research has demonstrated that increasing configurational entropy is a powerful method for enhancing the toughness of materials.^{27,228} The disorder in the composition of cation and anion sites in HECs results in a significant increase in configurational entropy.

A class of high-entropy carbide-nitrides ceramics, $(\text{Ti}_{0.33}\text{Zr}_{0.33}\text{Hf}_{0.33})(\text{C}_{0.5}\text{N}_{0.5})$ (HEC-1), $(\text{Ti}_{0.25}\text{Zr}_{0.25}\text{Hf}_{0.25}\text{Nb}_{0.25})(\text{C}_{0.5}\text{N}_{0.5})$ (HEC-2), and $(\text{Ti}_{0.2}\text{Zr}_{0.2}\text{Hf}_{0.2}\text{Nb}_{0.2}\text{Ta}_{0.2})(\text{C}_{0.5}\text{N}_{0.5})$ (HEC-3), with multi-anionic structures has been successfully prepared.²²⁹ In Fig. 22(a), the fracture toughness and Vickers hardness of the three samples are shown. The fracture

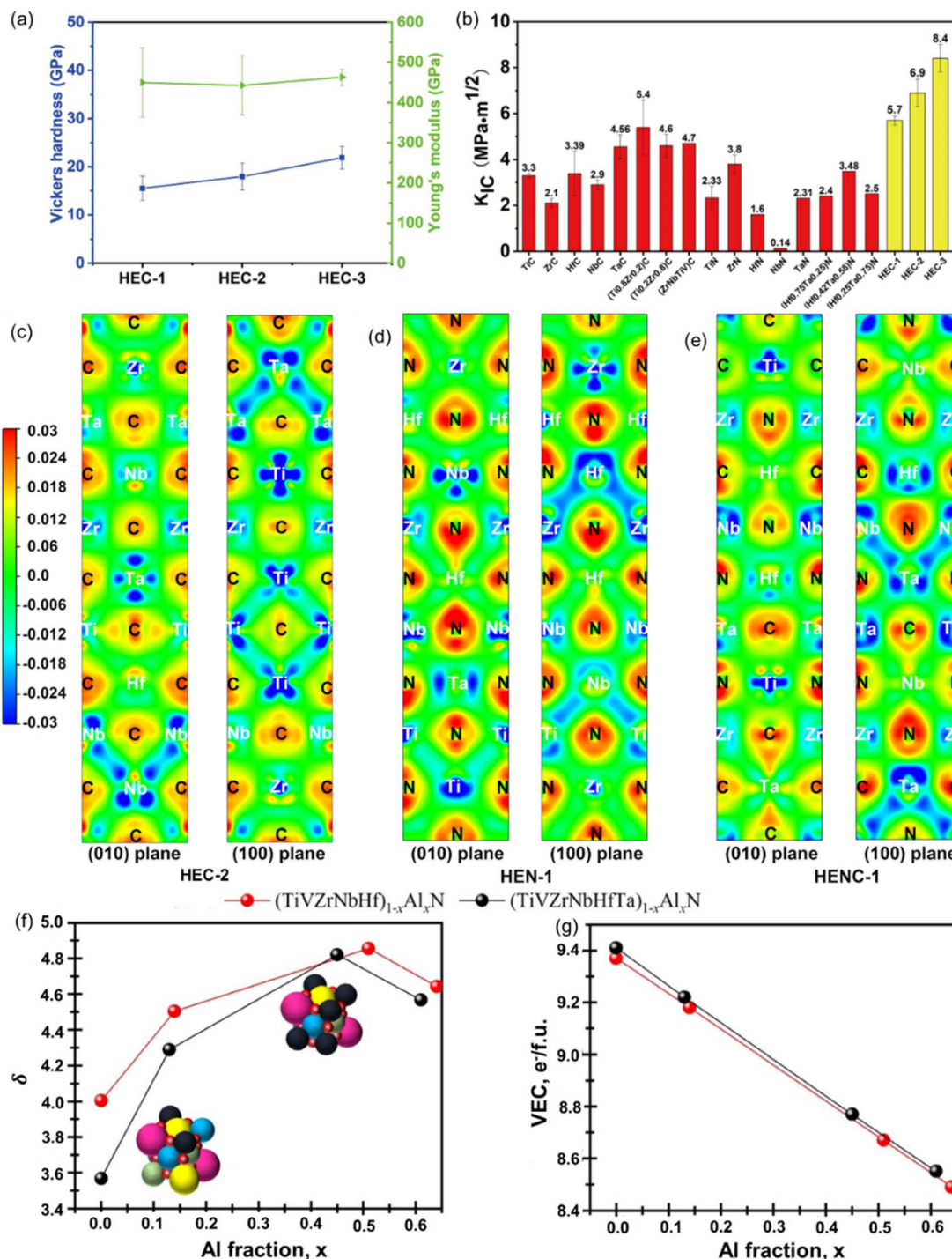


Fig. 22 (a) Vickers hardness and Young's modulus of HECs with the standard deviation of the error bar; (b) fracture toughness of HECs and the data reported in the literature. Reproduced from ref. 229 with permission from Springer Nature, copyright 2021; the CDD of (c) HEC-2, (d) HEN-1, and (e) HENC-1. Reproduced from ref. 230 with permission from John Wiley and Sons, copyright 2020; (f) calculated lattice distortion (δ); (g) VEC $e^-/\text{f. u.}$ ²³¹ Reproduced under the terms of the CC-BY 4.0 license. Copyright 2022, the authors, published by Elsevier.

toughness of HEC-1, HEC-2 and HEC-3 is 5.7, 6.9 and 8.4 $\text{MPa m}^{1/2}$ (Fig. 22(b)), respectively. Furthermore, the fracture toughness of HEC-3 is nearly three times that of traditional carbides and nitrides,^{232–234} which may demonstrate the enhancing effect of multi-anionic structures on fracture toughness.²²⁹

($\text{Hf}_{0.2}\text{Zr}_{0.2}\text{Ta}_{0.2}\text{Nb}_{0.2}\text{Ti}_{0.2}$)($\text{N}_{0.5}\text{C}_{0.5}$) (HENC-1), with a multi-anion structure, exhibits higher hardness and elastic modulus compared to ($\text{Hf}_{0.2}\text{Zr}_{0.2}\text{Ta}_{0.2}\text{Nb}_{0.2}\text{Ti}_{0.2}$)N (HEN-1) and ($\text{Hf}_{0.2}\text{Zr}_{0.2}\text{Ta}_{0.2}\text{Nb}_{0.2}\text{Ti}_{0.2}$)C (HEC-2).²³⁰ The data presented in Fig. 22(c)–(e) illustrate that the charge density distribution (CDD) values for the three samples are almost in the same

range, suggesting that their electronic structures and bonding characteristics exhibit a high degree of similarity. The existence of multi-anionic sublattice structures in HENC-1 samples can lead to substantial mass disorder and distortion of the lattice. It has been suggested that mass disorder can lead to impedance mismatch, resulting in the reflection and dispersion of group energy, potentially resulting in an increase in hardness and modulus.¹⁰⁹ Unfortunately, HENC-1 with a multi-anionic structure did not show satisfactory improvement in fracture toughness ($2.8 \text{ MPa m}^{1/2}$).

High-entropy nitride films with multi-anionic structures of hexavalent $(\text{TiHfNbVZr})_{1-x}\text{Al}_x\text{N}$ and heptanary $(\text{TiHfNbVZrTa})_{1-x}\text{Al}_x\text{N}$ were synthesized.²³¹ In hexanary films, the hardness demonstrates an increase from approximately 30.86 GPa at $x = 0$ to 34.68 GPa at $x = 0.51$. Similarly, for heptanary films, the respective values are 29.41 GPa at $x = 0$ and $33.09 \pm 1.85 \text{ GPa}$ at $x = 0.45$. As depicted in Fig. 22(f), an increase in the Al content within the cation sublattice leads to an escalation in the disruption of symmetry associated with lattice distortion. Furthermore, the elevated VEC values in Al-free and low- x systems can promote additional effects based on the formation of SFs (Fig. 22(g)). By restricting dislocation motion on SFs, additional hardness can be achieved. It has been

proposed that the increase in hardness may be due to significant lattice distortion and robust ionic metal–N bonding in the Al-rich single-phase films. Furthermore, the heptanary single-phase films with the highest Al content demonstrate a high yield strength resulting from the synergistic effect of multiple strengthening mechanisms, with lattice friction strengthening playing a predominant role. The hexavalent single-phase high entropy film of $x = 0.51$ also exhibits good plasticity due to phase transformation-induced toughening.

3.4.6 Dual-phase strengthening/toughening. Dual-phase strengthening/toughening refers to the process of effectively dispersing and compounding heterogeneous phases to uniformly disperse them in a ceramic matrix to obtain composite materials. In dual-phase ceramics, the second phase is no longer simple crystal whiskers or fibers, but rather another ceramic component. The emergence of dual-phase high-entropy ceramics has provided a new platform for high-entropy ceramics with superior performance. This allows for customization of various properties by altering phase fractions and microstructures.

The HV1 hardness the $(\text{Ti}_{0.14}\text{Zr}_{0.2}\text{Nb}_{0.2}\text{Hf}_{0.2}\text{Ta}_{0.26})\text{C}/(\text{Ti}_{0.38}\text{Zr}_{0.18}\text{Nb}_{0.22}\text{Hf}_{0.115}\text{Ta}_{0.105})\text{B}_2$ reaches 29.4 GPa, demonstrating concurrently a reasonable fracture toughness ($3.9 \text{ MPa m}^{1/2}$).²³⁵

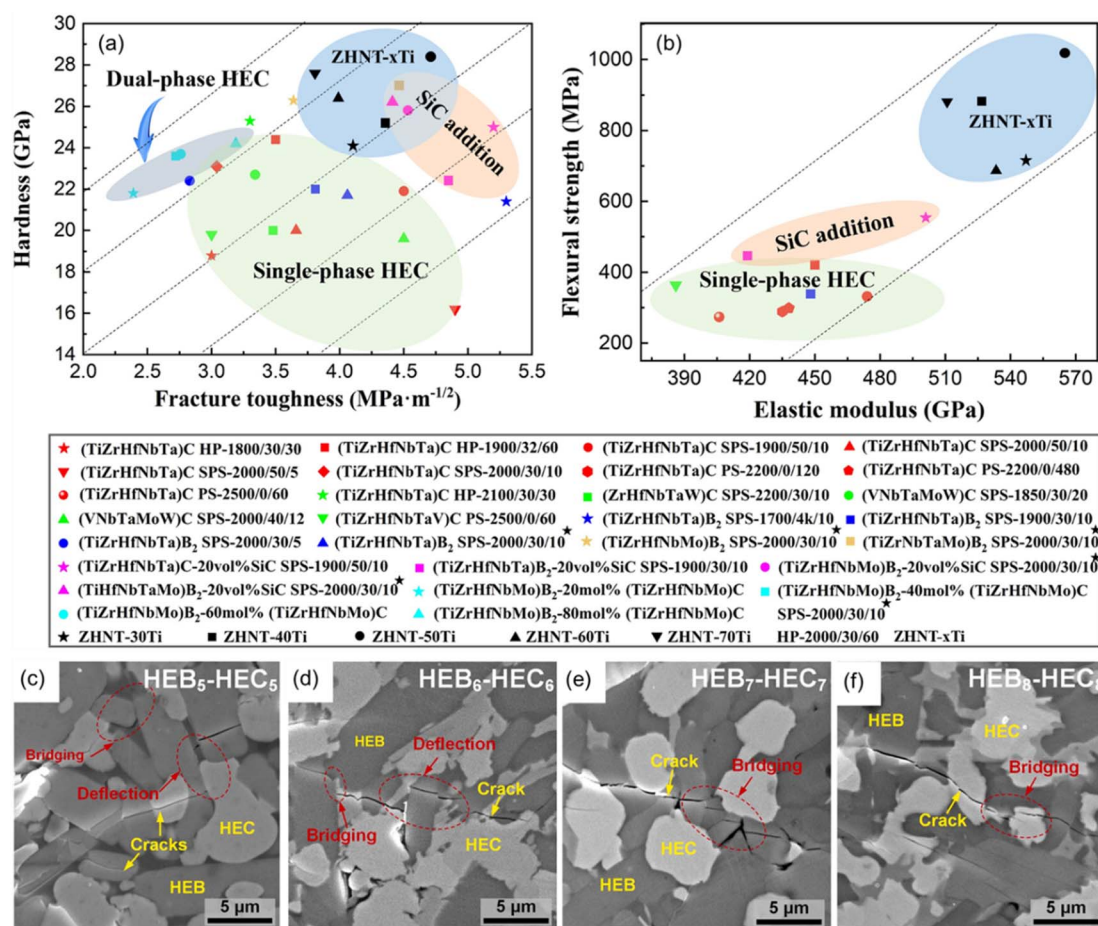


Fig. 23 Ashby plots showing (a) hardness vs. fracture toughness and (b) flexural strength vs. elastic modulus relationships for high-entropy ceramics from this work and other studies. Reproduced from ref. 236 with permission from Elsevier, copyright 2022; (c–f) crack deflection behavior of $\text{HEB}_5\text{-HEC}_5$, $\text{HEB}_6\text{-HEC}_6$, $\text{HEB}_7\text{-HEC}_7$ and $\text{HEB}_8\text{-HEC}_8$. Reproduced from ref. 237 with permission from Elsevier, copyright 2023.

Huo *et al.*²³⁶ prepared dual-phase high-entropy ceramic ZHNT-50Ti that exhibited a bending strength of up to 1017 MPa and a fracture toughness of 4.7 MPa m^{1/2}. As depicted in Fig. 23(a) and (b), a range of dual-phase high-entropy ceramics (ZHNT-*x*Ti, *x* = 30, 40, 50, 60, 70) prepared by Huo *et al.* exhibited superior mechanical properties compared to other high-entropy ceramics, with ZHNT-50Ti demonstrating the most outstanding mechanical performance. It was suggested that in ZHNT-50Ti, the volume fractions of diborides and carbides are closely comparable, resulting in a higher presence of grain boundaries and interfaces that impede the movement of grains, thereby inhibiting grain growth. Consequently, the refined grain structure enhanced the mechanical properties of ZHNT-50Ti.

Luo *et al.*²³⁸ prepared various dual-phase high-entropy ceramics (Ti_{0.2}Zr_{0.2}Hf_{0.2}Nb_{0.2}Ta_{0.2})B₂-(Ti_{0.2}Zr_{0.2}Hf_{0.2}Nb_{0.2}Ta_{0.2})C with different compositions by adjusting the content of B₄C and C in the precursor powders. Among them, B2C8 exhibited Vickers hardness as high as 24.4 GPa and a fracture toughness of 3.19 MPa m^{1/2}. The experimental findings demonstrate that the Vickers hardness and fracture toughness of

(Ti_{0.2}Zr_{0.2}Hf_{0.2}Nb_{0.2}Ta_{0.2})B₂ are 21.3 GPa and 2.34 MPa m^{1/2}, respectively, while those of (Ti_{0.2}Zr_{0.2}Hf_{0.2}Nb_{0.2}Ta_{0.2})C are 23.1 GPa and 3.04 MPa m^{1/2}. It was proposed that improving the mechanical properties of high-entropy ceramics can be achieved through proper adjustment of the phase fractions.

Furthermore, it was suggested that crack deflection or blunting and bridging of rod-like diborides or boron-rich phases play a role in enhancing the fracture toughness of dual-phase high-entropy ceramics. Guo *et al.*²³⁷ synthesized a series of dual-phase high-entropy ceramic, denoted as HEB_{*x*}-HEC_{*x*} (*x* = 5, 6, 7, 8), among which component HEB₅-HEC₅ exhibited exceptional fracture toughness (5.4 MPa m^{1/2}). As illustrated in Fig. 23(c)–(f), crack blunting was observed when a crack intersected a phase rich in boron. Furthermore, despite the reduced boron content in HEB₅-HEC₅ and HEB₆-HEC₆ phases, the presence of rod-like diborides still induces crack deflection, thereby enhancing fracture toughness.

3.4.7 Gradient structure strengthening/toughening. A gradient structure material is a type of functional material characterized by a composition and structure that transition continuously from one orientation to another. This results in

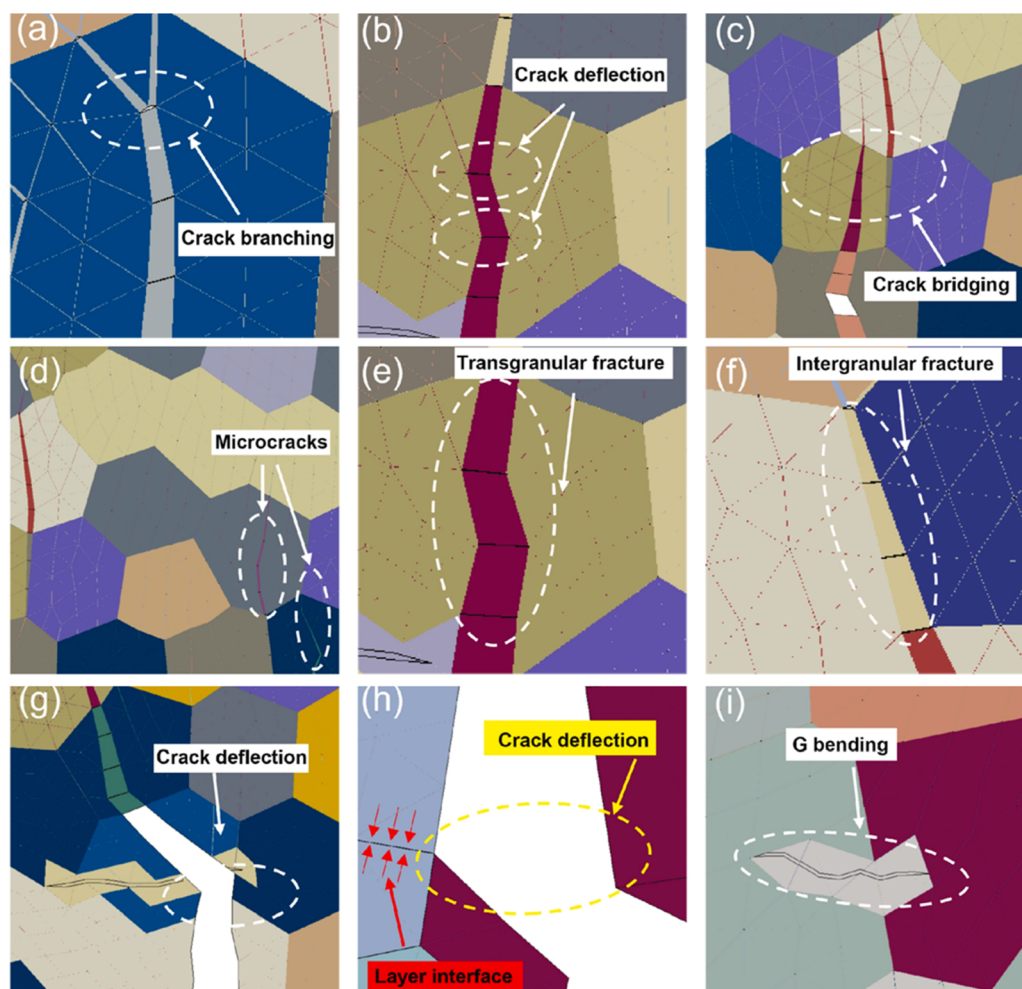


Fig. 24 Schematic of crack propagation of a G/(HfNbTaTiZr)C-Al₂O₃ gradient composite (the surface content of G is 0.20%). Reproduced from ref. 239 with permission from Elsevier, copyright 2024. (a) Crack branching; (b) crack deflection; (c) crack bridging; (d) microcracks; (e) transgranular fracture; (f) intergranular fracture; (g) crack deflection; (h) layer interface; (i) G bending.

gradients in the composition, properties, and functionality of the material.²³⁹

In order to investigate the influence of the gradient structure on the mechanical properties of high-entropy ceramics, a five-layer symmetrical gradient composite material of G/(HfNbTaTiZr)C-Al₂O₃ with a layer thickness ratio of 0.2 was established using Abaqus using the Python language.²³⁹ The flexural strength and fracture toughness of G/(HfNbTaTiZr)C-Al₂O₃ are reported to be 863 MPa and 8.18 MPa m^{1/2}, respectively. Fig. 24 illustrates the toughening mechanism obtained from the simulation of crack propagation in G/(HfNbTaTiZr)C-Al₂O₃. From Fig. 24, it can be observed that the presence of crack bridging in G/(HfNbTaTiZr)C-Al₂O₃ hinders crack propagation, thereby enhancing its fracture toughness. In addition, as illustrated in Fig. 24(g) and (h), the crack undergoes deflection upon encountering graphene and traversing various layers, thereby expending energy to enhance the fracture toughness of the composite material.

4. Concluding remarks and outlook

In summary, this article provides an overview of the latest research progress in HEICs and HECs, presenting predictive criteria for their phase structures and the associated mechanical properties. Additionally, it emphasizes the relevant strengthening/toughening strategies for HEICs and HECs, with the aim of accelerating the development of high-performance materials. In this context, we provide a concise overview of various crucial topics and potential avenues for future

investigations concerning HEICs and HECs. The application of high-entropy materials is continuously expanding. Owing to their exceptional corrosion resistance and high-temperature performance, high-entropy materials are driving advancements and developments in the field of coatings. Furthermore, high-entropy materials present a novel paradigm for the design of catalysts. Multi-component alloys, which incorporate a variety of elements, demonstrate intricate synergistic interactions that arise from the presence of multiple and diverse active sites.²⁴⁰ It has been suggested that high-entropy alloys can serve as an economical and reliable catalyst for the complete decomposition of seawater.²⁴¹ The application domains of high-entropy materials are extensive, and it is imperative to intensify efforts to promote the diverse applications of these materials in the future.

4.1 High-throughput design

The inclusion of a greater number of constituent elements in HEICs and HECs as novel materials has significantly expanded the exploration space for materials. However, this expansion has also made the rapid design of high-performance materials extremely challenging. Utilizing conventional trial-and-error methods in the development of high-entropy materials has consumed significant amounts of time and effort. With advancements in machine learning and computational techniques, high-throughput computational design is considered one of the crucial tools for developing materials that are both reliable and efficient. Feng *et al.*²⁴² used a CALPHAD-based high-

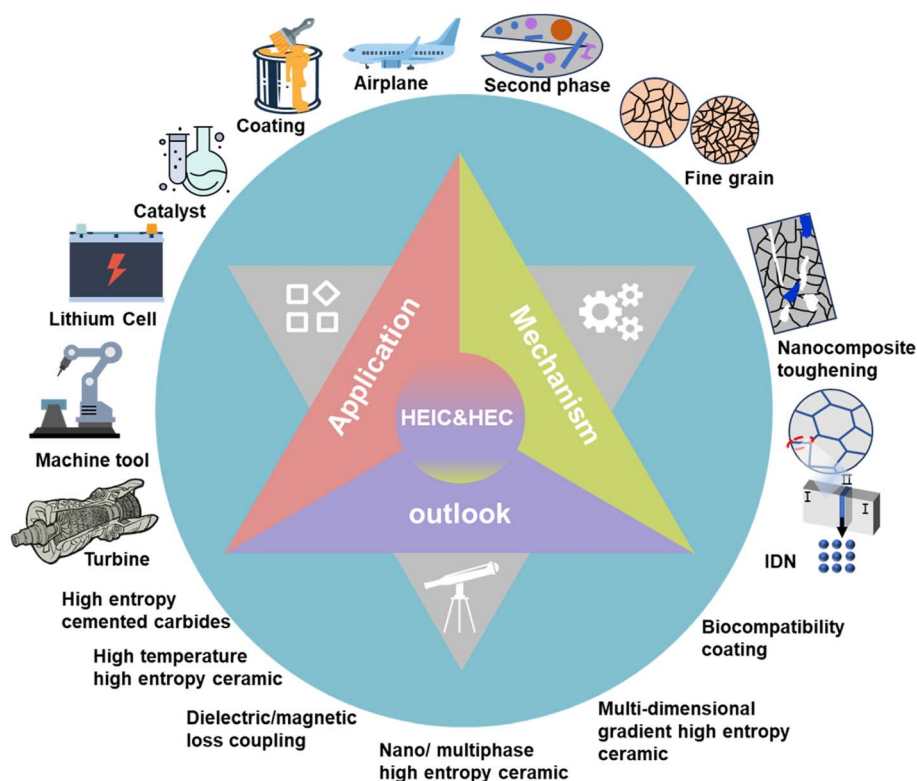


Fig. 25 Schematic diagram of the mechanism, applications, and development trends of HEICs and HECs.

throughput computational method to identify a lightweight high-entropy alloy with precipitation strengthening characteristics from thousands of initial compositions. Compared to other similar materials, this alloy exhibits superior strength performance under both room temperature and high-temperature conditions. The mechanical properties of materials are largely influenced by their chemical elemental composition. To address this, a method combining high-throughput design and machine learning has been proposed to achieve the development of high-strength and low-cost medium-entropy alloys.²⁴³ The research results indicate that the combination of high-throughput simulations and machine learning is significant in searching for optimal mechanical properties across a wide range of elemental compositions, which is crucial for developing alloys with desired performance. High-entropy materials are considered promising catalysts due to their extensive chemical space and tunability; however, this also poses challenges for the rational design of high-entropy catalysts. Singh *et al.*²⁴⁴ employed high-throughput density functional theory calculations to create a comprehensive database and developed a high-precision machine learning model aimed at disentangling the relative contributions of ligand and coordination effects in high-entropy alloy catalysts. In the future, further exploration in machine learning and computational methods should be pursued to accelerate the application of high-entropy materials. The scope of high-throughput design should extend beyond the mere prediction of phase structures in high-entropy materials to encompass the evaluation of their synthesizability and the anticipation of their mechanical properties. In addition, the databases of HEICd and HECd should also be set up to facilitate the discovery of high performance and high entropy materials.

4.2 Microstructural control and mechanical properties at elevated temperatures

HEICs exhibit high temperature strength and stability, enabling their potential applications in high-temperature environments. Similarly, HECs can maintain their original structure in extreme temperatures, pressures and chemical environments, making them stable in various working environments. High-entropy materials have demonstrated significant potential in terms of their mechanical properties at elevated temperatures. As depicted in Fig. 25, HECs are expected to play a significant role in cutting tools and aerospace heat-resistant insulation components due to their excellent hardness and high temperature stability. The high-entropy superalloys $\text{Al}_{10.3}\text{Co}_{17}\text{Cr}_{7.5}\text{Fe}_9\text{Ni}_{48.6}\text{Ti}_{5.8}\text{Ta}_{0.6}\text{Mo}_{0.8}\text{W}_{0.4}$ and $\text{Al}_{7.8}\text{Co}_{20.6}\text{Cr}_{12.2}\text{Fe}_{11.5}\text{Ni}_{40.7}\text{Ti}_{7.2}$, developed by Tsao *et al.*,²⁴⁵ exhibit remarkable high-temperature and mechanical properties. Notably, the high-temperature hardness of $\text{Al}_{10.3}\text{Co}_{17}\text{Cr}_{7.5}\text{Fe}_9\text{Ni}_{48.6}\text{Ti}_{5.8}\text{Ta}_{0.6}\text{Mo}_{0.8}\text{W}_{0.4}$ surpasses that of conventional nickel-based superalloys. Furthermore, the high-temperature strength of $\text{Al}_{7.8}\text{Co}_{20.6}\text{Cr}_{12.2}\text{Fe}_{11.5}\text{Ni}_{40.7}\text{Ti}_{7.2}$, after aging for 5 hours at 900 °C, exceeds that of the Inconel 617 alloy. Senkov *et al.*^{246,247} synthesized refractory high-entropy alloys composed of refractory elements. Among these, two specific HEAs, NbMoTaW and VNbMoTaW, exhibit a single-phase

disordered BCC structure and demonstrate a yield strength exceeding 400 MPa at a temperature of 1600 °C. In addition, the antioxidant properties of high-entropy materials represent a critical factor influencing their performance in extreme environments. During high-temperature oxidation processes, prevalent failure modes are frequently observed in aircraft engines and aerospace propulsion systems. High-entropy alloys, due to their distinctive structure and characteristics, demonstrate exceptional high-temperature oxidation resistance. Research shows that the $\text{Al}_{0.7}\text{CoCrFeNi}$ high-entropy alloy doped with Y/Hf exhibits an extremely low oxidation rate and significant interfacial bonding strength, making it a highly promising high-temperature oxidation-resistant material.²⁴⁸ However, their practical application is significantly constrained by inferior plasticity/toughness. Therefore, it is imperative to conduct a systematic investigation on the relationship between the composition, structure, processing, and performance of HEICs and HECs in order to overcome their deficiencies and propel the application of high-entropy materials in extreme environments. It is believed that HEICs with long-range ordered structures exhibit exceptional strength at elevated temperatures, making them attractive candidates for high-temperature structural applications and potentially serving as substitutes for superalloys²⁴⁹ (Fig. 25). In the future, it is imperative to dedicate increased efforts and endeavors towards researching the high-temperature strength and creep performance of HEICs. On the other hand, it is also needed to investigate the evolution of the microstructure of HEICs and HECs at different temperatures, while quantifying the alloying effects of constituent elements on their high-temperature stability.

4.3 High entropy cemented carbides

High-entropy cemented carbides (HECCs), which utilize high-entropy ceramics as the hard phase and high-entropy alloys as the bonding phase, hold promise for revolutionizing the field of high-performance cutting tools. At present, there is a limited amount of literature on HECCs. Nevertheless, a few researchers have conducted studies on HEA bonded cemented carbides. Due to high-entropy alloys serving as the bonding phase, the WC-HEA exhibits superior mechanical properties and oxidation/corrosion resistance compared to traditional WC-Co cemented carbides. Based on the comparison of the performance of HECCs with other high-entropy materials discussed earlier, it is believed that HECCs will play a significant role in advanced manufacturing industries in the future.

4.4 Dual-phase high entropy ceramics

In addition, research on dual-phase high-entropy ceramics has demonstrated their exceptional mechanical properties. The emergence of dual-phase high-entropy ceramics has provided a new platform for high-entropy ceramics with superior performance. This allows for customization of various properties by altering phase fractions and microstructures. Dual-phase high-entropy ceramics show great promise in applications within ultra-high temperature environments. It was suggested that by controlling two distinct high-entropy ceramic phases, it

is possible to tailor the microstructural characteristics, mechanical properties, and thermal stability of dual-phase high-entropy ceramics. In the future, advancements in sintering technology, sintering aids, and other aspects should be utilized to enhance the densification of dual-phase high-entropy ceramics, while incorporating various strategies to improve their fracture toughness.

4.5 Gradient structure high entropy ceramics

Research has demonstrated that gradient structures can enhance the thermal shock life of high-entropy coatings. High-entropy $(\text{La}_{0.2}\text{Nd}_{0.2}\text{Sm}_{0.2}\text{Eu}_{0.2}\text{Gd}_{0.2})_2\text{Ce}_2\text{O}_7$ (LECO) has been suggested as a promising candidate for use as a thermal barrier material due to its exceptional thermo-physical characteristics. To further enhance the thermal stress resistance of LECO coatings, gradient multilayer LECO has been developed, consisting of five ceramic sub-layers.²⁵⁰ The thermal shock resistance of multilayer LECO was significantly improved by a factor of approximately four.

The gradient structure is identified as a primary factor contributing to the enhancement of thermal shock resistance in coatings. This underscores the potential of gradient structures in accelerating the application of high-entropy ceramics in the field of high-temperature coatings. However, there is currently limited research on mechanical properties of gradient structures in high-entropy ceramics. Our simulations demonstrate the potential of gradient structures to improve the mechanical properties of high-entropy ceramics,²³⁹ and using gradient structure materials may be an effective strategy for improving the mechanics of high-entropy ceramics in the future.

Data availability

Data will be made available on request.

Author contributions

Bin Li and Jialin Sun conceptualized the article structure, content, and figures. Bin Li, Jialin Sun and Jun Zhao wrote and edited the manuscript.

Conflicts of interest

The authors declare no competing financial or non-financial interests.

Acknowledgements

This work was supported by the National Natural Science Foundation of China (No. 52375451 and 52005396), Shandong Provincial Natural Science Foundation (ZR2023YQ052), Shandong Provincial Technological SME Innovation Capability Promotion Project (2023TSGC0375), Young Taishan Scholars Program of Shandong Province (No. tsqn202306041), Guandong Basic and Applied Basic Research Foundation (2023A1515010044), Shandong Provincial Youth Innovation Team (No. 2022KJ038), Open Project of State Key Laboratory of

Solid Lubrication (LSL-22-11), Young Talent fund of University Association for Science and Technology in Shaanxi (No. 20210414) and Qilu Youth Scholar Project Funding of Shandong University.

References

- 1 J. W. Yeh, S. K. Chen, S. J. Lin, J. Y. Gan, T. S. Chin, T. T. Shun, C. H. Tsau and S. Y. Chang, *Adv. Eng. Mater.*, 2004, **6**, 299–303.
- 2 B. Cantor, I. T. H. Chang, P. Knight and A. J. B. Vincent, *Mater. Sci. Eng., A*, 2004, **375–377**, 213–218.
- 3 Y. Zhang, T. T. Zuo, Z. Tang, M. C. Gao, K. A. Dahmen, P. K. Liaw and Z. P. Lu, *Prog. Mater. Sci.*, 2014, **61**, 1–93.
- 4 Y. Tang, R. Wang, B. Xiao, Z. Zhang, S. Li, J. Qiao, S. Bai, Y. Zhang and P. K. Liaw, *Prog. Mater. Sci.*, 2023, **135**, 101090.
- 5 B. Cantor, *Prog. Mater. Sci.*, 2021, **120**, 100754.
- 6 J. Kottke, M. Laurent-Brocq, A. Fareed, D. Gaertner, L. Perrière, L. Rogal, S. V. Divinski and G. Wilde, *Scr. Mater.*, 2019, **159**, 94–98.
- 7 C. Zhang, F. Zhang, K. Jin, H. Bei, S. Chen, W. Cao, J. Zhu and D. Lv, *J. Phase Equilib. Diffus.*, 2017, **38**, 434–444.
- 8 D. Gaertner, K. Abrahams, J. Kottke, V. A. Esin, I. Steinbach, G. Wilde and S. V. Divinski, *Acta Mater.*, 2019, **166**, 357–370.
- 9 C. M. Rost, E. Sachet, T. Borman, A. Moballegh, E. C. Dickey, D. Hou, J. L. Jones, S. Curtarolo and J.-P. Maria, *Nat. Commun.*, 2015, **6**, 8485.
- 10 J. Gu, J. Zou, S. K. Sun, H. Wang, S. Y. Yu, J. Zhang, W. Wang and Z. Fu, *Sci. China Mater.*, 2019, **62**, 1898–1909.
- 11 X. Q. Shen, J. X. Liu, F. Li and G. J. Zhang, *Ceram. Int.*, 2019, **45**, 24508–24514.
- 12 J. X. Liu, X. Q. Shen, Y. Wu, F. Li, Y. Liang and G. J. Zhang, *J. Adv. Ceram.*, 2020, **9**, 503–510.
- 13 Y. Zhang, Z. B. Jiang, S. K. Sun, W. M. Guo, Q. S. Chen, J. X. Qiu, K. Plucknett and H. T. Lin, *J. Eur. Ceram. Soc.*, 2019, **39**, 3920–3924.
- 14 R. Hahn, A. Kirnbauer, M. Bartosik, S. Kolozsvári and P. H. Mayrhofer, *Mater. Lett.*, 2019, **251**, 238–240.
- 15 L. Feng, W. T. Chen, W. G. Fahrenholtz and G. E. Hilmas, *J. Am. Ceram. Soc.*, 2021, **104**, 419–427.
- 16 F. Wang, X. Zhang, X. Yan, Y. Lu, M. Nastasi, Y. Chen and B. Cui, *J. Am. Ceram. Soc.*, 2020, **103**, 4463–4472.
- 17 K. Lu, J. X. Liu, X. F. Wei, W. Bao, Y. Wu, F. Li, F. Xu and G. J. Zhang, *J. Eur. Ceram. Soc.*, 2020, **40**, 1839–1847.
- 18 D. Moskovskikh, S. Vorotilo, V. Buinevich, A. Sedegov, K. Kuskov, A. Khort, C. Shuck, M. Zhukovskiy and A. Mukasyan, *Sci. Rep.*, 2020, **10**, 19874.
- 19 S. Akrami, P. Edalati, M. Fuji and K. Edalati, *Mater. Sci. Eng., R*, 2021, **146**, 100644.
- 20 C. Oses, C. Toher and S. Curtarolo, *Nat. Rev. Mater.*, 2020, **5**, 295–309.
- 21 M. H. Tsai, *Entropy*, 2016, **18**, 252.
- 22 E. Trofimov, A. Ostovari Moghaddam, K. Litvinyuk and D. Mikhailov, *J. Alloys Compd.*, 2023, **934**, 168021.
- 23 D. Qiao, H. Liang, S. Wu, J. He, Z. Cao, Y. Lu and T. Li, *Mater. Charact.*, 2021, **178**, 111287.

- 24 K. Yao, L. Liu, J. Ren, Y. Guo, Y. Liu, Y. Cao, R. Feng, F. Wu, J. Qi, J. Luo, P. K. Liaw and W. Chen, *Scr. Mater.*, 2021, **194**, 113674.
- 25 H. Li, W. Yang, Y. Ma, F. Kong, Y. Wan, C. Chen, H. Liu, H. Li and A. Inoue, *J. Alloys Compd.*, 2023, **935**, 167897.
- 26 S. Wang, S. Chen, Y. Jia, Z. Hu, H. Huang, Z. Yang, A. Dong, G. Zhu, D. Wang, D. Shu, F. Tian, Y. Dai and B. Sun, *Mater. Des.*, 2019, **168**, 107648.
- 27 T. Yang, Y. L. Zhao, W. P. Li, C. Y. Yu, J. H. Luan, D. Y. Lin, L. Fan, Z. B. Jiao, W. H. Liu, X. J. Liu, J. J. Kai, J. C. Huang and C. T. Liu, *Science*, 2020, **369**, 427–432.
- 28 H. J. Park, Y. S. Na, S. H. Hong, J. T. Kim, Y. S. Kim, K. R. Lim, J. M. Park and K. B. Kim, *Met. Mater. Int.*, 2016, **22**, 551–556.
- 29 Z. Ye, C. Li, M. Zheng, X. Zhang, X. Yang, Q. Wang and J. Gu, *Mater. Res. Lett.*, 2022, **10**, 736–743.
- 30 Q. Tang, H. Su, S. Peng, W. Chen and P. Dai, *Metals*, 2022, **12**, 932.
- 31 N. Y. Yurchenko, N. D. Stepanov, S. V. Zharebtsov, M. A. Tikhonovsky and G. A. Salishchev, *Mater. Sci. Eng., A*, 2017, **704**, 82–90.
- 32 J. Sun, L. Zhao and X. Li, *CN Pat.*, 202211328464, 2022.
- 33 B. Straumal and I. Konyashin, *Metals*, 2023, **13**, 171.
- 34 C. Peng, H. Tang, Y. He, X. Lu, P. Jia, G. Liu, Y. Zhao and M. Wang, *J. Mater. Sci. Technol.*, 2020, **51**, 161–166.
- 35 F. Wang, X. Zhang, X. Yan, Y. Lu, M. Nastasi, Y. Chen and B. Cui, *J. Am. Ceram. Soc.*, 2020, **103**, 4463–4472.
- 36 K. Wang, L. Chen, C. Xu, W. Zhang, Z. Liu, Y. Wang, J. Ouyang, X. Zhang, Y. Fu and Y. Zhou, *J. Mater. Sci. Technol.*, 2020, **39**, 99–105.
- 37 J. Liu, X. Wang, A. Singh, H. Xu, F. Kong and F. Yang, *Metals*, 2021, **11**, 2054.
- 38 A. Manzoni, H. Daoud, R. Völkl, U. Glatzel and N. Wanderka, *Ultramicroscopy*, 2013, **132**, 212–215.
- 39 T. P. Yadav, S. Mukhopadhyay, S. S. Mishra, N. K. Mukhopadhyay and O. N. Srivastava, *Philos. Mag. Lett.*, 2018, **97**, 494–503.
- 40 N. Zhou, S. Jiang, T. Huang, M. Qin, T. Hu and J. Luo, *Sci. Bull.*, 2019, **64**, 856–864.
- 41 Y. L. Zhao, W. C. Xiao, Z. K. Zhao, Q. Li, J. Cui, J. H. Luan, C. T. Liu, P. K. Liaw and T. Yang, *Scr. Mater.*, 2023, **229**, 115371.
- 42 A. Ostovari Moghaddam, D. Mikhailov, R. Fereidonnejad, N. Shaburova, D. Vinnik, D. Uchaev, F.-Q. Bai, D. Janas and E. Trofimov, *J. Alloys Compd.*, 2022, **912**, 165195.
- 43 N. D. Stepanov, N. Y. Yurchenko, D. V. Skibin, M. A. Tikhonovsky and G. A. Salishchev, *J. Alloys Compd.*, 2015, **652**, 266–280.
- 44 O. N. Senkov, S. V. Senkova, D. B. Miracle and C. Woodward, *Mater. Sci. Eng., A*, 2013, **565**, 51–62.
- 45 S. Jiang, T. Hu, J. Gild, N. Zhou, J. Nie, M. Qin, T. Harrington, K. Vecchio and J. Luo, *Scr. Mater.*, 2018, **142**, 116–120.
- 46 J. Gild, Y. Zhang, T. Harrington, S. Jiang, T. Hu, M. C. Quinn, W. M. Mellor, N. Zhou, K. Vecchio and J. Luo, *Sci. Rep.*, 2016, **6**, 37946.
- 47 N. Yurchenko, N. Stepanov and G. Salishchev, *Mater. Sci. Technol.*, 2016, **33**, 17–22.
- 48 S. Guo and C. T. Liu, *Prog. Nat. Sci.*, 2011, **21**, 433–446.
- 49 A. Ostovari Moghaddam, D. Mikhailov, M. Sudarikov, R. Fereidonnejad, A. Cabot and E. Trofimov, *J. Alloys Compd.*, 2022, **927**, 167102.
- 50 Z. Huang, G. Liu, K. Wang, Y. Sun, Y. Yang, M. Yan and Y. Fu, *Physica B*, 2022, **646**, 414275.
- 51 Z. Zhou, Y. Zhou, Q. He, Z. Ding, F. Li and Y. Yang, *npj Comput. Mater.*, 2019, **5**, 128.
- 52 C. Y. Hsu, C. C. Juan, W. R. Wang, T. S. Sheu, J. W. Yeh and S. K. Chen, *Mater. Sci. Eng., A*, 2011, **528**, 3581–3588.
- 53 C. T. Liu and J. O. Stiegler, *Science*, 1984, **226**, 636–642.
- 54 J. Hou, J. Gan, W. Li, H. Tian, X. Luo, J. Ju, Y. Zhou, S. Liu, H. Yao, Z. Chen and T. Yang, *Corros. Sci.*, 2023, **225**, 111607.
- 55 Q. F. He, J. G. Wang, H. A. Chen, Z. Y. Ding, Z. Q. Zhou, L. H. Xiong, J. H. Luan, J. M. Pelletier, J. C. Qiao, Q. Wang, L. L. Fan, Y. Ren, Q. S. Zeng, C. T. Liu, C. W. Pao, D. J. Srolovitz and Y. Yang, *Nature*, 2022, **602**, 251–257.
- 56 S. S. Mishra, S. Mukhopadhyay, T. P. Yadav, N. K. Mukhopadhyay and O. N. Srivastava, *J. Mater. Res.*, 2019, **34**, 807–818.
- 57 Y. H. Meng, F. H. Duan, J. Pan and Y. Li, *Intermetallics*, 2019, **111**, 106515.
- 58 F. R. Long, S. I. Baik, D. W. Chung, F. Xue, E. A. Lass, D. N. Seidman and D. C. Dunand, *Acta Mater.*, 2020, **196**, 396–408.
- 59 Y. Tong, A. Shuitcev and Y. Zheng, *Adv. Eng. Mater.*, 2020, **22**, 1900496.
- 60 G. S. Firstov, J. Van Humbeeck and Y. N. Koval, *Mater. Sci. Eng., A*, 2004, **378**, 2–10.
- 61 G. Fu, X. Liu, X. Yi, S. Zhang, X. Cao, X. Meng, Z. Gao and H. Wang, *Metals*, 2023, **13**, 1279.
- 62 L. Peltier, F. Meraghni, S. Berveiller, P. Lohmuller and P. Laheurte, *Shape Mem. Superelasticity*, 2021, **7**, 438–446.
- 63 S. Li, D. Cong, X. Sun, Y. Zhang, Z. Chen, Z. Nie, R. Li, F. Li, Y. Ren and Y. Wang, *Mater. Res. Lett.*, 2019, **7**, 482–489.
- 64 D. Canadinc, W. Trehern, J. Ma, I. Karaman, F. Sun and Z. Chaudhry, *Scr. Mater.*, 2019, **158**, 83–87.
- 65 A. Rohatgi, D. J. Harach, K. S. Vecchio and K. P. Harvey, *Acta Mater.*, 2003, **51**, 2933–2957.
- 66 N. Thiyaneshwaran, C. P. Selvan, A. Lakshmikanthan, K. Sivaprasad and B. Ravisankar, *J. Mater. Res. Technol.*, 2021, **14**, 1126–1136.
- 67 S. Yang, M. Li, P. Cao, L. Zhang, Q. Zhang, B. Cai and Y. Fang, *Mater. Sci. Eng., A*, 2022, **858**, 144099.
- 68 P. Li, N. T. Aboulkhair, J. Wu, K. L. Leng, D. Yang, A. T. Clare, X. Hou and F. Xu, *J. Mater. Res. Technol.*, 2023, **27**, 4891–4907.
- 69 Y. F. Luo, R. Y. Lu, Y. Wang, B. Liu, H. T. Yang and Y. Liu, *Trans. Nonferrous Met. Soc. China*, 2023, **33**, 2054–2063.
- 70 M. K. Mani, G. Viola, M. J. Reece, J. P. Hall and S. L. Evans, *Mater. Sci. Eng., A*, 2014, **592**, 19–27.
- 71 C. Stangl, E. Kollmannsberger, T. A. Zimogliadova, M. Krüger and H. Saage, *Intermetallics*, 2022, **146**, 107566.

- 72 Y. Mu, L. Liu, J. Shi, T. Sun, K. Hu, Y. Jia, K. Song, Y. Jia, Q. Wang and G. Wang, *Composites, Part B*, 2022, **247**, 110322.
- 73 K. Yao, Y. Zhang, L. Liu, X. Zhang, K. Duan, B. Liu, J. Qi, Z. Zhao and F. Wu, *J. Alloys Compd.*, 2023, **947**, 169616.
- 74 B. Xiao, J. Zhang, S. Liu, Y. Zhou, J. Ju, J. J. Kai, Y. Zhao, X. Yang, L. Xu, S. Zhao and T. Yang, *Acta Mater.*, 2024, **262**, 119459.
- 75 B. Xiao, J. Zhang, S. Liu, Y. Zhao, L. Xu, C. T. Liu and T. Yang, *J. Mater. Sci. Technol.*, 2023, **160**, 28–33.
- 76 I. Baker, B. Huang and E. M. Schulson, *Acta Metall.*, 1988, **36**, 493–499.
- 77 E. Chen, A. Tamm, T. Wang, M. E. Epler, M. Asta and T. Frolov, *npj Comput. Mater.*, 2022, **8**, 80.
- 78 M. Dodaran, A. H. Etefagh, S. M. Guo, M. M. Khonsari, W. J. Meng, N. Shamsaei and S. Shao, *Intermetallics*, 2020, **117**, 106670.
- 79 Y. T. Zhu, K. Ameyama, P. M. Anderson, I. J. Beyerlein, H. J. Gao, H. S. Kim, E. Lavernia, S. Mathaudhu, H. Mughrabi, R. O. Ritchie, N. Tsuji, X. Y. Zhang and X. L. Wu, *Mater. Res. Lett.*, 2020, **9**, 1–31.
- 80 P. Zhang, Y. Yuan, B. Li, S. W. Guo, G. X. Yang and X. L. Song, *Mater. Sci. Eng., A*, 2016, **655**, 152–159.
- 81 T. Takasugi, N. Masahashi and O. Izumi, *Acta Metall.*, 1987, **35**, 381–391.
- 82 C. T. Liu, C. L. White and J. A. Horton, *Acta Metall.*, 1985, **33**, 213–229.
- 83 B. Xiao, L. Xu, C. Cayron, J. Xue, G. Sha and R. Logé, *Acta Mater.*, 2020, **195**, 199–208.
- 84 M. Biesuz, L. Spiridigliozzi, G. Dell'Agli, M. Bortolotti and V. M. Sglavo, *J. Mater. Sci.*, 2018, **53**, 8074–8085.
- 85 H. Xie, M. Qin, M. Hong, J. Rao, M. Guo, J. Luo and L. Hu, *Sci. Adv.*, 2022, **8**, 8241.
- 86 J. Zhang, J. Yan, S. Calder, Q. Zheng, M. A. McGuire, D. L. Abernathy, Y. Ren, S. H. Lapidus, K. Page, H. Zheng, J. W. Freeland, J. D. Budai and R. P. Hermann, *Chem. Mater.*, 2019, **31**, 3705–3711.
- 87 X. Wang, S. Wei, B. Wang, X. Cheng, Y. Wang and Y. Liang, *J. Mater. Sci.: Mater. Electron.*, 2023, **34**, 47–60.
- 88 Z. F. Zhao, H. Chen, H. M. Xiang, F. Z. Dai, X. H. Wang, W. Xu, K. Sun, Z. J. Peng and Y. C. Zhou, *J. Mater. Sci. Technol.*, 2020, **39**, 167–172.
- 89 J. Zhang, S. Liu, Z. Tian, Y. Zhang and Z. Shi, *Materials*, 2023, **16**, 16062214.
- 90 W. Lu, L. Chen, W. Zhang, W. Su, Y. Wang, Y. Fu and Y. Zhou, *J. Eur. Ceram. Soc.*, 2022, **42**, 2021–2027.
- 91 J. Zhang, B. Xu, Y. Xiong, S. Ma, Z. Wang, Z. Wu and S. Zhao, *npj Comput. Mater.*, 2022, **8**, 5.
- 92 Q. Zhou, F. Xu, C. Z. Gao, D. Zhang, X. Q. Shi, M. F. Yuen and D. W. Zuo, *Ceram. Int.*, 2023, **49**, 5760–5769.
- 93 Y. Yan, Z. Pei, M. C. Gao, S. Mixture and K. Wang, *Acta Mater.*, 2023, **253**, 118955.
- 94 D. G. Sangiovanni, K. Kaufmann and K. Vecchio, *Sci. Adv.*, 2023, **9**, 2960.
- 95 S. Y. Liu, S. Zhang, S. Liu, D. J. Li, Y. Li and S. Wang, *J. Eur. Ceram. Soc.*, 2021, **41**, 6267–6274.
- 96 J. Gild, Y. Zhang, T. Harrington, S. Jiang, T. Hu, M. C. Quinn, W. M. Mellor, N. Zhou, K. Vecchio and J. Luo, *Sci. Rep.*, 2016, **6**, 37946.
- 97 J. Schmidt, M. R. G. Marques, S. Botti and M. A. L. Marques, *npj Comput. Mater.*, 2019, **5**, 83.
- 98 L. López-de-la-Torre, B. Winkler, J. Schreuer, K. Knorr and M. Avalos-Borja, *Solid State Commun.*, 2005, **134**, 245–250.
- 99 J. F. Smith, O. N. Carlson and R. R. De Avillez, *J. Nucl. Mater.*, 1987, **148**, 1–16.
- 100 J. Ma, M. Wu, Y. Du, S. Chen, J. Ye and L. Jin, *Mater. Lett.*, 2009, **63**, 905–907.
- 101 K. Balasubramanian, S. V. Khare and D. Gall, *Acta Mater.*, 2018, **152**, 175–185.
- 102 H. Kindlund, D. G. Sangiovanni, I. Petrov, J. E. Greene and L. Hultman, *Thin Solid Films*, 2019, **688**, 137479.
- 103 S. Guo, C. Ng, J. Lu and C. T. Liu, *J. Appl. Phys.*, 2011, **109**, 103505.
- 104 C. T. Liu, *Int. Met. Rev.*, 2013, **29**, 168–194.
- 105 A. Roy, T. Babuska, B. Krick and G. Balasubramanian, *Scr. Mater.*, 2020, **185**, 152–158.
- 106 M. Magnuson, L. Hultman and H. Höglberg, *Vacuum*, 2022, **196**, 110567.
- 107 T. J. Harrington, J. Gild, P. Sarker, C. Toher, C. M. Rost, O. F. Dippo, C. McElfresh, K. Kaufmann, E. Marin, L. Borowski, P. E. Hopkins, J. Luo, S. Curtarolo, D. W. Brenner and K. S. Vecchio, *Acta Mater.*, 2019, **166**, 271–280.
- 108 H. Huang, L. Shao and H. Liu, *Phys. Status Solidi B*, 2021, **258**, 2100140.
- 109 P. Sarker, T. Harrington, C. Toher, C. Oses, M. Samiee, J. P. Maria, D. W. Brenner, K. S. Vecchio and S. Curtarolo, *Nat. Commun.*, 2018, **9**, 4980.
- 110 O. F. Dippo, N. Mesgarzadeh, T. J. Harrington, G. D. Schrader and K. S. Vecchio, *Sci. Rep.*, 2020, **10**, 21288.
- 111 S. Y. Liu, L. Qin, H. Zhang, C. Liu, S. Liu, D. J. Li, T. Yadav, D. Shah and S. Wang, *Ceram. Int.*, 2024, **50**, 17977–17987.
- 112 D. G. Sangiovanni, *Acta Mater.*, 2018, **151**, 11–20.
- 113 W. C. Chen, J. N. Schmidt, D. Yan, Y. K. Vohra and C. C. Chen, *npj Comput. Mater.*, 2021, **7**, 114.
- 114 A. Mansouri Tehrani, A. O. Olynyk, M. Parry, Z. Rizvi, S. Couper, F. Lin, L. Miyagi, T. D. Sparks and J. Brgoch, *J. Am. Chem. Soc.*, 2018, **140**, 9844–9853.
- 115 C. Nam, *Mater. Today Commun.*, 2023, **35**, 32–41.
- 116 J. Gild, A. Wright, K. Quiambao-Tomko, M. Qin, J. A. Tomko, M. Shafkat bin Hoque, J. L. Braun, B. Bloomfield, D. Martinez, T. Harrington, K. Vecchio, P. E. Hopkins and J. Luo, *Ceram. Int.*, 2020, **46**, 6906–6913.
- 117 T. K. Chen and M. S. Wong, *Surf. Coat. Technol.*, 2008, **203**, 495–500.
- 118 D. O. Moskovskikh, S. Vorotilo, A. S. Sedegov, K. V. Kuskov, K. V. Bardasova, P. V. Kiryukhantsev-korneev, M. Zhukovskiy and A. S. Mukasyan, *Ceram. Int.*, 2020, **46**, 19008–19014.
- 119 V. Braic, A. C. Parau, I. Pana, M. Braic and M. Balaceanu, *Surf. Coat. Technol.*, 2014, **258**, 996–1005.
- 120 M. Braic, M. Balaceanu, A. Vladescu, C. N. Zoita and V. Braic, *Appl. Surf. Sci.*, 2013, **284**, 671–678.

- 121 W. J. Shen, M. H. Tsai and J. W. Yeh, *Coatings*, 2015, **5**, 312–325.
- 122 P. Cui, W. Li, P. Liu, K. Zhang, F. Ma, X. Chen, R. Feng and P. K. Liaw, *J. Alloys Compd.*, 2020, **834**, 223–230.
- 123 P. K. Huang and J. W. Yeh, *Thin Solid Films*, 2009, **518**, 180–184.
- 124 M. H. Hsieh, M. H. Tsai, W. J. Shen and J. W. Yeh, *Surf. Coat. Technol.*, 2013, **221**, 118–123.
- 125 A. J. Wright, Q. Wang, S.-T. Ko, K. M. Chung, R. Chen and J. Luo, *Scr. Mater.*, 2020, **181**, 76–81.
- 126 M. Li, C. Huang, B. Zhao, H. Liu, J. Wang and Z. Liu, *Ceram. Int.*, 2017, **43**, 14192–14199.
- 127 X. Hou, S. Zhou, T. Jia, H. Lin and H. Teng, *J. Eur. Ceram. Soc.*, 2011, **31**, 733–738.
- 128 D. Feng, Q. Ren, H. Ru, W. Wang, S. Ren and C. Zhang, *Mater. Sci. Eng., A*, 2021, **802**, 140443.
- 129 V. V. Rodaev, A. O. Zhigachev, V. V. Korenkov and Y. I. Golovin, *Mater. Sci. Eng., A*, 2018, **730**, 363–366.
- 130 G. Zhao, C. Huang, H. Liu, B. Zou, H. Zhu and J. Wang, *Mater. Sci. Eng., A*, 2014, **606**, 108–116.
- 131 L. Zhang, X. Li, D. Hu, P. Chen, X. Li, T. Xie, Q. Yuan, L. Wu, Q. Liu and J. Li, *J. Am. Ceram. Soc.*, 2023, **106**, 5311–5321.
- 132 W. Li, F. Li, Z. Yu, Q. Wen, B. Fan, Y. Feng, C. Zhao, E. Ricohermoso, III, M. Widenmeyer, A. Weidenkaff and R. Riedel, *J. Eur. Ceram. Soc.*, 2022, **42**, 4493–4502.
- 133 D. Ye, D. C. Jia, Z. H. Yang, Z. L. Sun and P. F. Zhang, *J. Zhejiang Univ., Sci., A*, 2010, **11**, 761–765.
- 134 J. Song, G. Chen, H. Xiang, F. Dai, S. Dong, W. Han, X. Zhang and Y. Zhou, *J. Mater. Sci. Technol.*, 2022, **121**, 181–189.
- 135 F. Cai, D. Ni, W. Bao, B. Chen, J. Lu, X. Zou, Y. Qin and S. Dong, *Composites, Part B*, 2022, **243**, 110177.
- 136 D. Demirskiy, H. Borodianska, T. S. Suzuki, Y. Sakka, K. Yoshimi and O. Vasylykiv, *Scr. Mater.*, 2019, **164**, 12–16.
- 137 Y. F. Ye, C. T. Liu and Y. Yang, *Acta Mater.*, 2015, **94**, 152–161.
- 138 X. Yan, L. Constantin, Y. Lu, J. F. Silvain, M. Nastasi and B. Cui, *J. Am. Ceram. Soc.*, 2018, **101**, 4486–4491.
- 139 A. C. Feltrin and F. Akhtar, *J. Eur. Ceram. Soc.*, 2023, **43**, 7363–7372.
- 140 F. Wang, X. Zhang, X. L. Yan, Y. F. Lu, M. Nastasi, Y. Chen and B. Cui, *J. Am. Ceram. Soc.*, 2020, **103**, 4463–4472.
- 141 H. Chen, H. Xiang, F. Z. Dai, J. Liu, Y. Lei, J. Zhang and Y. Zhou, *J. Mater. Sci. Technol.*, 2019, **35**, 1700–1705.
- 142 B. Ye, T. Wen, M. C. Nguyen, L. Hao, C. Z. Wang and Y. Chu, *Acta Mater.*, 2019, **170**, 15–23.
- 143 A. Kirnbauer, C. Spadt, C. M. Koller, S. Kolozsvári and P. H. Mayrhofer, *Vacuum*, 2019, **168**, 108850.
- 144 M. I. Lin, M. H. Tsai, W. J. Shen and J. W. Yeh, *Thin Solid Films*, 2010, **518**, 2732–2737.
- 145 Z. M. Yang, K. Zhang, N. Qiu, H. B. Zhang, Y. Wang and J. Chen, *Chin. Phys. B*, 2019, **28**, 046201.
- 146 J. Sun, R. Ren, H. Yue, W. Cui, G. Wang, C. Xu, J. Qiao, W. Sun, K. Sun and Z. Wang, *Chin. Chem. Lett.*, 2023, **34**, 107776.
- 147 Y. An, K. Wan, M. Song and L. Zhao, *Ceram. Int.*, 2024, **50**, 4699–4707.
- 148 J. Zhu, X. Meng, P. Zhang, Z. Li, J. Xu, M. J. Reece and F. Gao, *J. Eur. Ceram. Soc.*, 2021, **41**, 2861–2869.
- 149 R. Yan, W. Liang, Q. Miao, H. Zhao, R. Liu, J. Li, K. Zang, M. Dong, X. He, X. Gao and Y. Song, *Ceram. Int.*, 2023, **49**, 20729–20741.
- 150 H. R. Mao, R. F. Guo, Y. Cao, S. B. Jin, X. M. Qiu and P. Shen, *J. Eur. Ceram. Soc.*, 2021, **41**, 2855–2860.
- 151 Z. Teng, P. Wang, S. Zeng, W. Feng, C. Chen, P. Jia, Y. Tan and S. Peng, *Ceram. Int.*, 2023, **50**, 6892–6897.
- 152 S. Fu, Z. Jia, D. Wan and Y. Bao, *Ceram. Int.*, 2024, **50**, 5510–5515.
- 153 R. Yang, J. Xu, M. Wei, J. Zhu, X. Meng, P. Zhang, J. Yang and F. Gao, *Ceram. Int.*, 2022, **48**, 28586–28594.
- 154 J. Zhu, M. Wei, J. Xu, R. Yang, X. Meng, P. Zhang, J. Yang, G. Li and F. Gao, *J. Adv. Ceram.*, 2022, **11**, 1222–1234.
- 155 D. Guo, F. Zhou, B. Xu, Y. Wang and Y. Wang, *Chin. J. Aeronaut.*, 2022, **36**, 556–564.
- 156 Z. Liu, C. Wei, Y. De, S. Zhang, C. Zhang and X. Li, *J. Eur. Ceram. Soc.*, 2023, **43**, 7613–7622.
- 157 X. Luo, H. Li, S. Huang, K. Li, J. Li, X. Yang, C. Xu, S. Hou and H. Jin, *J. Eur. Ceram. Soc.*, 2023, **43**, 5339–5346.
- 158 Z. Deng, Y. Peng, W. W. Qin, B. Liu, G. Zhang, X. Wang, Y. Xie, L. Zhu and D. Xu, *Chem. Eng. J.*, 2023, **475**, 146260.
- 159 K. Chen, X. Pei, L. Tang, H. Cheng, Z. Li, C. Li, X. Zhang and L. An, *J. Eur. Ceram. Soc.*, 2018, **38**, 4161–4164.
- 160 J. T. Zhu, X. Y. Meng, J. Xu, P. Zhang, Z. H. Lou, M. J. Reece and F. Gao, *J. Eur. Ceram. Soc.*, 2021, **41**, 1052–1057.
- 161 J. Gild, M. Samiee, J. L. Braun, T. Harrington, H. Vega, P. E. Hopkins, K. Vecchio and J. Luo, *J. Eur. Ceram. Soc.*, 2018, **38**, 3578–3584.
- 162 F. Ye, T. Luo, F. Meng and L. Guo, *Ceram. Int.*, 2024, **50**, 181–187.
- 163 H. Li, X. Luo, S. Huang, K. Li, S. Zhang and H. Jin, *Ceram. Int.*, 2023, **49**, 39627–39631.
- 164 R. Liu, W. Liang, Q. Miao, H. Zhao, S. Ramakrishna, B. Ramasubramanian, X. Zhang, Y. Song, X. Gao, J. Du and X. Tao, *J. Mater. Res. Technol.*, 2023, **27**, 1365–1380.
- 165 F. Li, L. Zhou, J. X. Liu, Y. Liang and G. J. Zhang, *J. Adv. Ceram.*, 2019, **8**, 576–582.
- 166 Z. F. Zhao, H. M. Xiang, F. Z. Dai, Z. J. Peng and Y. C. Zhou, *J. Mater. Sci. Technol.*, 2019, **35**, 2647–2651.
- 167 K. Ren, Q. Wang, G. Shao, X. Zhao and Y. Wang, *Scr. Mater.*, 2020, **178**, 382–386.
- 168 W. Hong, F. Chen, Q. Shen, Y. H. Han, W. G. Fahrenholtz and L. Zhang, *J. Am. Ceram. Soc.*, 2018, **102**, 2228–2237.
- 169 G. N. Kotsonis, C. M. Rost, D. T. Harris and J. P. Maria, *MRS Commun.*, 2018, **8**, 1371–1377.
- 170 J. L. Braun, C. M. Rost, M. Lim, A. Giri, D. H. Olson, G. N. Kotsonis, G. Stan, D. W. Brenner, J. P. Maria and P. E. Hopkins, *Adv. Mater.*, 2018, **30**, 1805004–1805012.
- 171 Y. Zhang, X. H. Yan, W. B. Liao and K. Zhao, *Entropy*, 2018, **20**, 624.
- 172 M. H. Tsai, C. H. Lai, J. W. Yeh and J. Y. Gan, *J. Phys. D: Appl. Phys.*, 2008, **41**, 235402.
- 173 J. Li, Y. Zhao, X. Shi, J. Zheng, Y. Dong, J. Chen, Y. Chen, D. Sun, S. Zhang and S. Wang, *Ceram. Int.*, 2023, **49**, 40382–40391.

- 174 C. H. Chang, P. W. Li, Q. Q. Wu, M. H. Wang, C. C. Sung and C. Y. Hsu, *Mater. Technol.*, 2018, **34**, 343–349.
- 175 P. K. Huang and J. W. Yeh, *Scr. Mater.*, 2010, **62**, 105–108.
- 176 J. J. Wang, S. Y. Chang and F. Y. Ouyang, *Surf. Coat. Technol.*, 2020, **393**, 125796.
- 177 H. T. Hsueh, W. J. Shen, M. H. Tsai and J. W. Yeh, *Surf. Coat. Technol.*, 2012, **206**, 4106–4112.
- 178 P. Cui, W. Li, P. Liu, K. Zhang, F. Ma, X. Chen, R. Feng and P. K. Liaw, *J. Alloys Compd.*, 2020, **834**, 155063.
- 179 K. von Fieandt, L. Riekehr, B. Osinger, S. Fritze and E. Lewin, *Surf. Coat. Technol.*, 2020, **389**, 125614.
- 180 K. von Fieandt, E.-M. Paschalidou, A. Srinath, P. Soucek, L. Riekehr, L. Nyholm and E. Lewin, *Thin Solid Films*, 2020, **693**, 137685.
- 181 N. A. Khan, B. Akhavan, C. Zhou, H. Zhou, L. Chang, Y. Wang, Y. Liu, M. M. Bilek and Z. Liu, *Surf. Coat. Technol.*, 2020, **402**, 126327.
- 182 O. V. Sobol, A. A. Andreev, V. F. Gorban, H. O. Postelnyk, V. A. Stolbovoy, A. V. Zvyagolsky, A. V. Dolomanov, Z. V. Kraievska and P. At, *Sci. Technol.*, 2019, **9**, 127–135.
- 183 A. Kirnbauer, A. Kretschmer, C. M. Koller, T. Wojcik, V. Paneta, M. Hans, J. M. Schneider, P. Polcik and P. H. Mayrhofer, *Surf. Coat. Technol.*, 2020, **389**, 125674.
- 184 K. Johansson, L. Riekehr, S. Fritze and E. Lewin, *Surf. Coat. Technol.*, 2018, **349**, 529–539.
- 185 J. Li, Y. Chen, Y. Zhao, X. Shi, S. wang and S. Zhang, *J. Alloys Compd.*, 2022, **926**, 166807.
- 186 A. A. Bagdasaryan, A. V. Pshyk, L. E. Coy, M. Kempinski, A. D. Pogrebnyak, V. M. Beresnev and S. Jurga, *Mater. Lett.*, 2018, **229**, 364–367.
- 187 Z. C. Chang, *Mater. Chem. Phys.*, 2018, **220**, 98–110.
- 188 R. Chen, Z. Cai, J. Pu, Z. Lu, S. Chen, S. Zheng and C. Zeng, *J. Alloys Compd.*, 2020, **827**, 153836.
- 189 A. D. Pogrebnyak, A. A. Bagdasaryan, V. M. Beresnev, A. I. Kupchishin, S. V. Plotnikov and Y. O. Kravchenko, *High Temp. Mater. Process.*, 2017, **21**, 261–275.
- 190 D. Yu, J. Yin, B. Zhang, X. Liu, M. J. Reece, W. Liu and Z. Huang, *J. Eur. Ceram. Soc.*, 2021, **41**, 3823–3831.
- 191 W. Zhang, L. Chen, C. Xu, W. Lu, Y. Wang, J. Ouyang and Y. Zhou, *J. Mater. Sci. Technol.*, 2021, **72**, 23–28.
- 192 L. Feng, W. G. Fahrenholtz and G. E. Hilmas, *J. Am. Ceram. Soc.*, 2019, **102**, 7217–7224.
- 193 K. Sun, Z. Yang, R. Mu, S. Niu, Y. Wang and D. Wang, *J. Eur. Ceram. Soc.*, 2021, **41**, 3196–3206.
- 194 E. Castle, T. Csanádi, S. Grasso, J. Dusza and M. Reece, *Sci. Rep.*, 2018, **8**, 8609.
- 195 L. He, L. Liu, F. Peng, W. Zhang, N. Lin, S. Zhao, Y. Ma and Z. Wu, *J. Eur. Ceram. Soc.*, 2023, **43**, 5792–5801.
- 196 S. Li, Q. Wu, J. Zhan, R. Chen, A. Mao, C. Zheng and H. Wen, *J. Eur. Ceram. Soc.*, 2024, **44**, 1890–1897.
- 197 O. Popov and V. Vishnyakov, *Materialia*, 2023, **32**, 101890.
- 198 L. Chen, W. Zhang, Y. Tan, P. Jia, C. Xu, Y. Wang, X. Zhang, J. Han and Y. Zhou, *J. Eur. Ceram. Soc.*, 2021, **41**, 60–67.
- 199 M. Braic, V. Braic, M. Balaceanu, C. N. Zoita, A. Vladescu and E. Grigore, *Surf. Coat. Technol.*, 2010, **204**, 2010–2014.
- 200 H. Chen, Z. Wu, M. Liu, W. Hai and W. Sun, *J. Eur. Ceram. Soc.*, 2021, **41**, 7498–7506.
- 201 D. Liu, A. Zhang, J. Jia, J. Meng and B. Su, *J. Eur. Ceram. Soc.*, 2020, **40**, 2746–2751.
- 202 G. Tallarita, R. Licheri, S. Garroni, R. Orrù and G. Cao, *Scr. Mater.*, 2019, **158**, 100–104.
- 203 Y. Zhang, W. M. Guo, Z. B. Jiang, Q. Q. Zhu, S. K. Sun, Y. You, K. Plucknett and H. T. Lin, *Scr. Mater.*, 2019, **164**, 135–139.
- 204 Y. Zhang, S. K. Sun, W. M. Guo, W. Zhang, L. Xu, J. H. Yuan, D. K. Guan, D. W. Wang, Y. You and H. T. Lin, *J. Eur. Ceram. Soc.*, 2021, **41**, 1015–1019.
- 205 S. Failla, P. Galizia, S. Fu, S. Grasso and D. Sciti, *J. Eur. Ceram. Soc.*, 2020, **40**, 588–593.
- 206 M. Qin, J. Gild, H. Wang, T. Harrington, K. S. Vecchio and J. Luo, *J. Eur. Ceram. Soc.*, 2020, **40**, 4348–4353.
- 207 M. Qin, Q. Yan, H. Wang, K. S. Vecchio and J. Luo, *J. Eur. Ceram. Soc.*, 2021, **41**, 2968–2973.
- 208 P. H. Mayrhofer, A. Kirnbauer, P. Ertelthaler and C. M. Koller, *Scr. Mater.*, 2018, **149**, 93–97.
- 209 J. Pelleg, *The Strength and Strengthening of Ceramics*, Springer International Publishing, Cham, 2014, pp. 351–415.
- 210 S. C. Luo, W. M. Guo, Z. L. Fang, K. Plucknett and H. T. Lin, *J. Eur. Ceram. Soc.*, 2022, **42**, 336–343.
- 211 Q. Sun, W. Chen, S. Zhu, J. Cheng, H. Tan, J. Chen, J. Guo and J. Yang, *Tribol. Int.*, 2023, **184**, 108471.
- 212 V. Kombamuthu, H. Ünsal, Z. Chlup, M. Tatarková, A. Kovalčíková, I. Zhukova, N. Hosseini, M. Hičák, I. Dlouhý and P. Tatarko, *J. Eur. Ceram. Soc.*, 2023, **22**, 93–97.
- 213 M. Ma, B. Ye, Y. Han, L. Sun, J. He and Y. Chu, *J. Am. Ceram. Soc.*, 2020, **103**, 587–592.
- 214 C. Chen, H. Zhang, D. Qiao, P. Xia, X. Tao, W. Dang, S. Gu and Y. Yang, *Ceram. Int.*, 2024, **50**, 5570–5578.
- 215 Y. Z. Zhou, K. H. Huang, G. X. Bo, S. C. Luo, W. M. Guo, S. K. Sun and H. T. Lin, *Ceram. Int.*, 2023, **49**, 33652–33658.
- 216 F. Peng, Z. Wei, Q. Song, L. He, F. Dai, W. Zhang and Z. Wu, *J. Am. Ceram. Soc.*, 2023, **106**, 4443–4454.
- 217 Y. J. Zhong, W. S. Xiang, L. T. He, J. Z. Li, J. Hao, Z. I. Tian and X. Wang, *J. Eur. Ceram. Soc.*, 2021, **41**, 7119–7129.
- 218 A. G. Evans, *J. Am. Ceram. Soc.*, 1990, **73**, 187–206.
- 219 Z. Cao, J. Sun, L. Meng, K. Zhang, J. Zhao, Z. Huang and X. Yun, *J. Mater. Sci. Technol.*, 2023, **161**, 10–43.
- 220 R. Li, R. Y. Luo, N. Lin, A. Q. Li, X. C. Zhang, Y. Tang, Z. G. Wu, Z. Y. Wang and C. Ma, *Ceram. Int.*, 2022, **48**, 32540–32545.
- 221 D. Baril, S. P. Tremblay and M. Fiset, *J. Mater. Sci.*, 2004, **28**, 5486–5494.
- 222 D. Liu, A. Zhang, J. Jia, J. Han, J. Zhang and J. Meng, *Composites, Part B*, 2021, **212**, 108681.
- 223 Y. T. Li, X. M. Chen, X. K. Zeng, M. Liu, X. Jiang and Y. X. Leng, *J. Mater. Sci. Technol.*, 2024, **173**, 20–30.
- 224 Y. T. Li, X. Jiang, X. T. Wang and Y. X. Leng, *Scr. Mater.*, 2024, **238**, 115763.
- 225 J. Sun, J. Zhao, Y. Chen, L. Wang, X. Yun and Z. Huang, *Composites, Part B*, 2022, **231**, 109586.
- 226 Z. Wang, X. Li, X. Wang, S. Cai, P. Ke and A. Wang, *Surf. Coat. Technol.*, 2016, **304**, 553–559.

- 227 Y. X. Wang, S. Zhang, J. W. Lee, W. S. Lew, D. Sun and B. Li, *Surf. Coat. Technol.*, 2013, **231**, 346–352.
- 228 T. Yang, Y. L. Zhao, Y. Tong, Z. B. Jiao, J. Wei, J. X. Cai, X. D. Han, D. Chen, A. Hu, J. J. Kai, K. Lu, Y. Liu and C. T. Liu, *Science*, 2018, **362**, 933–937.
- 229 P. Zhang, X. Liu, A. Cai, Q. Du, X. Yuan, H. Wang, Y. Wu, S. Jiang and Z. Lu, *Sci. China Mater.*, 2021, **64**, 2037–2044.
- 230 T. Wen, B. Ye, M. C. Nguyen, M. Ma and Y. Chu, *J. Am. Ceram. Soc.*, 2020, **103**, 6475–6489.
- 231 A. V. Pshyk, A. Vasylenko, B. Bakhit, L. Hultman, P. Schweizer, T. E. J. Edwards, J. Michler and G. Greczynski, *Mater. Des.*, 2022, **219**, 110798.
- 232 C. Zhang, A. Gupta, S. Seal, B. Boesl and A. Agarwal, *J. Am. Ceram. Soc.*, 2017, **100**, 1853–1862.
- 233 N. Alexandre, M. Desmaison-Brut, F. Valin and M. Boncoeur, *J. Mater. Sci.*, 1993, **28**, 2385–2390.
- 234 Y. Hu, J. H. Huang and J. M. Zuo, *J. Mater. Res.*, 2016, **31**, 370–379.
- 235 A. Naughton-Duszová, D. Medveď, L. Ďáková, A. Kovalčíková, P. Švec, P. Tatarko, H. Ünsal, P. Hvizdoš, P. Šajgalík and J. Dusz, *J. Eur. Ceram. Soc.*, 2023, **13**, 2217–2235.
- 236 S. Huo, L. Chen, X. Liu, Q. Kong, Y. Wang, H. Gu and Y. Zhou, *J. Mater. Sci. Technol.*, 2022, **129**, 223–227.
- 237 R. F. Guo, H. R. Mao and P. Shen, *J. Eur. Ceram. Soc.*, 2023, **43**, 5763–5773.
- 238 S. C. Luo, W. M. Guo, K. Plucknett and H. T. Lin, *J. Eur. Ceram. Soc.*, 2021, **41**, 3189–3195.
- 239 Z. N. Cao, J. L. Sun, K. G. Zhang, W. L. Zhao and Z. Yu, *Eur. J. Mech. Solid.*, 2024, **103**, 105165.
- 240 C. L. Huang, K. Sasaki, D. Senthil Raja, C. T. Hsieh, Y. J. Wu, J. T. Su, C. C. Cheng, P. Y. Cheng, S. H. Lin and Y. Choi, *Adv. Energy Mater.*, 2021, **11**, 2101827.
- 241 G. Raj, R. Nandan, K. Kumar, D. B. Gorle, A. B. Mallya, S. M. Osman, J. Na, Y. Yamauchi and K. K. Nanda, *Mater. Horiz.*, 2023, **10**, 5032–5044.
- 242 R. Feng, C. Zhang, M. C. Gao, Z. Pei, F. Zhang, Y. Chen, D. Ma, K. An, J. D. Poplawsky, L. Ouyang, Y. Ren, J. A. Hawk, M. Widom and P. K. Liaw, *Nat. Commun.*, 2021, **12**, 4329.
- 243 J. Li, B. Xie, Q. Fang, B. Liu, Y. Liu and P. K. Liaw, *J. Mater. Sci. Technol.*, 2021, **68**, 70–75.
- 244 Z. Lu, Z. W. Chen and C. V. Singh, *Matter*, 2020, **3**, 1318–1333.
- 245 T. K. Tsao, A. C. Yeh, C. M. Kuo and H. Murakami, *Adv. Eng. Mater.*, 2017, **19**, 1600475.
- 246 O. N. Senkov, G. B. Wilks, D. B. Miracle, C. P. Chuang and P. K. Liaw, *Intermetallics*, 2010, **18**, 1758–1765.
- 247 O. N. Senkov, G. B. Wilks, J. M. Scott and D. B. Miracle, *Intermetallics*, 2011, **19**, 698–706.
- 248 J. Lu, Y. Chen, H. Zhang, L. Li, L. Fu, X. Zhao, F. Guo and P. Xiao, *Corros. Sci.*, 2020, **170**, 108691.
- 249 T. Yang, B. X. Cao, T. L. Zhang, Y. L. Zhao, W. H. Liu, H. J. Kong, J. H. Luan, J. J. Kai, W. Kuo and C. T. Liu, *Mater. Today*, 2022, **52**, 161–174.
- 250 Y. Xue, H. Zhang, X. Zhao, Y. An, G. Liu, Y. Ma, H. Li, H. Zhou and J. Chen, *Ceram. Int.*, 2024, **50**, 18024–18034.